SECONDARY FLOW IN A TWO-DIMENSIONAL CASCADE OF HIGH TURNING ANGLE TURBINE BLADES

BY

GARY JOSEPH PARON, B. ENG.

A Thesis

Submitted to the School of Graduate Studies

in Partial Fulfilment of the Requirements

for the Degree

Master of Engineering

McMaster University

April 1981

MASTER OF ENGINEERING (1981) McMASTER UNIVERSITY
(Mechanical Engineering) Hamilton, Ontario

TITLE: Secondary Flow in a Two-Dimensional Cascade of High Turning Angle Turbine Blades

AUTHOR: G.J. Paron, B. Eng. (McMaster University)

SUPERVISOR: Dr. J. H. T. Wade

NUMBER OF PAGES: xv, 160

ABSTRACT

Modern trends in gas turbine design have been geared to producing a compact high work output engine as a power unit. To achieve this, the turbine rotor must be comprised of high turning angle blades. Secondary flow has always accounted for a major portion of the losses within a blade row and high turning angle blades tend to reinforce these losses. A review of the current literature on secondary flows shows that there is a void of data for two-dimensional high turning angle turbine blade cascades.

The object of this study was to construct and experiment upon a large scale two-dimensional high turning angle turbine blade cascade. Each of the four blades within the cascade had a chord and span of 214 mm and 188.5 mm respectively. The overall test rig was an open circuit wind tunnel which was operated at a Reynolds number of 3.68×10^5 (based on the blade chord) which corresponded to a mean blade inlet velocity VI of 26.5 m/s(87 ft/s). The rig was designed with the facility to adjust the inlet flow in the pitchwise direction to ensure periodicity. Suction chambers were installed on the inlet channel endwalls to control the boundary layers and hence observe their effect on the measured secondary losses. The flow parameters were measured and recorded at the inlet bellmouth throat, at the inlet and the

exit from the cascade and at a distance of 1.5C in the streamwise direction from the cascade exit.

A blade passage surface static pressure distribution is presented and the exit flow parameters are given in the form of contour plots of total pressure loss coefficients and static pressure coefficients. The spanwise distribution of pitchwise averaged flow parameters is given and the measured losses are reported and compared with existing correlations. The measured losses were found to be significantly lower than those predicted by these correlations.

ACKNOWLEDGEMENTS

The author wishes to express his sincere thanks to his supervisor, Dr. J. H. T. Wade for providing constant guidance, encouragement and expertise throughout the course of this work.

The assistance in the fabrication and instrumentation of the test rig provided by G. Innocente, Y. Kitamura, W. Schrader and L. Hensher of the Senior Science Instrument Machine Shop is gratefully acknowledged.

Thanks are also due to D. Schick, F. Drieman and J. Verhaeghe of the Mechanical Engineering Workshop.

The competent assistance of D. Lord and R. Lawton is gratefully acknowledged.

The financial support provided through operating grant A1585 from the National Sciences and Engineering Research Council is also appreciated.

The author would also like to thank Miss L. Hammond for her accurate typing of the thesis.

TABLE OF CONTENTS

			Page
ABSTRACT			iii
ACKNOWLEDGEMENTS			v
TABLE OF CONTENTS			vi
LIST OF FIGURES			ix
NOMENCLATURE			xiv
CHAPTER 1	INTRODUCTION		1
CHAPTER 2	LITERATURE SURVEY		4
CHAPTER 3	THE TWO-DIMENSIONAL TEST RIG		17
	3.1	Overview	17
	3.2	The Inlet Section	19
	3.3	The Two-Dimensional Cascade Section	22
	3.4	The Exit Section	23
	3.5	The Test Rig Air Supply and Associated Components	33
CHAPTER 4	INSTRUMENTATION		38
	4.1	Main Flow Instrumentation	38
	4.1.1	The Traverse Mechanism	39
	4.1.2	Mainstream Measurements	41
	4.2	Inlet Channel Boundary Layer Instrumentation	47
	4.3	Blade Test Passage Instrumentation	52

			Page
	4.3.1	The Endwall and Blade Surface Static Pressure Taps	52
CHAPTER 5		OBJECTIVES AND EXPERIMENTAL PROCEDURES	60
	5.1	Preliminary Tests	60
	5.2	Test Passage Measurements	61
	5.3	Tests at the Exit Measuring Stations	61
CHAPTER 6		EXAMINATION OF THE INLET CHANNEL FLOW PARAMETERS	63
	6.1	Flow Characteristics at the Bellmouth Throat	63
	6.2	Pitchwise Distribution of Velocity and Incidence at the Inlet Measuring Station	63
	6.3	Spanwise Distribution of Velocity and Incidence at the Inlet Measuring Station	70
	6.4	The Endwall Boundary Layer	75
	6.5	Endwall Boundary Layer Control	81
	6.6	Turbulence Intensity at the Inlet Measuring Station	88
CHAPTER 7		THE CASCADE TEST PASSAGE PRESSURE DISTRIBUTION	94
	7.1	Pressure Distribution on the Blade Surfaces	95
	7.2	Pressure Distribution on the Test Passage Endwalls	103
CHAPTER 8		EXAMINATION OF THE EXIT FLOW PARAMETERS	108
	8.1	Chosen Inlet Conditions for the Exit Flow Studies	110

			Page
	8.2	Contour Plots of the Local Total Pressure Loss Coefficient	111
	8.3	Contour Plots of the Local Static Pressure Coefficient	122
	8.4	Spanwise Variation of the Pitchwise Averaged Flow Parameters	128
	8.5	Cascade Losses and Comparison with Correlations	135
CHAPTER 9		CONCLUSIONS AND RECOMMENDATIONS FOR FURTHER STUDIES	142
REFERENCES			147
APPENDIX 1		ERROR ANALYSIS	150
APPENDIX 2		SUPPLEMENT FOR INSTRUMENTATION	154
APPENDIX 3		SPECIFICATIONS FOR THE BELLMOUTH INLET DUCT	158

LIST OF FIGURES

Figure	Title	Page
2.1	Secondary Flow and Vortices Occurring in a Turbine Blade Passage	7
2.2	Example of Flow Losses Through a Row of Turbine Blades	8
3.1	Plan View of the Two-Dimensional Cascade Test Rig	18
3.2	The Bellmouth Entrance Duct	20
3.3	Hole Pattern Used in the Inner and Outer Endwall Boundary Layer Suction Chambers	24
3.4	Test Section Plan View	26
3.5 a)	Overview for Figure 3.5 b)	27
3.5 b)	Alternate View of Test Section	29
3.6	Boundary Layer Suction Apparatus	30
3.7	Overall View of Test Facility	32
3.8	The Turbine Blade Profile	35
3.9	Schematic Representation of the Overall Test Facility	36
4.1	Cascade Inlet and Exit Measuring Stations	40
4.2	Probes Used for Mainstream Measurements	44
4.3	The Pressure Transducer	45
4.4	Transducer Calibration Curve	46
4.5	Transducer Calibration Apparatus	49
4.6	Inner Endwall Boundary Layer Probe	50
4.7	Outer Endwall Boundary Layer Probe	51

Figure	Title	Page
4.8	Axial Locations of the Static Pressure Taps in the Cascade Test Passage	53
4.9	Location of the Static Pressure Taps in the Cascade Endwalls	54
4.10	Location of the Static Pressure Taps on the Blade Pressure Surface	55
4.11	Location of the Static Pressure Taps on the Blade Suction Surface	56
4.12	Test Passage Instrumentation	58
6.1	Velocity Distribution at the Bellmouth Throat at Various Throat Width Locations	64
6.2	Pitchwise Distribution of Velocity and Incidence at the Inlet Measuring Station at 20% Blade Span	67
6.3	Pitchwise Distribution of Velocity and Incidence at the Inlet Measuring Station at 50% Blade Span	68
6.4	Pitchwise Distribution of Velocity and Incidence at the Inlet Measuring Station at 80% Blade Span	69
6.5	Cascade Equipotentials and Streamlines from the Electrical Analogue Potential Flow Solution	71
6.6	Electrical Analogue Apparatus	73
6.7	Pitchwise Distribution of Incidence from the Electrical Analogue Potential Flow Solution	74
6.8	Spanwise Distribution of Velocity and Incidence at the Geometric Projection of the Centre of Passage I	76
6.9	Spanwise Distribution of Velocity and Incidence at the Geometric Projection of the Leading Edge of Blade 2	77

Figure	Title	Page
6.10	Spanwise Distribution of Velocity and Incidence at the Geometric Projection of the Centre of the Test Passage	78
6.11	Spanwise Distribution of Velocity and Incidence at the Geometric Projection of the Leading Edge of Blade 3	79
6.12	Spanwise Distribution of Velocity and Incidence at the Geometric Projection of the Centre of Passage III	80
6.13	Boundary Layer Profiles at the Inner and Outer Endwalls	82
6.14	The Effect of Suction on the Boundary Layer Profiles at the Inner Endwall at the Geometric Centre of the Test Passage	86
6.15	The Effect of Suction on the Boundary Layer Profiles at the Outer Endwall at the Geometric Centre of the Test Passage	87
6.16	Hot Wire Probe Calibration Apparatus	90
6.17	Calibration Curve for the Hot Wire Probe	91
6.18	Turbulence Intensity at Various Percentages of the Blade Span	93
7.1	Cp_s Contours on the Blade Pressure Surface	96
7.2	Cp_s Contours on the Blade Suction Surface	97
7.3	Blade Surface Pressure Distribution	98
7.4	Comparison of the Blade Surface Pressure Distribution at 50% Blade Span with the Two-Dimensional Potential Flow Solution Reported in Ref. {17}	102

Figure	Title	Page
7.5	Cp_s Contours on the Inner Endwall	104
7.6	Cp_s Contours on the Outer Endwall	105
7.7	Endwall Static Pressure Distribution at the Cascade Exit	106
8.1	Distribution of the Local Total Pressure Loss Coefficient for Inlet Condition a) (No Suction)	112
8.2	Distribution of the Local Total Pressure Loss Coefficient for Inlet Condition b) (Suction at the Inner Endwall Corresponding to -11.68 mm (-4.6 inches) of water)	113
8.3	Distribution of the Local Total Pressure Loss Coefficient for Inlet Condition c) (Suction at the Outer Endwall Corresponding to -11.68 mm (-4.6 inches) of water)	114
8.4	Distribution of the Local Total Pressure Loss Coefficient for Inlet Condition d) (Suction at Both Endwalls Corresponding to -11.68 mm (-4.6 inches) of water)	115
8.5	Distribution of the Local Total Pressure Loss Coefficient for Inlet Condition e) (Maximum Suction at Both Endwalls Corresponding to -26.65 mm (-10.1 inches) of water)	116
8.6	Formation of the 'Passage Vortex'	118
8.7	Distribution of the Local Static Pressure Coefficient for Inlet Condition a) (No Suction)	123
8.8	Distribution of the Local Static Pressure Coefficient for Inlet Condition b) (Suction at the Inner Endwall Corresponding to -11.68 mm (-4.6 inches) of water)	124

Figure	Title	Page
8.9	Distribution of the Local Static Pressure Coefficient for Inlet Condition c) (Suction at the Outer Endwall Corresponding to -11.68 mm (-4.6 inches) of water)	125
8.10	Distribution of the Local Static Pressure Coefficient for Inlet Condition d) (Suction at Both Endwalls Corresponding to -11.68 mm (-4.6 inches) of water)	126
8.11	Distribution of the Local Static Pressure Coefficient for Inlet Condition e) (Maximum Suction at Both Endwalls Corresponding to -26.65 mm (-10.1 inches) of water)	127
8.12	Spanwise Distribution of Pitchwise Averaged Flow Parameters for Inlet Condition a) (No Suction)	130
8.13	Spanwise Distribution of Pitchwise Averaged Flow Parameters for Inlet Condition b) (Suction at the Inner Endwall Corresponding to -11.68 mm (-4.6 inches) of water)	131
8.14	Spanwise Distribution of Pitchwise Averaged Flow Parameters for Inlet Condition c) (Suction at the Outer Endwall Corresponding to -11.68 mm (-4.6 inches) of water)	132
8.15	Spanwise Distribution of Pitchwise Averaged Flow Parameters for Inlet Condition d) (Suction at Both Endwalls Corresponding to -11.68 mm (-4.6 inches) of water)	133
8.16	Spanwise Distribution of Pitchwise Averaged Flow Parameters for Inlet Condition e) (Maximum Suction at Both Endwalls Corresponding to -26.65 mm (-10.1 inches) of water)	134
8.17	Variation of Gross Secondary Loss with the Inlet Displacement Thickness	139
A2.1	Manufacturer's Calibration Data for the Three-Dimensional Probe	155

NOMENCLATURE

Symbols	Description
C	Blade chord
C_L	Lift coefficient (Eqn. (8.8))
Cp_o	Total pressure loss coefficient
Cp_s	Static pressure coefficient
E	Voltage
H	Blade span
M	Mach number
M	Molecular weight
P	Static pressure
P_o	Stagnation pressure
R	Gas constant
R_e	Reynolds number
S	Blade spacing (pitch)
t	Blade thickness
V	Absolute flow velocity
Y	Overall loss coefficient
VI	Mean inlet flow velocity
Y_p	Blade profile loss coefficient
Y_s	Secondary loss coefficient
α	Flow yaw angle measured from the cascade axial direction
β	Blade angle with respect to the cascade axial direction
γ	Blade stagger angle

Symbols	Description
δ_1	Inlet boundary layer thickness
δ_1^*	Inlet boundary layer displacement thickness
Δ	Increment
θ	Flow pitch angle
μ	Fluid viscosity
ρ	Fluid density
Σ	Summation
H.P.	Horse power
m/s	Meters per second
r.m.s.	Root mean square
r.p.m.	Revolutions per minute

Subscripts

$_0$	Stagnation
$_1$	Cascade inlet
$_2$	Cascade outlet
a	Axial
m	Arithmetic mean
s	Static
T	Total

CHAPTER 1

INTRODUCTION

When weight and size become a major concern in the design of a gas turbine engine, it becomes necessary to achieve higher stage loading by subjecting the flow to higher turning angles. By doing so, the task of the turbomachine designer becomes increasingly more difficult due to the complex flow régime which exists within the blade passages. Great confidence has not been given to the analysis of potential flow through networks of turbine blades due to these complexities. Methods of analysis for compressor cascades are not generally useful in turbine studies because the flow turning angles through the turbine are much higher and consequently major effects, due to the boundary layers in the endwalls of the cascade, require a three-dimensional analysis of the flow field. Turbine profiles have been developed mainly on an empirical or semi-empirical basis. Considerable progress has been made by utilizing experimental cascade data to provide design information where the fluid flow conditions cannot be suitably resolved. Hence the turbomachine designer has been able to give an accurate assessment of the turbine stage performance if the performance of the equivalent two-dimensional cascade is known. Presently there has not been a sufficient amount of data available for two-dimensional high turning angle turbine blade cascades to

warrant the acceptance of a loss prediction based on the existing loss correlations.

Losses within a cascade are realized when a drop in the total pressure is observed. The total losses are comprised of the profile losses and the secondary losses, which are affected to some extent by the inlet flow endwall boundary layers. In particular it is the secondary flows which affect the gas exit angles and hence the incidence on a subsequent blade row. It is then evident that an efficient turbine design requires a reasonably accurate assessment of these losses and the resulting gas exit angles.

The present study focuses on the effect of the entry endwall boundary layers on the measured secondary losses in a two-dimensional cascade of high turning angle turbine blades. This particular profile was designed at McMaster University by Malhotra {1}* who used an extension of the stream tube method of analysis to account for compressibility. The design technique was later refined by Stannard {2}, who, utilizing these blades, tested a two-dimensional cascade for a series of pressure ratios from 1.5 to 2.62 .

As part of an open circuit wind tunnel, a two-dimensional cascade was constructed with provisions to modify the inner and outer endwall boundary layer displacement thickness. The inlet and exit channels were rectangular in cross-section

---

* Number in { } refers to the Bibliography shown on page 147

and designed to provide inlet and outlet gas angles equal to the design inlet and outlet blade angles (64^{o} and 64^{o} - 30' respectively). The inlet channel was connected to a rectangular horn-shaped duct which provided uniform throat velocities. Four blades made up the cascade and the centre passage (test passage) was fully instrumented with static pressure taps.

Chapter 3 provides detailed information on the overall test facility. The instrumentation is described in Chapter 4 and Chapter 5 outlines the aims of the experimental investigations. Chapter 6 examines the inlet flow conditions and Chapter 7 the static pressure distribution on the surfaces of the test passage. Chapter 8 provides a series of loss contour plots which show the effect of varying the inlet boundary layer displacement thickness. The calculated losses are tabulated and compared with existing correlations.

CHAPTER 2

LITERATURE SURVEY

The turbomachine designer must have a reasonably accurate account of the distribution of gas angles and deflections through a cascade in order to make a comparison with the gas angles which were specified in the original choice of velocity triangles. It is the designers task to obtain a work output from the gas by achieving the appropriate gas deflection with the least irreversibilities. These irreversibilities within a blade row or cascade are observed when a drop in the total pressure occurs due to viscous effects.

The overall pressure loss in a blade row is normally subdivided into a number of component losses, each of which may be a function of various aerothermodynamic or geometric parameters which will be given further consideration within this chapter. Several authors {3},{4},{5},{6},{7},{8},{9} {10},{11},{12},{13},{14} have given a partial or full account of these losses which may be summarized as follows:

(a) Profile Loss

When a viscous fluid flows past a body at rest, forces due to pressure and viscous shear act over the body surface (pressure and shear forces act normal and tangential to the surface respectively). The profile loss is attributed to the

components of these pressure and shear forces which act in the direction of the fluid with respect to the body{15}. Flow separation, particularly on the blade suction surface, may also be considered as part of the profile loss. Factors affecting the growth of the boundary layer include the velocity distribution, Reynolds number, turbulence level and blade surface roughness.

(b) Secondary Loss

Lakshminarayana et al.{8} reported that secondary flow "...may be defined as the difference between the actual and the idealized axisymmetric flow." and that this flow phenomenon "...is known to constitute a major portion of the total losses ." Louis {9} attributed the action of the secondary flow within the blade passage to the low momentum boundary layer fluid (adjacent to the annulus or cascade endwalls) which cannot negotiate the same turning as the high momentum main fluid. Due to the cross channel pressure gradients, the low momentum fluid is swept toward the junction of the suction surface and the annulus or cascade endwall where it accumulates, rolls up the blade suction surface and separates into a concentrated vortex core (termed the 'Passage Vortex') which is discharged at the trailing edge of the blades. The secondary loss is concentrated within the regions of low stagnation pressure which make up these vortex cores. This description has been verified by extensive flow visualization studies carried out by Herzig et al.{16}.

Another secondary motion has been observed in the passage and is due to vortices trailing from the previous blade row. These vortices may arise from variable blade circulation and are termed 'Mainstream Secondary Flow'.

(c) Annulus Loss

This loss is associated with the boundary layer on the endwalls of a row of blades or a cascade. Several authors have adopted the practice of considering the annulus loss as part of the secondary loss because it is hard to make a definite discernment between them.

(d) Tip Clearance Loss

These are due to the leakage of flow through the blade tip clearance or to the clearance space around shroud bands, if any are present. Figure 2.1 provides a pictorial description of the secondary flow and vorticies which may occur in a turbine blade row. The reader can appreciate the order or magnitude of the aforementioned losses by referring to Figure 2.2 .

A study of the secondary flow phenomenon depicted in Figure 2.1 provides some insight into Horlock's statement that "...a complete analytical solution to the compressible flow through turbine cascades of high deflection has not yet been obtained " . It becomes evident that the prediction of the secondary loss is best obtained through correlations which have been formulated from cascade test data.

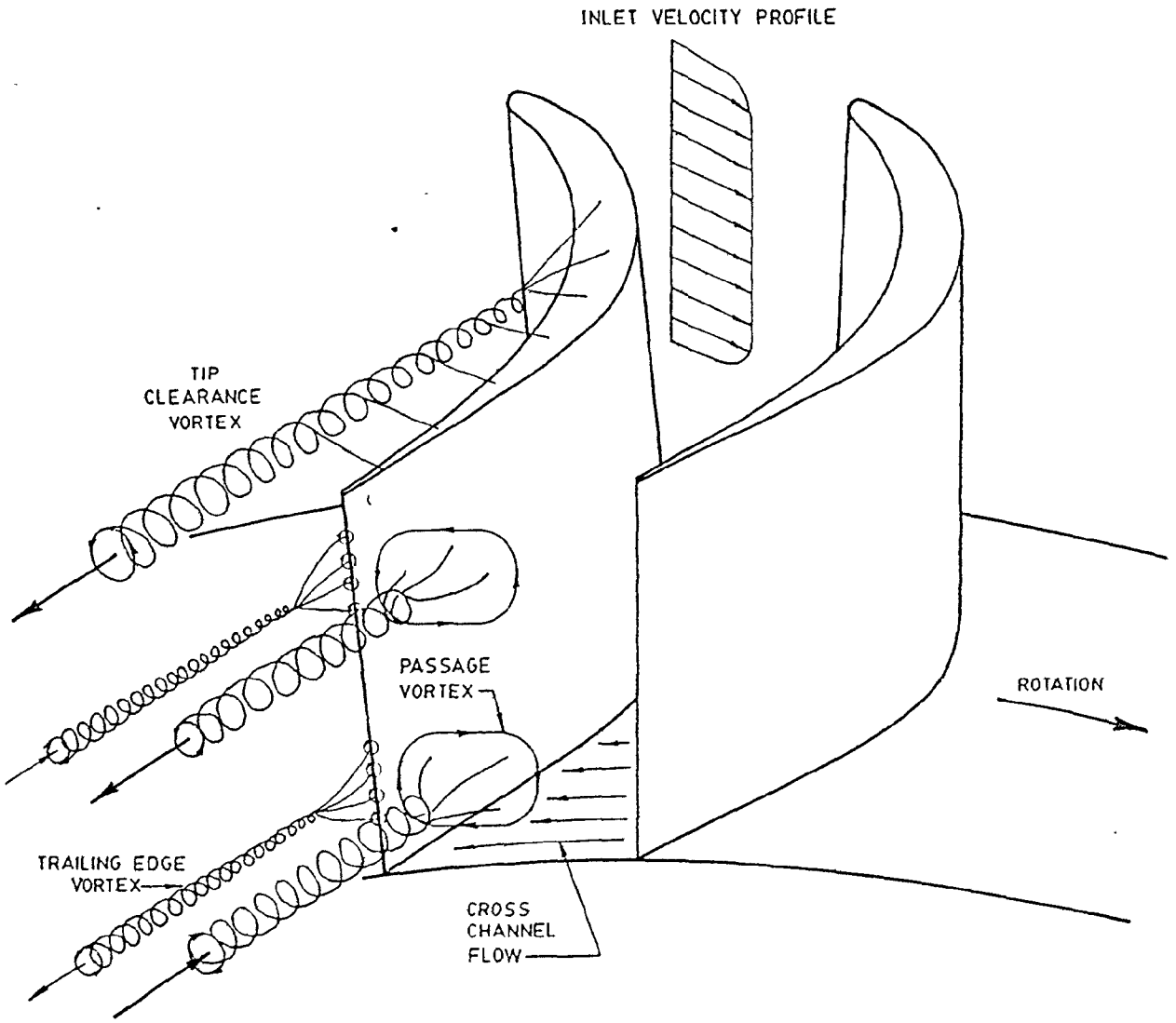

Figure 2.1 Secondary Flow and Vortices Occurring in a Turbine Blade Passage.

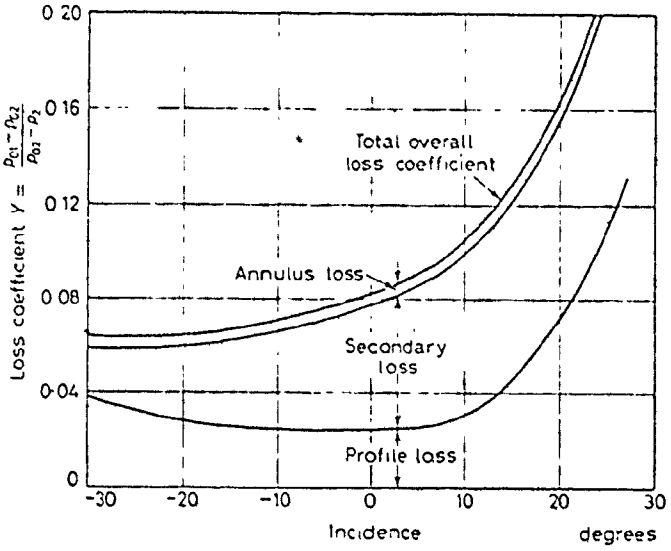

Figure 2.2 Example of Flow Losses Through a Row of Turbine Blades (Taken from Reference {18}).

Elshammaa {17} gave an excellent review on the theoretical analysis of secondary flow and pointed out that there are generally two established avenues of approach. One method deals with the passage vortex and is termed 'Secondary Flow Theory' and the other attempts to analyze the three dimensional endwall boundary layer. The 'Secondary Flow Theory' attempts to determine the deviation in the gas exit angles, the secondary flow with its associated streamlines and the resulting streamwise vorticity leaving the cascade. Elshammaa {17} pointed out that the solution of the mathematical formulations requires several "...simplifying assumptions..." requiring the flow to be "...steady, inviscid, rotational, incompressible and with no body forces". The 'Secondary Flow Theory' is unreliable when dealing with high turning cascades because viscous effects and possible flow separation within the passage are not accounted for.

Endwall boundary layer calculation schemes for high turning cascades have not been used to predict performance because their derivation restricts them to small flow turning. The solution requires that the endwall boundary layer be originally in line with the mainstream flow which is not the case within high turning cascades. In high turning cascades, the boundary layer fluid is swept towards the blade suction surface. The calculation schemes assume that the endwall boundary layer has no pressure gradient perpen-

dicular to the wall which may not be true and no account is made for the possibility of flow separation due to the excessive turning of the boundary layer fluid.

Because of the great difficulties and unrealistic assumptions associated with the analytical solution of the secondary flow phenomenon, the designer has had to resort to the correlations derived from experimental data. Horlock {18} attended to this with his statement "...relatively few designers have used these theoretical methods in their blade designs". Came { 5 } stated that the "...estimates of the secondary loss to date have been based upon empirical expressions derived from cascade data", because viscosity effects and boundary layer behaviour have not been "...sufficiently well understood..." to the point where they could be included into the theoretical solutions of the secondary flow.

The two most common methods of presenting the losles within a turbomachine are by the total pressure loss coefficient and by the enthalpy loss coefficient. These coefficients are normally non-dimensionalized on the mean inlet or outlet dynamic head. The losses are correlated to non-dimensional groupings of aerothermodynamic or geometric parameters through expressions which have been empirically or semi-empirically derived from extensive cascade data.

For compressible flow through a cascade, Horlock

{18} stated that the overall mean total pressure loss is a function of several parameters:

$$\Delta P_0 = P_{01} - P_{02} \tag{2.1}$$

= f (blade geometry, incidence, spacing S, blade chord C, blade span H, fluid density ρ, blade thickness t, velocity V, viscosity μ, boundary layer thickness δ_1, entry boundary layer parameters and turbulence level).

Non-dimensionally this expression becomes:

$$Y = \frac{\Delta P_0}{\frac{1}{2}\rho V^2} = f\ (R_e, \text{ incidence, blade geometry, } S/C, H/C, t/C, \delta_1/C, \text{ entry boundary layer parameters and turbulence level}). \tag{2.2}$$

For compressible flow, the same non-dimensional parameters are included plus others allowing for compressibility:

$$Y = f\ (R_e, \text{ incidence, blade geometry, } S/C, H/C, t/C, \delta_1/C, \text{ entry boundary layer parameters and turbulence level, } M_2, \gamma, R \text{ or } M). \tag{2.3}$$

The overall or total losses may be correlated against all the non-dimensional groups which is the basis of Soderberg's {18} correlation or the separate losses (profile and secondary) may be correlated with the appropriate parameters which is the basis of Ainley and Mathieson's {13} method.

The total pressure loss coefficient Y can be measured relatively easily in cascade tests and is the one most often reported in the literature. Several authors

{6} , {18} , {19} have shown that for low inlet Mach numbers (less than 0.4) the enthalpy and total pressure loss coefficients are almost numerically identical and Cohen {19} and Horlock {18} have developed expressions which show the relationship between the loss coefficients and the stage isentropic efficiency.

Ainley and Mathieson {13} were the first to present a detailed scheme to predict the profile and secondary losses and their correlations are still widely used in modern gas turbine design. Baljé and Binsley { 3 } presented a graphical method of displaying contours of profile loss coefficients against a variety of inlet and outlet gas angles. The associated profiles of optimum pitch to chord ratio are also provided. Recently Denton { 6 } reviewed and compared seven profile loss prediction methods with seventy-nine sets of cascade test results and found that none of them predicted the loss very accurately. He concluded that losses obtained from calculations of blade surface velocity distribution and boundary layer growth would likely yield a more accurate result.

Baljé and Binsley { 3 } and Horlock et al.{20} stated that there is little effect of the Reynolds number on the profile losses in a turbine or turbine cascade above $R_h = 10^5$ (where R_h is based on the outlet velocity and the hydraulic mean diameter at the throat). Below this value, the profile losses are shown to be proportional to:

$$\left\{\frac{10^5}{R_h}\right\}^{\frac{1}{2}} \qquad (2.4)$$

Baljé and Binsley {3} pointed out that the endwall losses are also subject to the Reynolds number influence. Because a significant part of these losses are attributed to the cross-channel flow of the boundary layer fluid, the influence is not significant and no Reynolds number effect has been assumed for the endwall losses.

Dunham {7} has made an attempt to examine the large amount of experimental data available from both compressor and turbine cascade tests with the hope of providing a physical understanding of the mechanisms of secondary flow and to produce a loss correlation. He has tabulated and reviewed thirteen incompressible forms of the various formulae for expressing the total pressure loss coefficient for secondary flow. Each of the correlations is a product of two terms:

(a) a loading term which represents the effect of cascade loading or deflection

(b) a length ratio term equivalent to a length associated with the secondary loss/blade span.

Based on his extensive examination of these formulae, Dunham { 7 } was able to derive a more embracing correlation for the secondary losses. His expression has been more successful in correlating the effect of blade loading on the secondary losses and he has provided a tentative expression (subject to change with further cascade data) for the inlet boundary layer effect. The correlation derived for Y_s is of the form:

$$Y_s = \frac{C}{H} \frac{C_L^2}{(S/C)^2} \frac{\cos^2\alpha_2}{\cos^3\alpha_m} \frac{\cos\alpha_2}{\cos\beta_1} \left(0.0055 + 0.078\sqrt{\frac{\delta_1^*}{C}}\right) \quad (2.5)$$

The boundary layer function shown in parenthesis is composed of two terms. The first term is the downstream wall boundary layer component, initially considered a constant, and the second term is the vortex core loss component, which is considered to be a function of δ_1^*/C .

In a more recent publication, Came { 5 } conducted a series of secondary loss measurements on a large scale cascade of turbine blades with a maximum gas turning angle of 84.2^o. Measurements were taken with a varying inlet wall boundary layer thickness and a varying inlet angle. The results were presented in the form of total pressure loss contours and spanwise variations (of pitchwise averaged losses) as functions of the inlet conditions. From his studies, Came presented a loss correlation for Y_s which can be written as:

$$Y_s = \frac{C_L^2}{(S/C)^2} \frac{\cos^2\alpha_2}{\cos^3\alpha_m} \frac{\cos\alpha_2}{\cos\beta_1} \left(0.025\ Y_1^* + 0.009\ \frac{C}{H}\right) \quad (2.6)$$

where Y_1^* defines the mass averaged inlet boundary layer loss. Came's experimental results were shown to be in good agreement with Dunham's correlation.

Dunham and Came {21} have recently performed detailed comparisons between the predicted and measured losses of sixteen turbines and have proposed changes in the widely used empirical formulas for profile, secondary and tip

clearance losses established by Ainley and Mathieson {13}. Their expression for the secondary loss coefficient was given as:

$$Y_s = 0.0334 \frac{C}{H} \frac{\cos\alpha_2}{\cos\beta_1} Z \qquad (2.7)$$

in place of Ainley's:

$$Y_s = \lambda Z \qquad (2.8)$$

where λ is an empirical function (see Reference {13}) and Z is Ainley's loading parameter defined as:

$$Z = \frac{C_L^2}{(S/C)^2} \frac{\cos^2\alpha_2}{\cos^3\alpha_m} \qquad (2.9)$$

The blade profile used in the present study (described in Chapter 3) was tested in a two-dimensional cascade by Stannard {2} who looked at the effects of incidence and pressure ratio on the blade surface pressure distributions. Recently Moustapha {22} and Elshammaa {17} tested the same profile in an annular test rig. Elshammaa reported on the secondary losses and found them to be significantly lower than those predicted by correlations. He suggested that a two-dimensional test rig be built in order to assess the influence of the annular rig radial pressure gradients and the varying pitch/chord ratio on the location of the secondary vortices at the cascade exit. He hoped that the extent of these effects could be realized through the study of the difference in the performance of the two rigs.

Conclusions

1) The analytical solutions to the secondary flow

phenomenon require too many simplifying assumptions and are not applicable to high turning angle profiles.

2) No correlation for secondary loss is entirely satisfactory.

3) Secondary losses are imperfectly understood and more data from two-dimensional high turning angle blade cascades must be made available in order to update the existing correlations making them more useful to the designer.

4) There is a need for further investigations on the effect of the inlet boundary layer on the secondary losses.

CHAPTER 3

THE TWO-DIMENSIONAL TEST RIG

3.1 Overview

In order to accurately investigate the free stream and secondary flow phenomena, it is necessary to take a large number of fluid measurements upstream and downstream from a turbine blade row. It is, therefore, desirable to construct test facilities which minimize the probe size effect on the flow and allow for more representative fluid measurements. To this end, a large scale two-dimensional test facility was designed and constructed with these considerations in mind.

The rig was an open circuit wind tunnel comprised of three main components: an inlet section, a high turning angle turbine blade cascade and an outlet section. The design incorporated the means to control the inlet flow parameters in the pitchwise direction and it was also possible to adjust the inlet endwall boundary layers. The main components of the test facility are shown schematically in Figure 3.1.

In order to determine the appropriate lengths of the inlet and exit channel, it was decided to solve Laplace's equation (the differential equation of the velocity potential) in two dimensions using an electrical analogue technique.

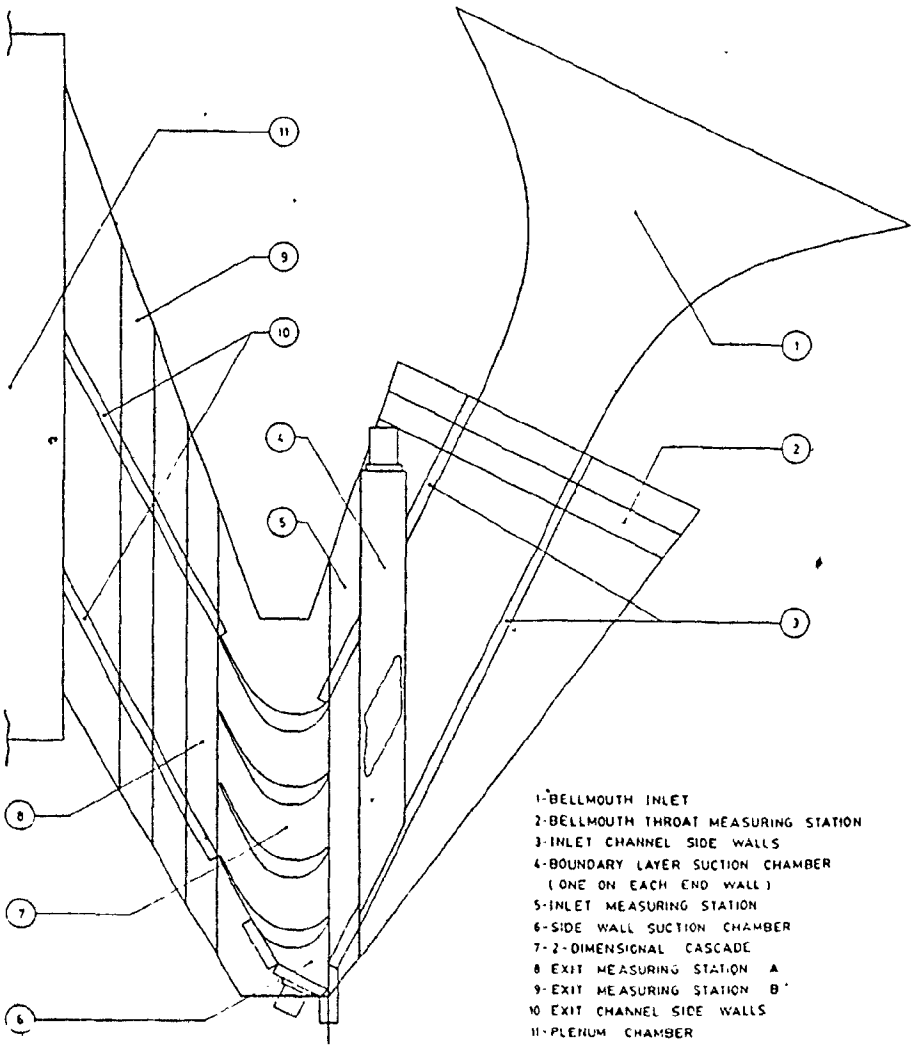

Figure 3.1 Plan View of the Two-Dimensional Cascade Test Rig.

A full scale representation of the cascade geometry (with the appropriate inlet and outlet angles) was constructed from a special conductive surface, carbon impregnated paper. A Kelk Field Plotter Model P103 was used to apply a potential difference across the cascade and a stylus (part of the Kelk apparatus) was used to probe the conductive surface establishing a plot of the lines of constant voltage potential. This method assumes that the flow is steady, incompressible, inviscid and irrotational and that the voltage potential is analagous to the velocity potential. By observation of the trends in the lines of constant velocity potential, it was possible to select an appropriate inlet and outlet channel length. The results of this plot are shown in Chapter 6 Figure 6.5.

3.2 The Inlet Section

A rectangular bellmouth entrance duct and a straight rectangular channel made up the inlet section. A detailed description of the bellmouth entrance duct is given in Appendix 3 {23}and is shown schematically in Figure 3.2. The dimensioned portions in Figure 3.2 are the orthographic projections of the width and height of the entrance duct and the remaining two drawings are representations of the development drawings which were used in its construction. A local sheet metal fabricator assembled the duct from 16 gauge galvanized sheet steel by arc-welding the seams.

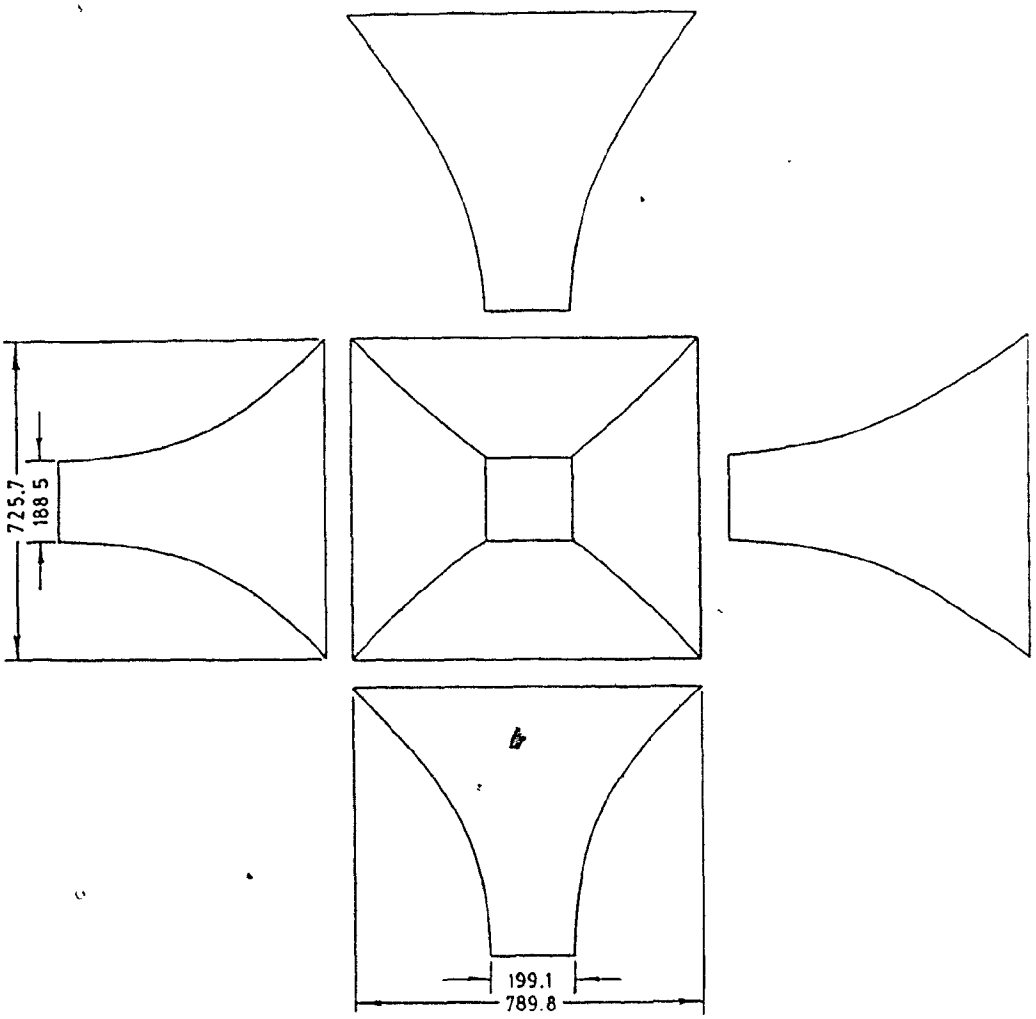

Figure 3.2 The Bellmouth Entrance Duct.

At both the opening and the throat, flanges were turned out at an angle of 90^{o}. The throat flange was fastened to the rectangular inlet channel and a framework of half-round pine wood was attached to the opening of the duct to eliminate any sharp edge effects. The inside seams were filletted with an automotive body filler and the entire assembly was painted.

The inlet channel sidewalls were made from 16 gauge stainless steel sheet and their surfaces were inclined at an angle of 64^{o} to the cascade axial direction. Their edges were turned out at an angle of 90^{o} and were fastened to the cascade rig top and bottom endwalls. These endwalls were made of 12 mm clear acrylic plastic to facilitate instrumentation and possible future flow visualization studies.

The inlet measuring station was located on the outer endwall (Item 5 Figure 3.1). It consisted of a removable segment, whose centre line was located at an axial distance of 27.5 mm ahead of the leading edge of the blades {17} and defined the edge of the plane in which the inlet flow parameters were measured. A similar measuring station (Item 2 Figure 3.1) was provided in order to study the flow characteristics at the bellmouth throat.

The boundary layer suction chambers (one on the inner endwall and one on the outer endwall) were installed immediately adjacent to and upstream of the inlet measuring

station (Item 4 Figure 3.1). The boundary layer suction in each chamber was applied through a network of 252--2 mm diameter holes. These holes were drilled through the inlet channel endwalls with the pattern shown in Figure 3.3 and the rows ran parallel to the inlet channel sidewalls. An integral 2.5 H.P. (1865 watts) A.C. electric motor-fan unit, capable of delivering a pressure equivalent to -39.9 cm water (-15.7 inches) was connected to each suction chamber via a flexible 5.1 cm (2 inch) cloth heater-type hose. The suction was regulated by a gate valve which was installed in series with the flexible hose.

Flow control was provided in the pitchwise direction by a sidewall suction chamber (Item 6 Figure 3.1) which was connected to a Sheldons 1403-B exhauster fan with a flexible cloth hose. The fan was driven by a Reliance 3 H.P. (2238 watts) D.C. electric motor and the speed controlled by a Variac. It was possible to regulate the suction with the Variac or from within the sidewall suction chamber by the positioning of a movable perforated plate which ran parallel to the cascade blade tips. The inlet section components can be seen in the photographs shown as Figures 3.4, 3.5, 3.6 and 3.7.

3.3 The Two-Dimensional Cascade Section

Because large scale test facilities pass high mass flow rates, it was necessary to limit the number of turbine

blades to four (three flow passages). The cascade geometric parameters (Item 7 Figure 3.1) are given in Table 3.1. The high turning angle turbine blades were of the flat back type and the profile was designed by Malhotra [1] (Figure 3.8). The two centre blades, made of aluminum, were manufactured by the Division of Mechanical Engineering, National Research Council in Ottawa. These two blades formed the test passage and were instrumented (Chapter 4) for static pressure measurements by the McMaster University Instrument Machine Shop. The outer two blades were cast, in a Plaster of Paris mold, from an opaque low shrinkage acrylic. These were later hand-sanded and painted and served as sidewalls to guide the flow around the test passage.

3.4 The Exit Section

A rectangular exit channel, similar in construction to the inlet channel, formed the basis of the exit section. The stainless steel sidewalls were actually extensions of the trailing edges of the end two blades and were therefore, inclined at an angle of 64.5° to the cascade axial direction. The outer endwall of the exit channel had two removable segments whose centrelines defined the edges of the planes of exit measuring stations A and B (Figure 3.1). The centreline of exit measuring station A was located at an axial distance of 27.5 mm downstream of the trailing edge

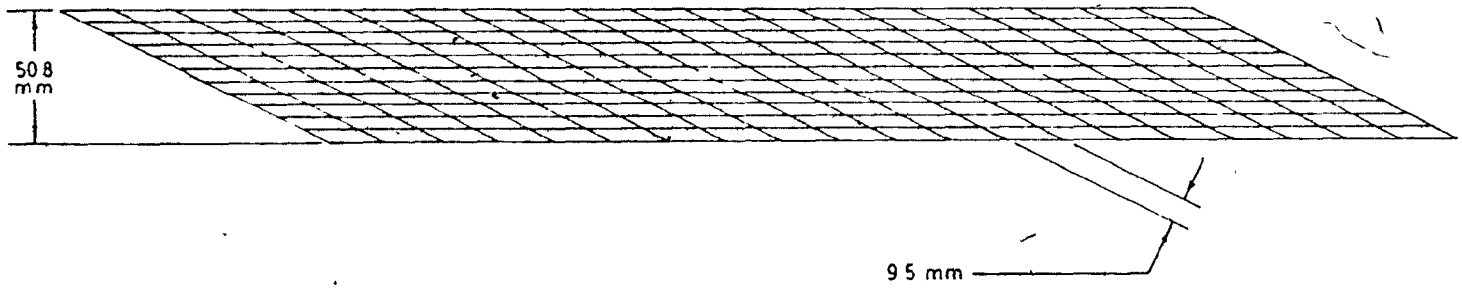

Figure 3.3 Hole Pattern Used in the Inner and Outer Endwall Boundary Layer Suction Chambers (252 Holes in Each Chamber).

CAPTIONS FOR FIGURE 3.4

A Traverse Mechanism

B Outer Endwall Boundary Layer Suction Chamber

C Inlet Bellmouth Duct

D Manometer Switching Station

E Boundary Layer Suction Fans

F Sidewall Suction Chamber

G Inlet Channel

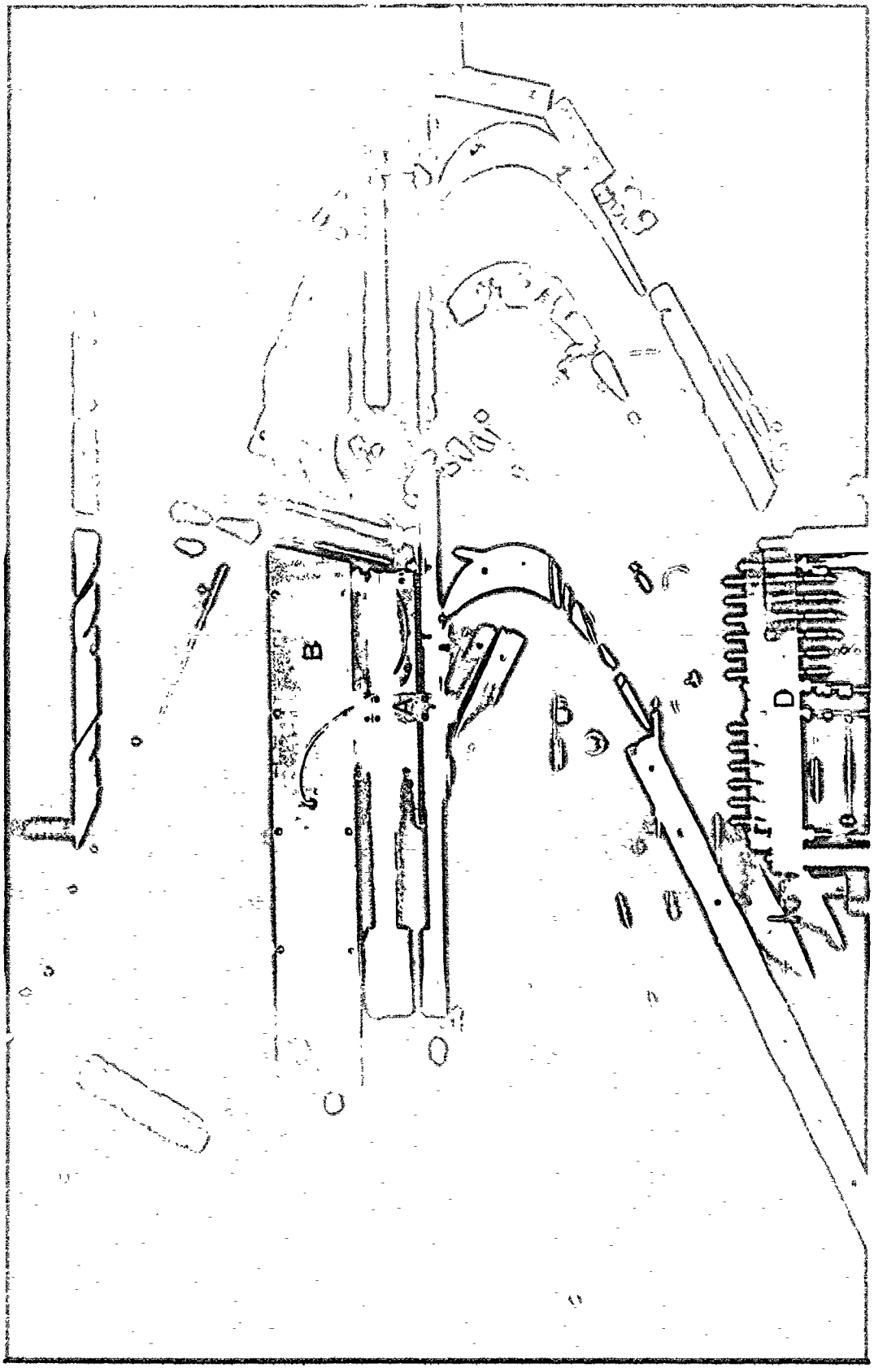

Test

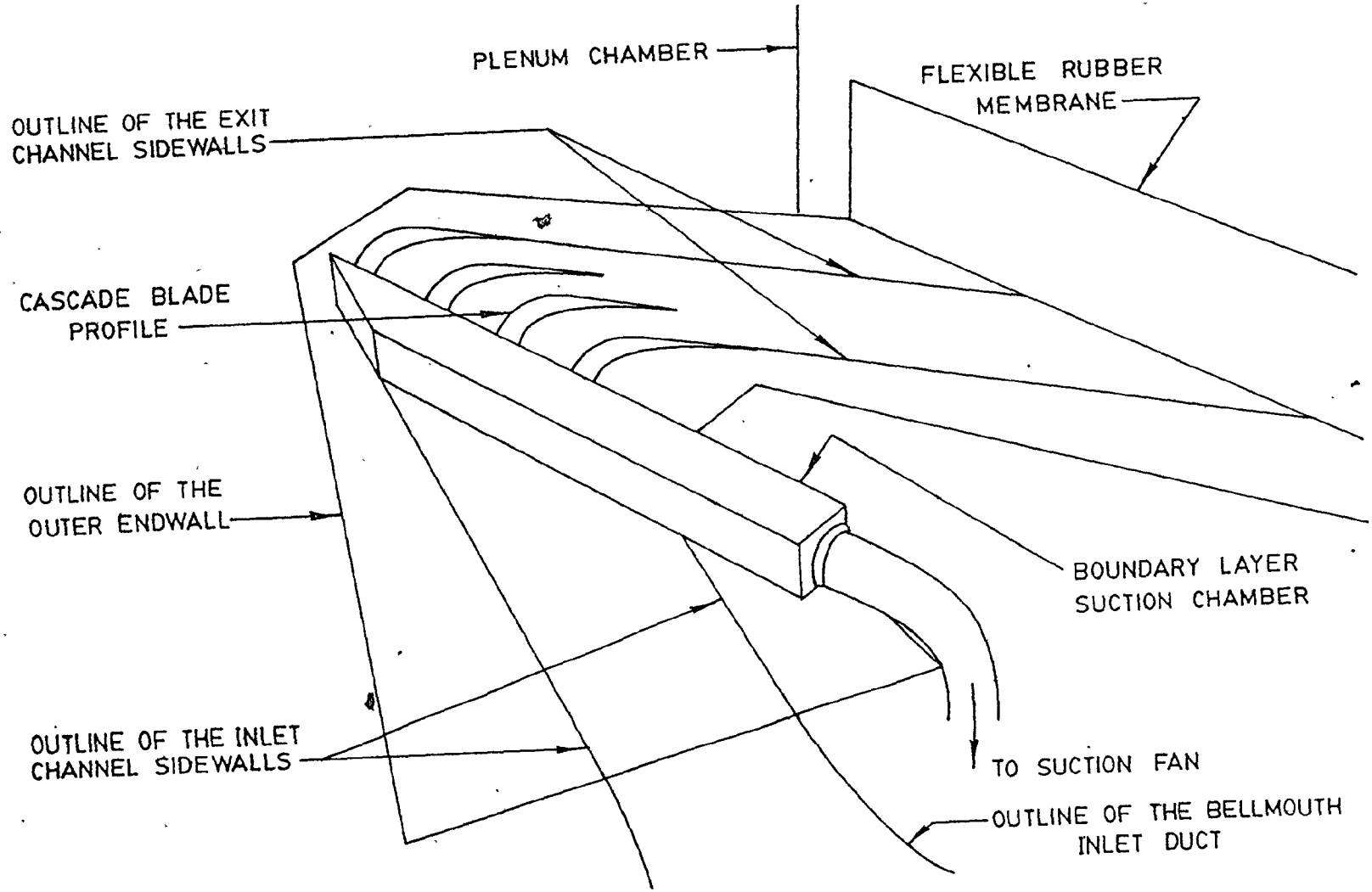

Figure 3.5 a) Overview for Figure 3.5 b).

CAPTIONS FOR FIGURE 3.5b)

A Inlet Bellmouth Duct

B Boundary Layer Suction Hole Pattern at the Inner Endwall

C Flexible Rubber Membrane

D Plenum Chamber

E Outer Endwall Boundary Layer Suction Chamber

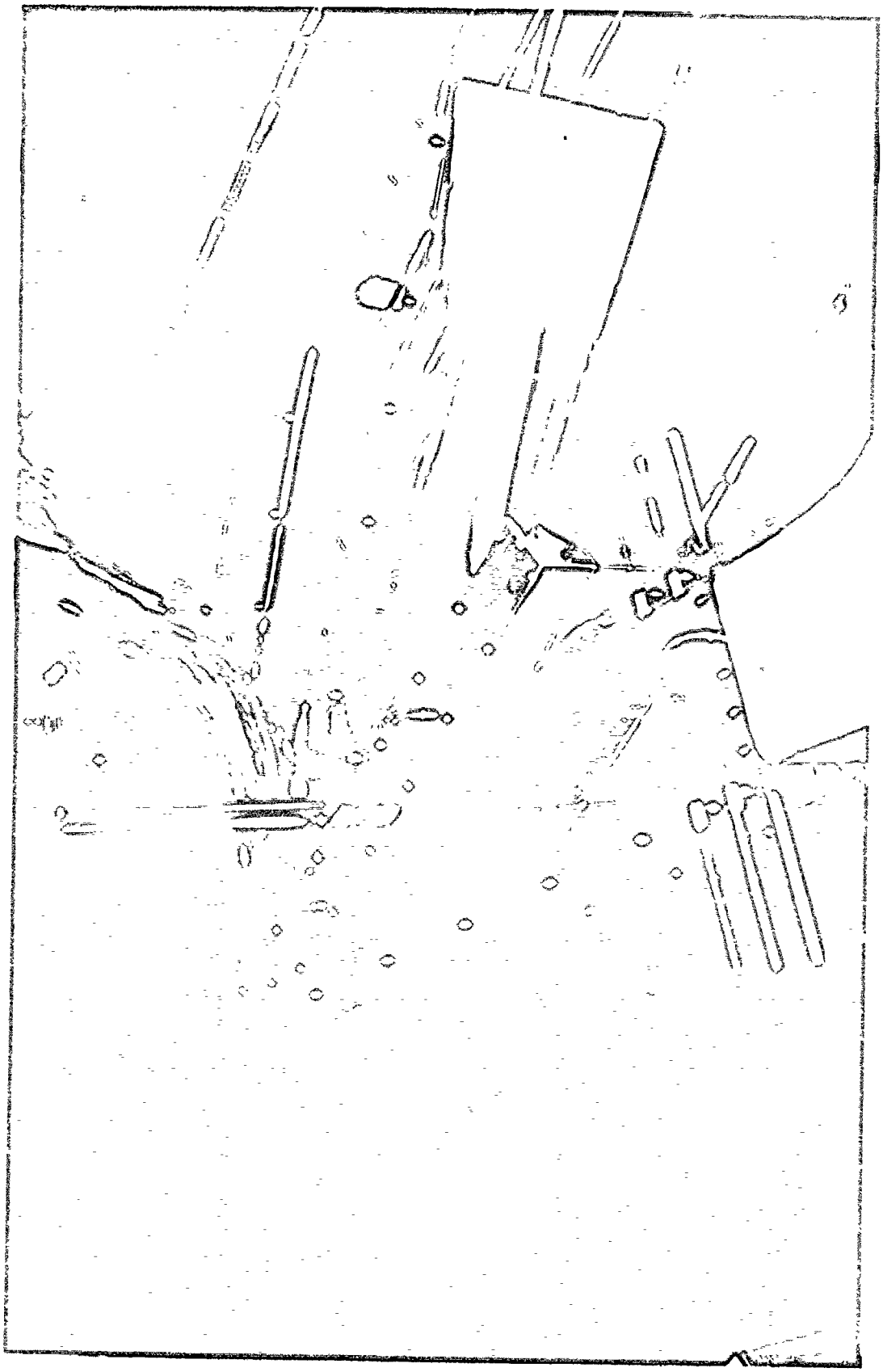

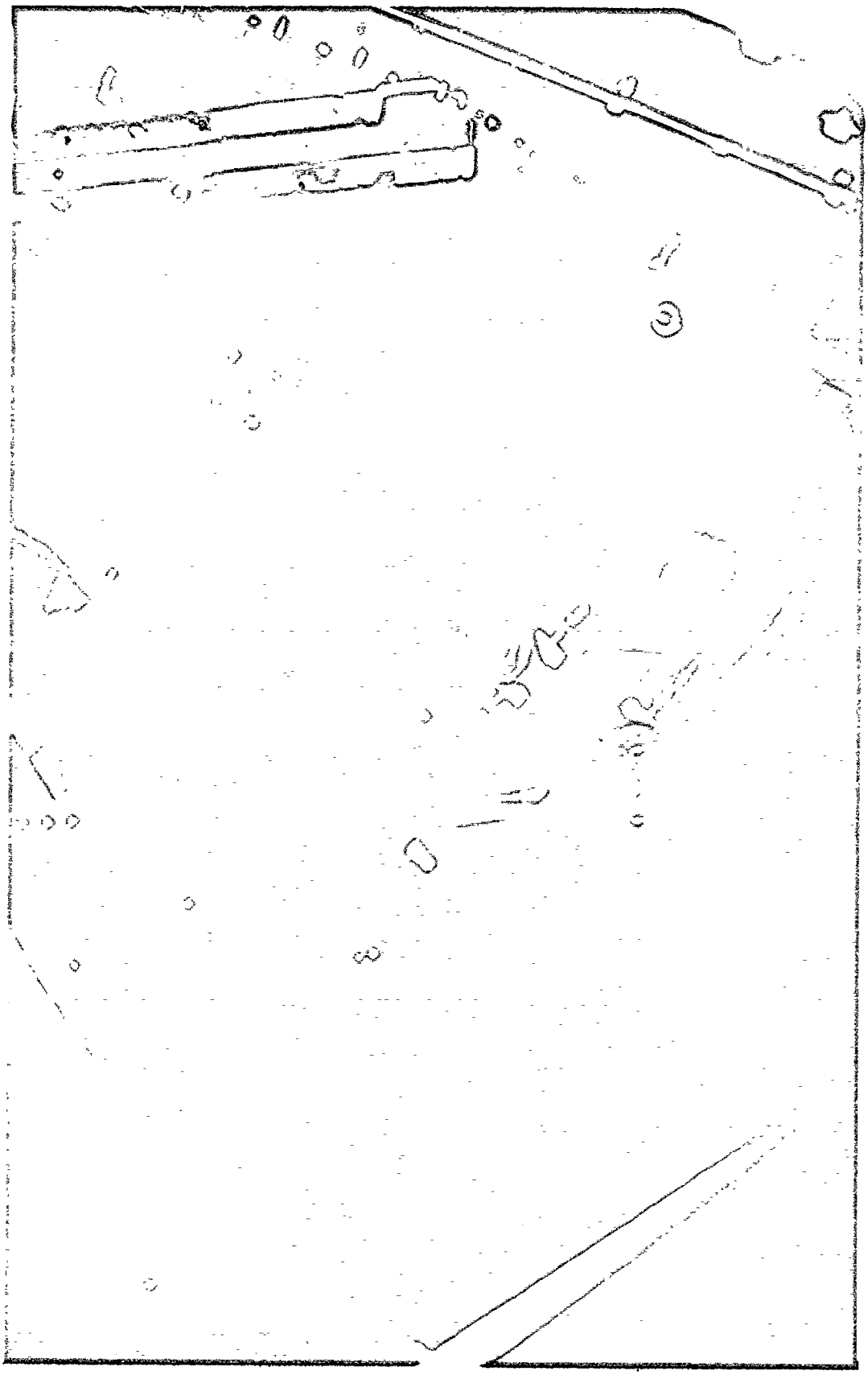

CAPTIONS FOR FIGURE 3.7

A Inlet Bellmouth Duct

B Inlet Channel Sidwalls

C Plenum Chamber

D Manometer Switching Station

E T.E.M. Instruments Multitube Manometer

F Plenum Chamber Exhaust Duct

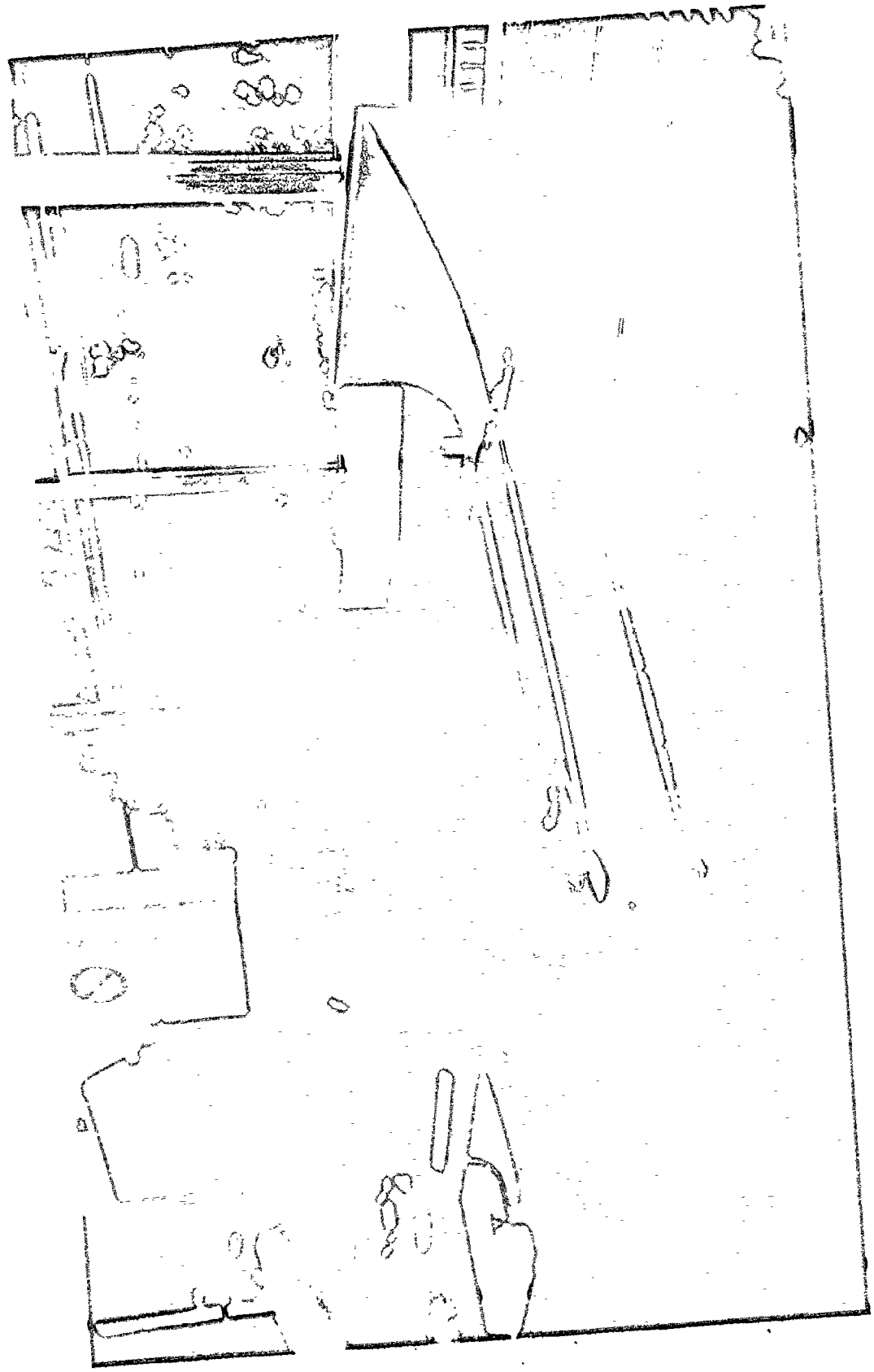

of the blades and station B at a streamwise distance of 1.5C.

3.5 The Test Rig Air Supply and Associated Components

The general layout of the entire test facility is shown schematically in Figure 3.9. Air was drawn through the cascade test rig by means of a Sheldons XB-19 Exhauster Fan capable of delivering 538.59 m^3/min (19020 ft^3/min) against a 15.24 cm (6 inch) static head of water at 13.87 K watts (18.6 H.P.) and 1282 r.p.m. The fan was driven by a BKB D.C. electric motor with a maximum power output of 18 K watts (24 H.P.) at 3000 r.p.m. and its speed was controlled by a power-stat. Vibrations within the test section were eliminated by using a flexible rubber membrane to connect the exit channel to the plenum chamber (see Figure 3.7). The entire portion of the test facility downstream from the cascade exit section was constructed by Moustapha {22} and Elshammaa {17}.

Table 3.1

Geometric Parameters of
The Two-Dimensional Cascade

Blade Turning Angle	128.5^{o}
Blade Inlet Angle	64^{o}
Blade Outlet Angle	64.5^{o}
Blade Chord (C)	214 mm
Blade Height (H)	188.5 mm
Blade Axial Chord	188.5 mm
Cascade Aspect Ratio (Blade Height/Blade Axial Chord)	1.0
Blade Pitch or Spacing (S)	124.68 mm

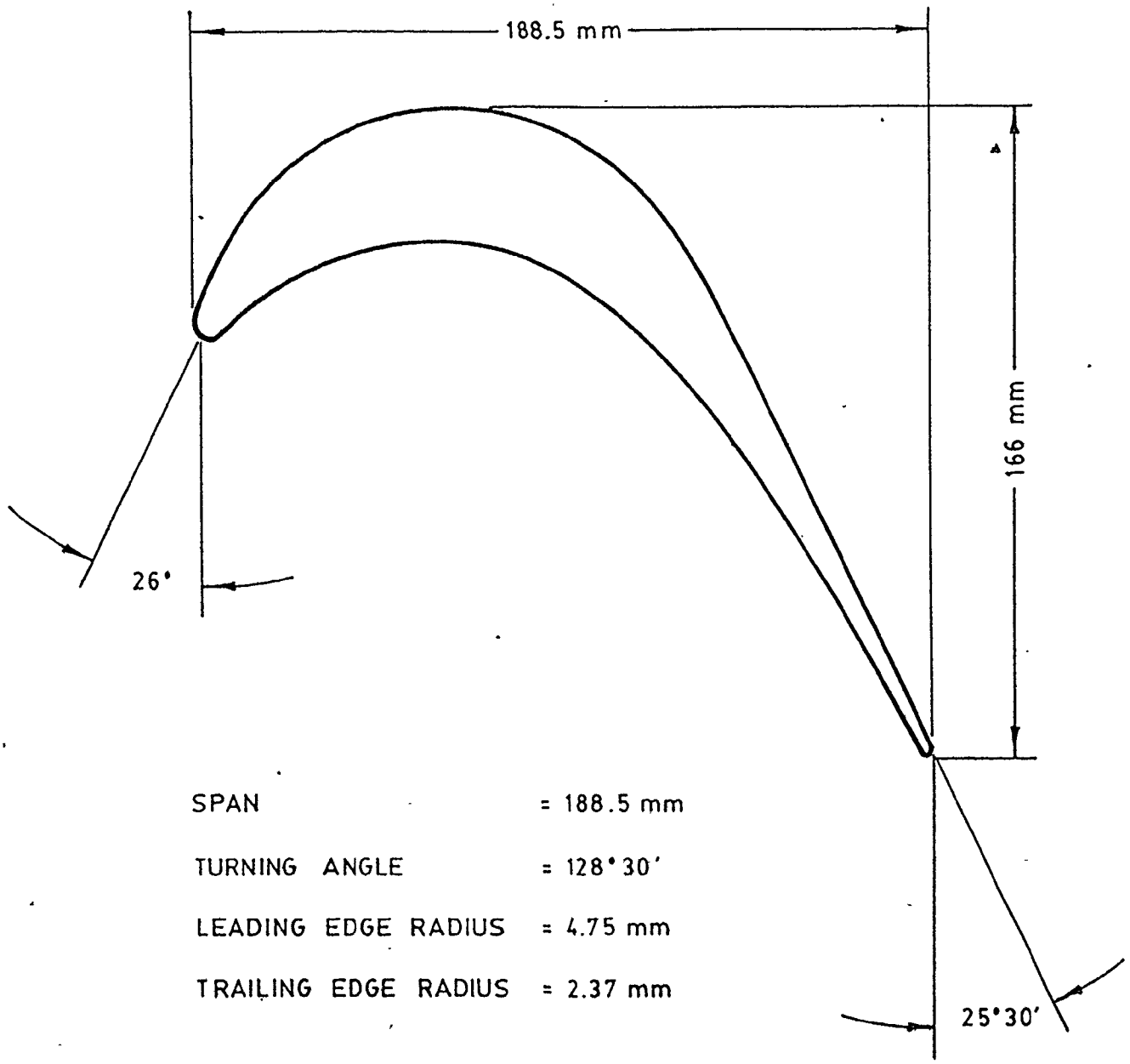

Figure 3.8 The Turbine Blade Profile.

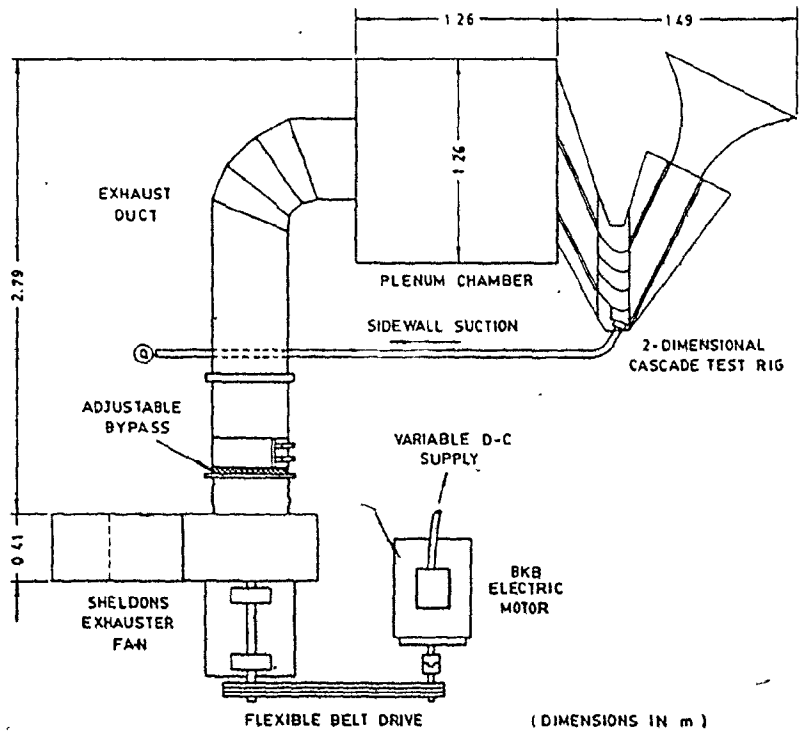

Figure 3.9 Schematic Representation of the Overall Test Facility.

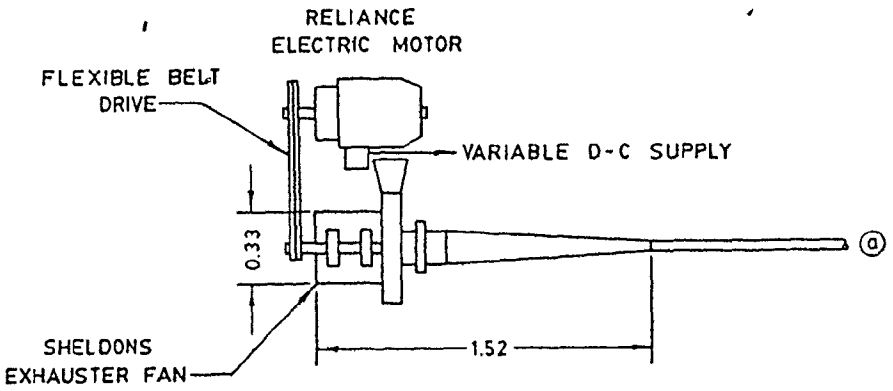

Figure 3.9 (Continued).

CHAPTER 4

INSTRUMENTATION

In order to carry out the investigation, it was necessary to measure the fluid flow parameters (of pressure and temperature) at several locations within the cascade test rig. The instrumentation required to accomplish this can be categorized as follows:

1. Main flow instrumentation at the bellmouth throat and at the inlet and exit measuring stations of the cascade.
2. Boundary layer instrumentation in the inlet channel.
3. Blade test passage instrumentation.

4.1 Main Flow Instrumentation

The main flow was traversed in the spanwise and pitchwise directions at each of the four measuring stations shown in Figures 3.1 and 4.1. The geometric projection (at the blade inlet angle of 64^{o}) of the centre of passage I (Figure 4.1) onto the plane of the inlet measuring station defined the origin for the flow measurements. From the origin, the flow was traversed in the pitchwise direction towards passage III in 20 mm increments and in the spanwise

direction at various percentages of the blade span. The geometric projection of the centre of passage III (at the blade exit angle of 64.5^{o}) defined the origins on the two exit measuring station planes. The exit flow traverses were done in 20 mm increments towards passage I. The flow traverses, taken at the inlet and exit measuring stations, normally covered a distance of 2S.

4.1.1 The Traverse Mechanism

A grid of probe positions was established from linear, orthogonal movements of the traverse mechanism shown in the photo of Figure 3.4. The pitchwise movement was provided by a sliding T-shaped member which was mounted in bearings between two rigid longitudinal supports. A rack and gear assembly, used in conjunction with an attached scale and vernier, could locate pitchwise positions to an accuracy of 0.1 mm. This component of the mechanism was fabricated by the McMaster University Instrument Machine Shop. The component for the spanwise movement was mounted on top of the T-shaped member and had a range of 254 mm (10 inches). The lead screw had a thread pitch of 1.27 mm (0.05 inches) and, with the hand wheel graduated into 50 divisions, spanwise positioning to 0.0254 mm (0.001 inch) was possible. The probes were fastened to this spanwise component via a United Sensor and Control Corp. 360^{o} protractor and vernier turntable attachment. With the scale and vernier, the flow yaw angle could be measured to 0.2^{o}.

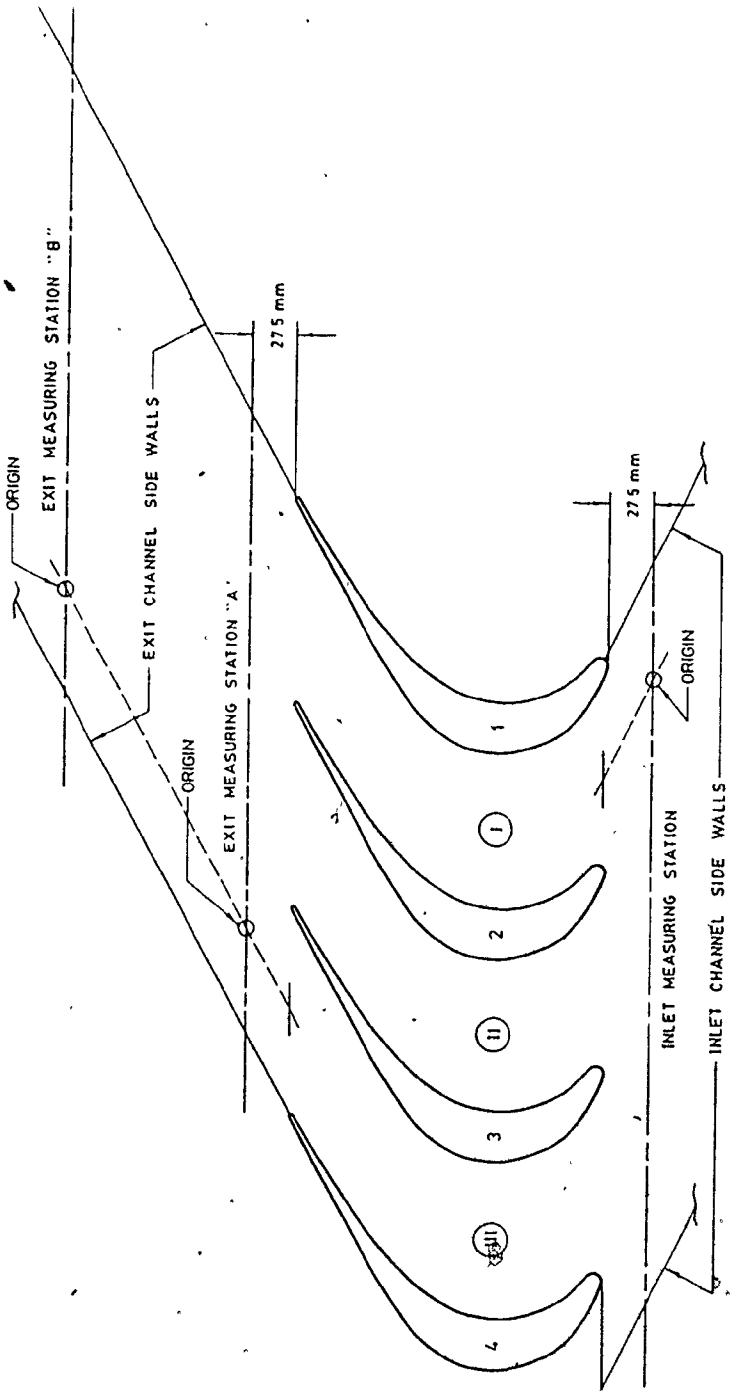

Figure 4.1 Cascade Inlet and Exit Measuring Stations.

4.1.2 Mainstream Measurements

A United Sensor L-4147-2 pitot-static probe, with a sensing head diameter of 1.587 mm (0.0625 inches) was used to measure the dynamic pressure in the bellmouth throat measuring plane. In this plane, a static pressure measurement was provided by a static tap which was installed in the inlet channel endwall.

A specially designed triangular shaped wedge probe {24} was used to measure the flow yaw angle at the cascade inlet and exit measuring stations. The static pressure taps on the two adjacent surfaces of the probe were connected to a water-filled U-tube manometer. When the probe was properly aligned with the flow, the static pressures were equal and the corresponding flow angle was recorded. The angle measurements were made with respect to the cascade axial direction.

Due to its relative insensitivity to flow direction ($\pm$ 30°) {25}, a United Sensor KCF-12-W Kiel Probe was used to record the total pressure at the cascade inlet measuring station and a wall static tap, in the same plane, provided a static pressure measurement. The Kiel Probe had an external tube diameter of 6.35 mm (0.250 inches).

Measurements in the planes of the two exit measuring stations were taken with a United Sensor B1211 2 five-hole three-dimensional probe. The probe had a sensing head diameter of 3.175 mm (0.125 inches) and a main shaft

diameter of 6.35 mm (0.250 inches). The probe head was designed to have five pressure sensing ports which were connected, via the main shaft, to a semi-circular block containing five stainless steel tubes labelled 1 through 5. At the sensing head, a centre port, 1, measured the total pressure. The two lateral taps 2 and 3 were used for nulling and static pressure measurements and pitch angles were determined from pressure measurements at the top and bottom taps 4 and 5. At each grid point in the measuring plane, the probe was set to the appropriate yaw angle (determined with the wedge probe) and the pressures indicated by the five taps were recorded. The manufacturers' calibration curve, given in Appendix 2, was used to determine the flow pitch angle, total and static pressures. Figure 4.2 is a photograph of the probes used in the mainstream.

The pressures sensed at the ports of the pitot-static, Kiel and three-dimensional probes were converted to voltages with a Setra Systems (Model number 237) pressure transducer. The transducer, shown in the photograph in Figure 4.3,was a bi-directional differential type with a range of $\pm$ 352 mm water (0.5 lb_f/in^2). The manufacturers' specifications for this unit are given in Appendix 2. The transducer was calibrated against a Betz manometer which could be read accurately to 0.1 mm of water. The calibration curve is shown in Figure 4.4. The voltage output from the transducer was displayed on a two channel

CAPTIONS FOR FIGURE 4.2

A United Sensor Three-Dimensional Probe

B United Sensor Kiel Probe

C Wedge Probe

D United Sensor Pitot-Static Probe

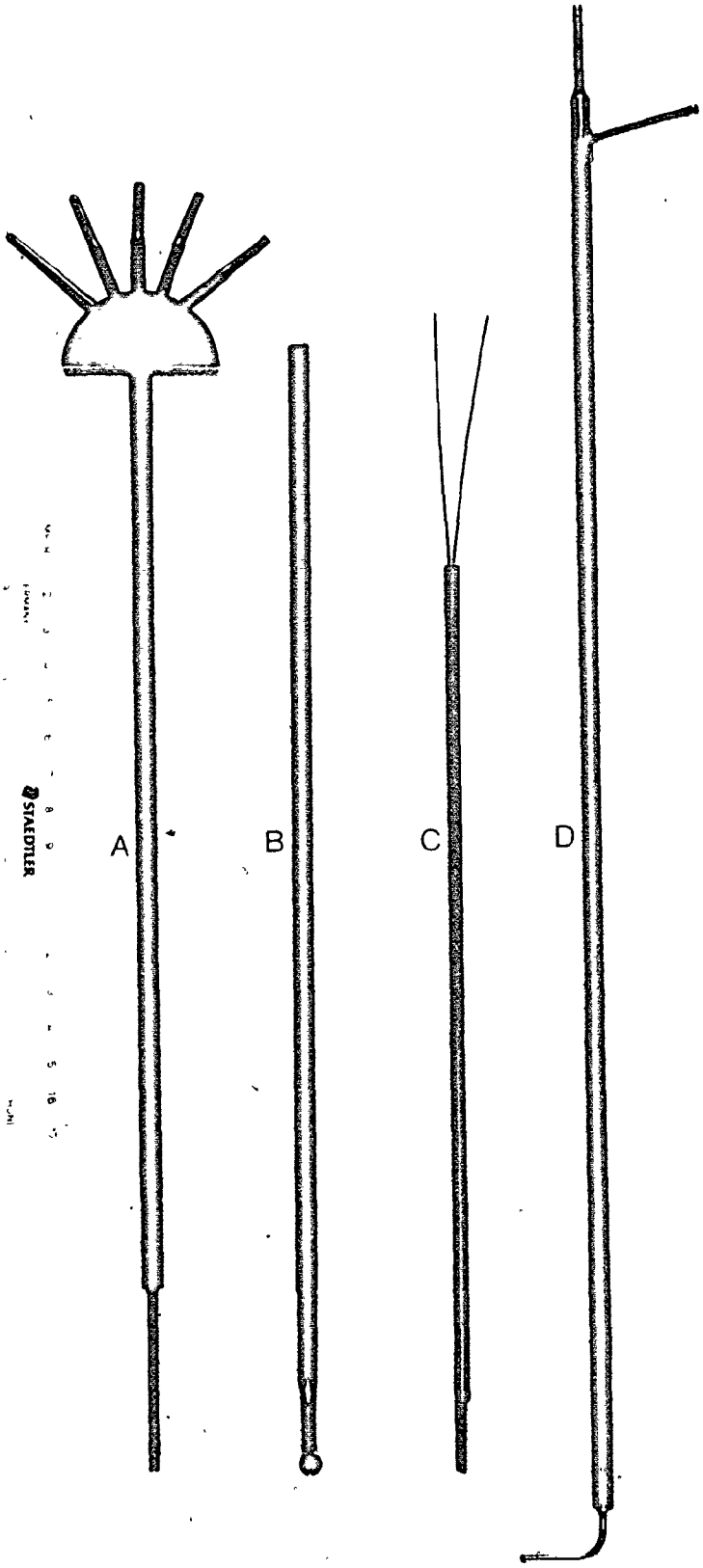

Figure 4.2 Probes Used for Mainstream Measurements.

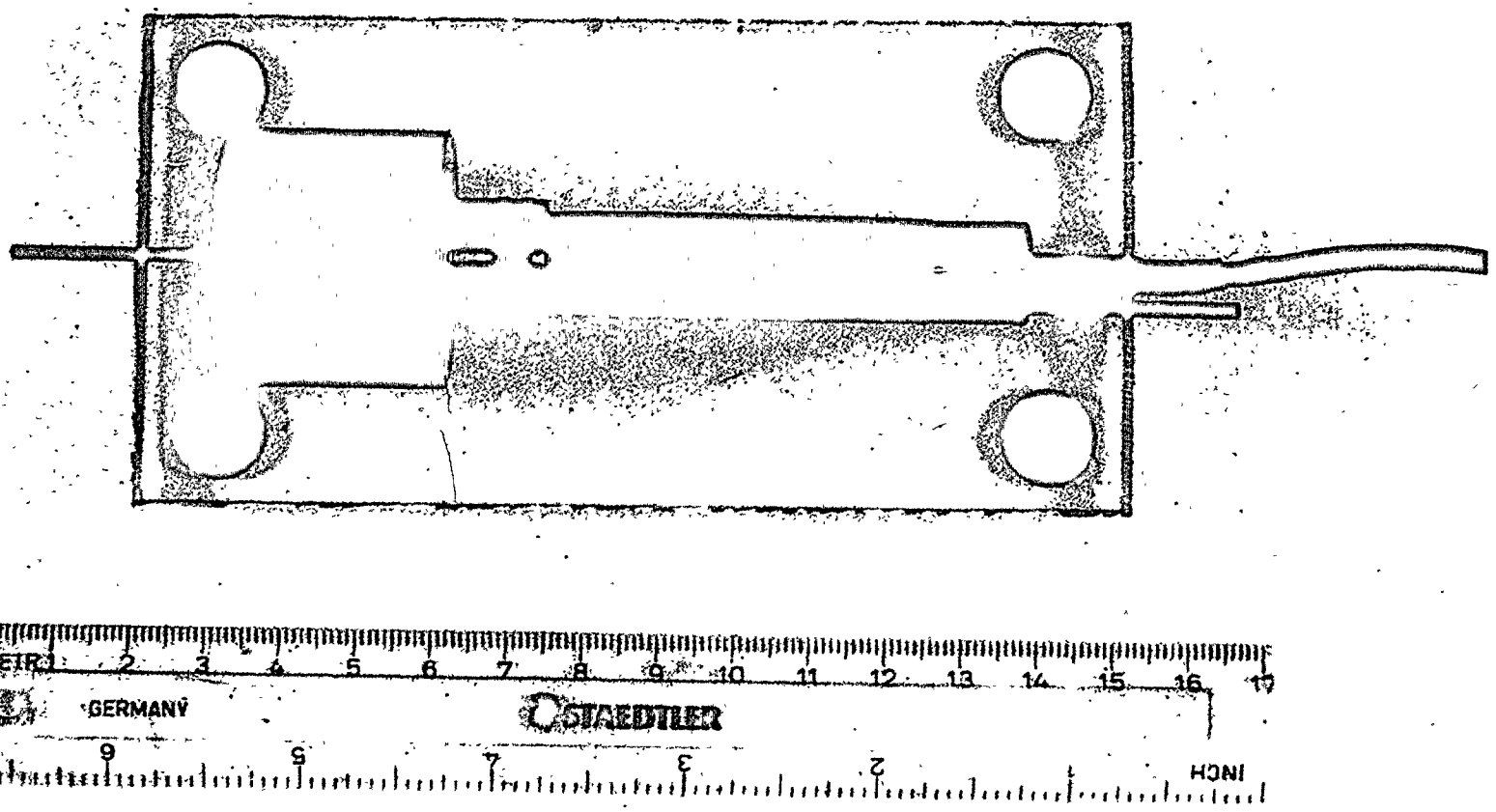

Figure 4.3 The Pressure Transducer.

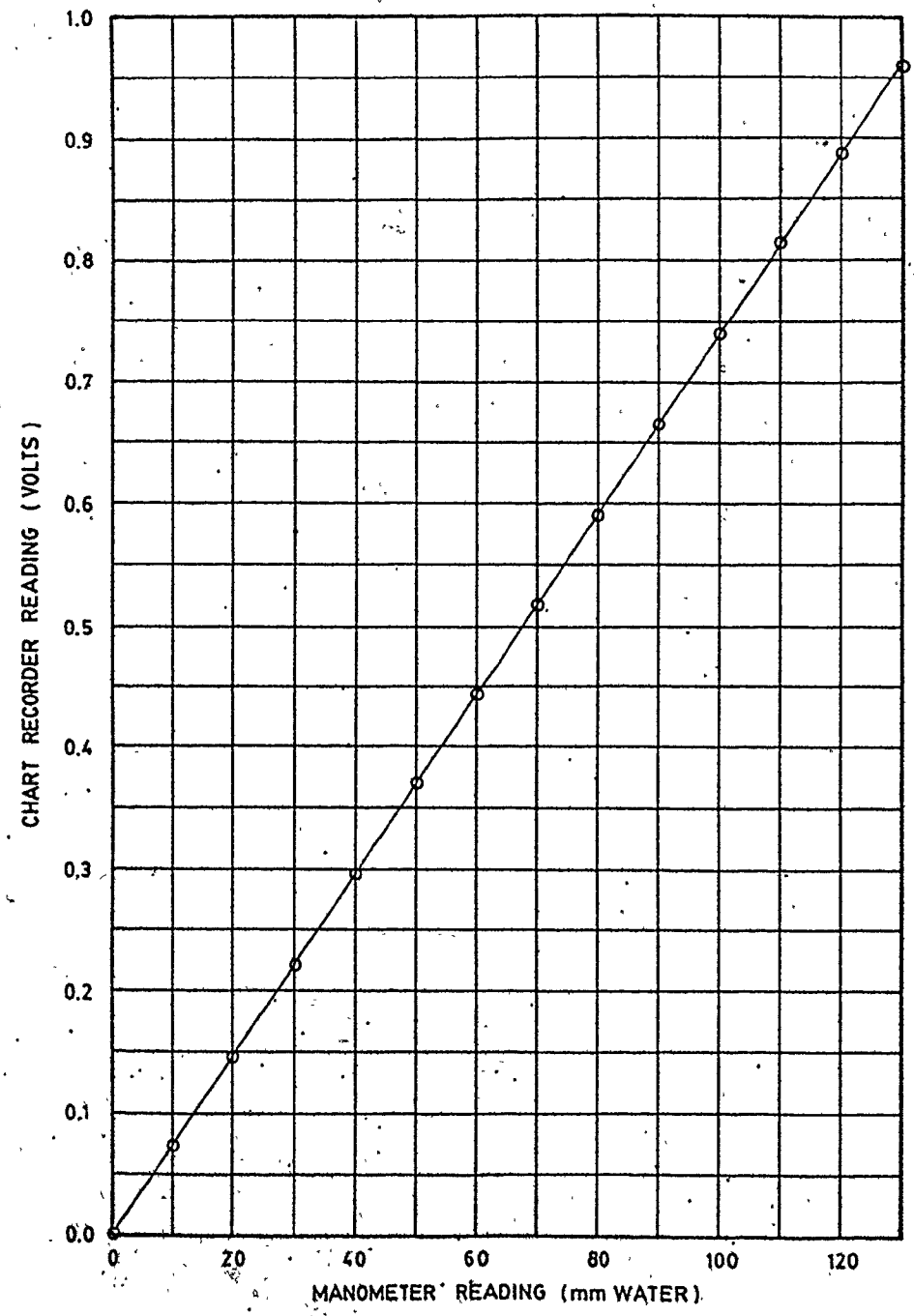

Figure 4.4 Transducer Calibration Curve.

Rikadenki chart recorder model B-281L. The apparatus for the transducer calibration is shown in the photograph of Figure 4.5.

The probes were connected to the transducer by 3.175 mm (0.125 inch) flexible clear Tygon tubing. A special T-valve system was assembled to convey the appropriate pressure to the transducer when the three-dimensional probe was used.

4.2 Inlet Channel Boundary Layer Instrumentation

Boundary layer measurements at the inner and outer endwalls were taken with the two specially constructed pitot-probes shown schematically in Figures 4.6 and 4.7. The probes were made from stainless steel tubing and their shape was designed to minimize possible stem effects. The probe tips were heated and flattened around a stainless steel shim which made it possible to take measurements within the vicinity of the wall. The inner dimensions were then measured with a toolmaker's microscope. The boundary layers were measured in the plane of the inlet measuring station and the same static taps, which were used in the mainflow measurements, were used to record the static pressure. The pitot and static pressures were connected to the transducer and the voltage output was displayed on the chart recorder. The transducer and chart recorder were also used to measure the static pressure within the boundary layer suction chambers (Chapter 6).

CAPTIONS FOR FIGURE 4.5

A Nitrogen Bottle

B Betz Manometer

C Keithley 179 TRMS Digital Multimeter

D Setra Pressure Transducer

E Whitey Micro Valve 22RS4

F Rikadenki Chart Recorder

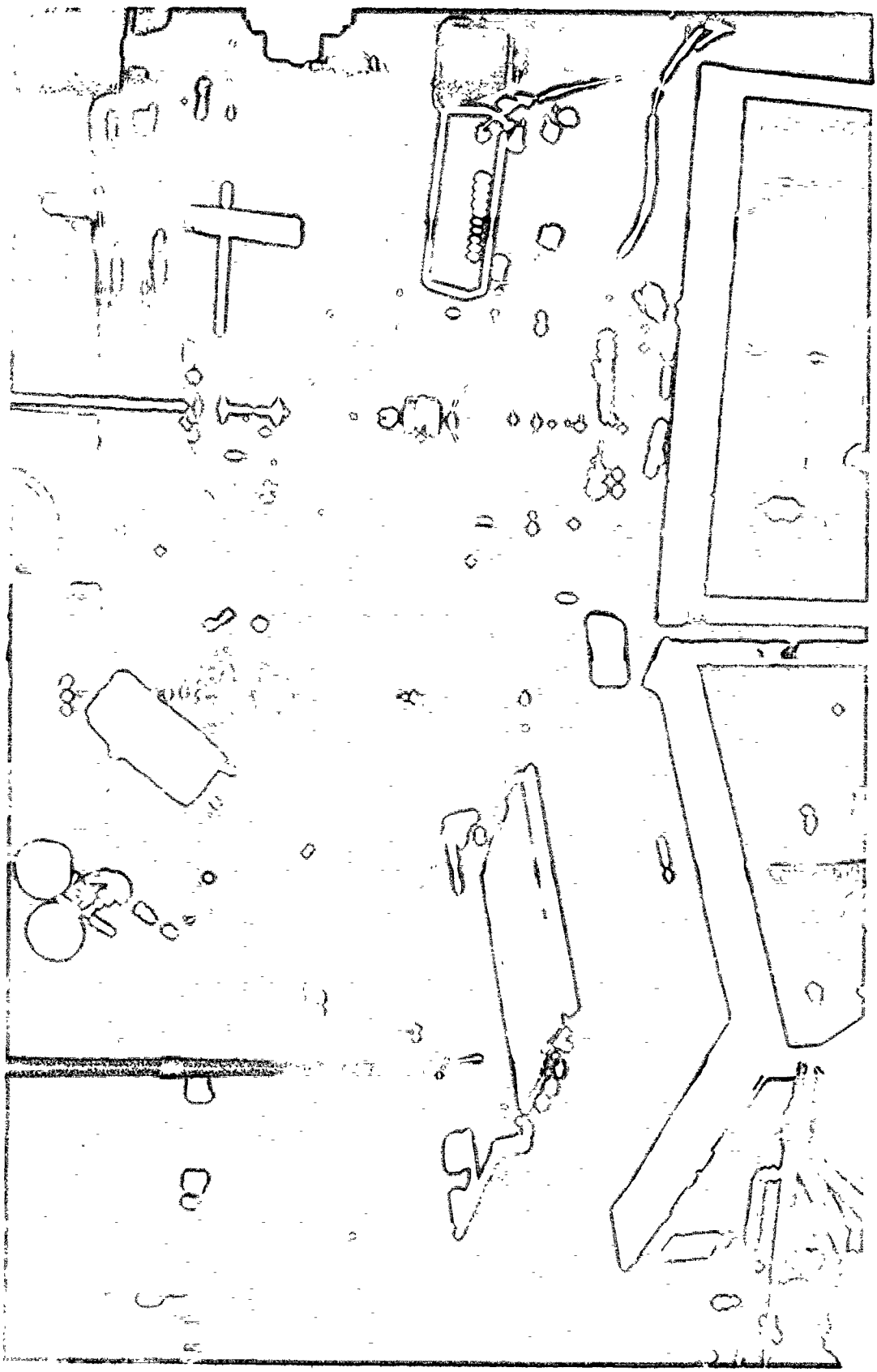

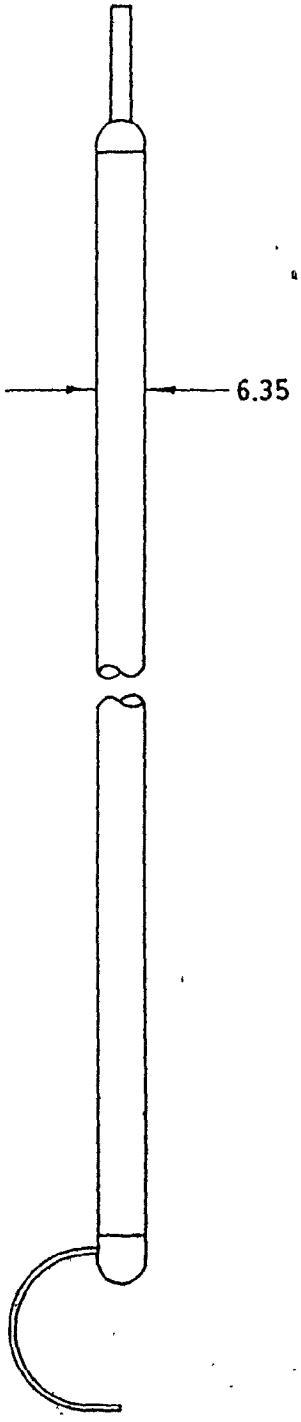

(DIMENSIONS IN mm)

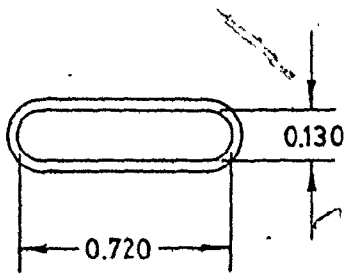

Figure 4.6 Inner Endwall Boundary Layer Probe.

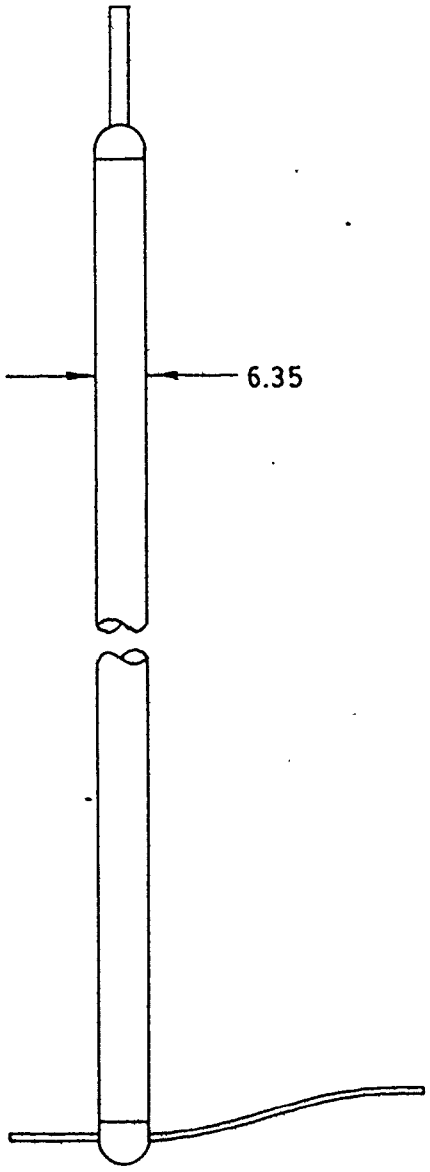

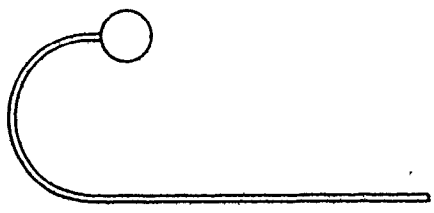

(DIMENSIONS IN mm)

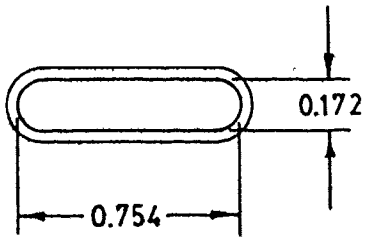

Figure 4.7 Outer Endwall Boundary Layer Probe.

4.3 Blade Test Passage Instrumentation

The cascade test passage (passage II Figure 4.1) was instrumented with a total of 130 -- 1 mm diameter static pressure taps. The axial location of these taps is shown by line numbers 1 to 7 in Figure 4.8.

4.3.1 The Endwall and Blade Surface Static Pressure Taps

The pitchwise and axial locations of the static pressure taps on the cascade endwalls are shown in Figure 4.9. Short pieces of 3.175 mm (0.125 inch) stainless steel tubing were epoxied into the exterior surface of the cascade endwalls (see Section C-C Figure 4.9).

The axial and spanwise locations of the static pressure taps on the blade pressure and suction surfaces are shown in Figures 4.10 and 4.11. The static taps on line numbers 1 to 5 were connected to short pieces of stainless steel tubing through 3.175 mm (0.125 inch) diameter holes drilled into the blades in the spanwise direction (see Figure 4.10 Section A-A). At the axial location designated by line 6, thin hypodermic tubing was used to make the connection to the surface static taps (see Section B-B Figure 4.11). These tubes were epoxied into machined rectangular channels and the surface was hand-sanded to the original profile. An overall view of the test passage and the related static pressure instrumentation is shown in Figure 4.12.

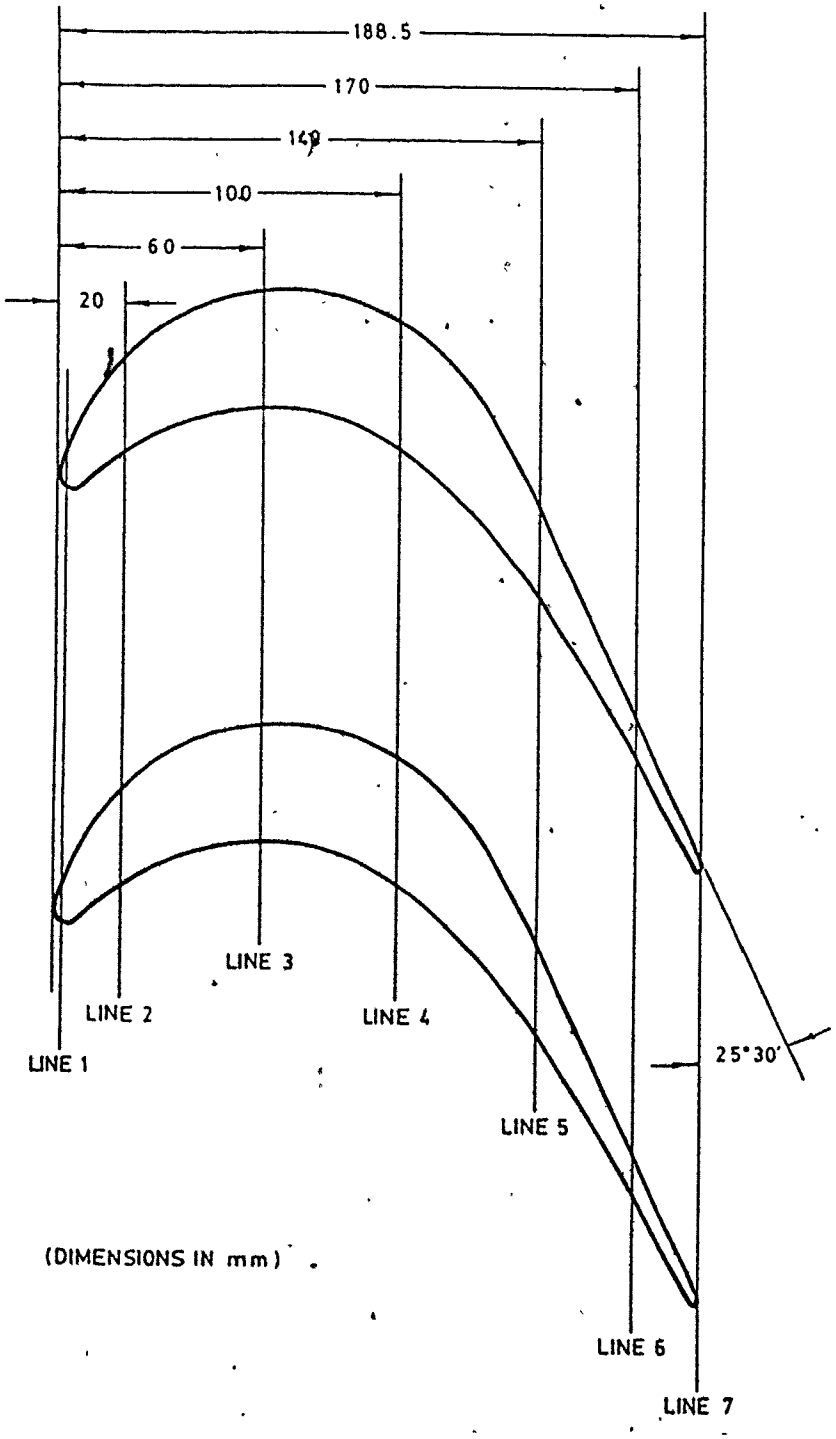

Figure 4.8 Axial Locations of the Static Pressure Taps in the Cascade Test Passage.

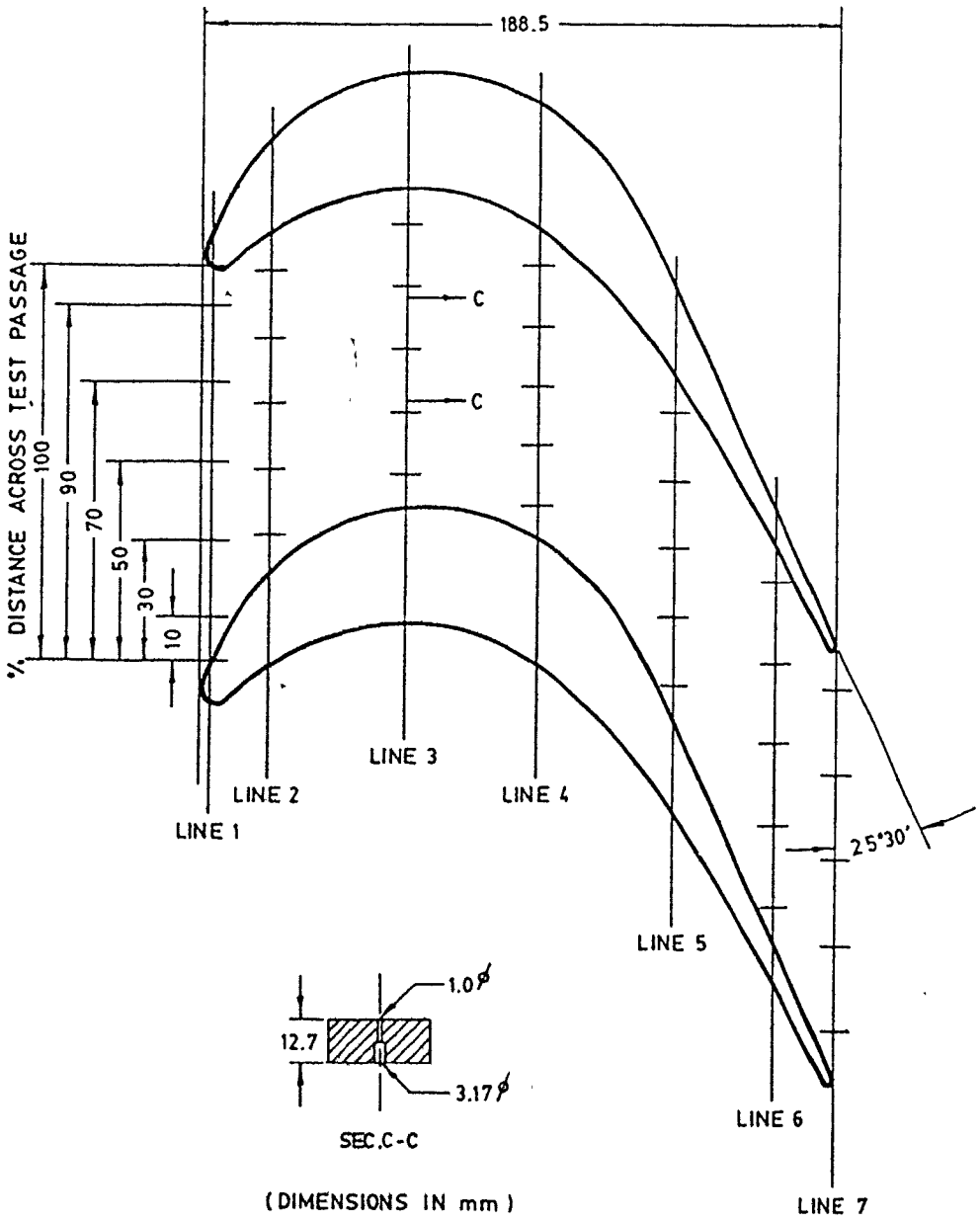

Figure 4.9 Location of the Static Pressure Taps in the Cascade Endwalls.

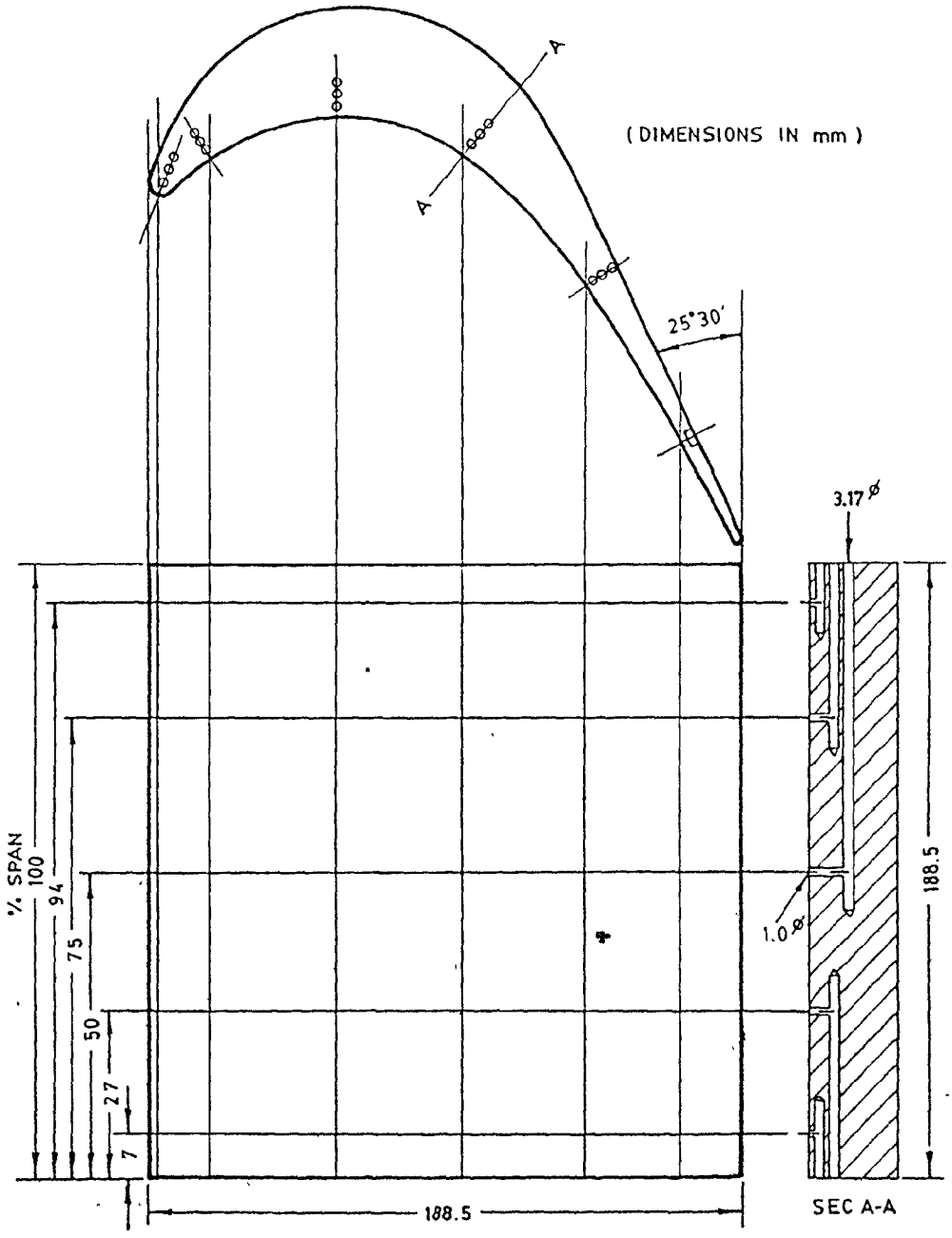

Figure 4.10 Location of the Static Pressure Taps on the Blade Pressure Surface.

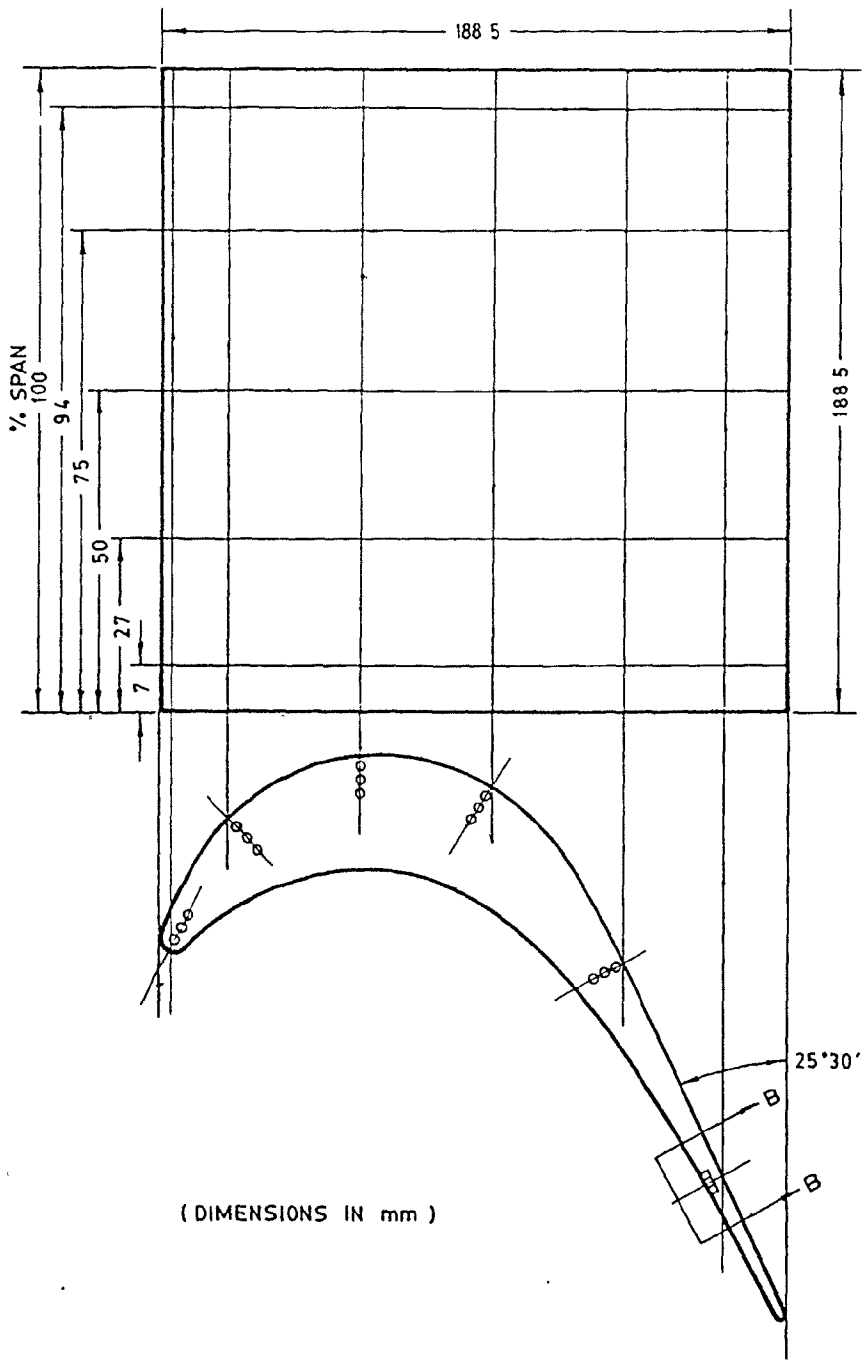

Figure 4.11 Location of the Static Pressure Taps on the Blade Suction Surface.

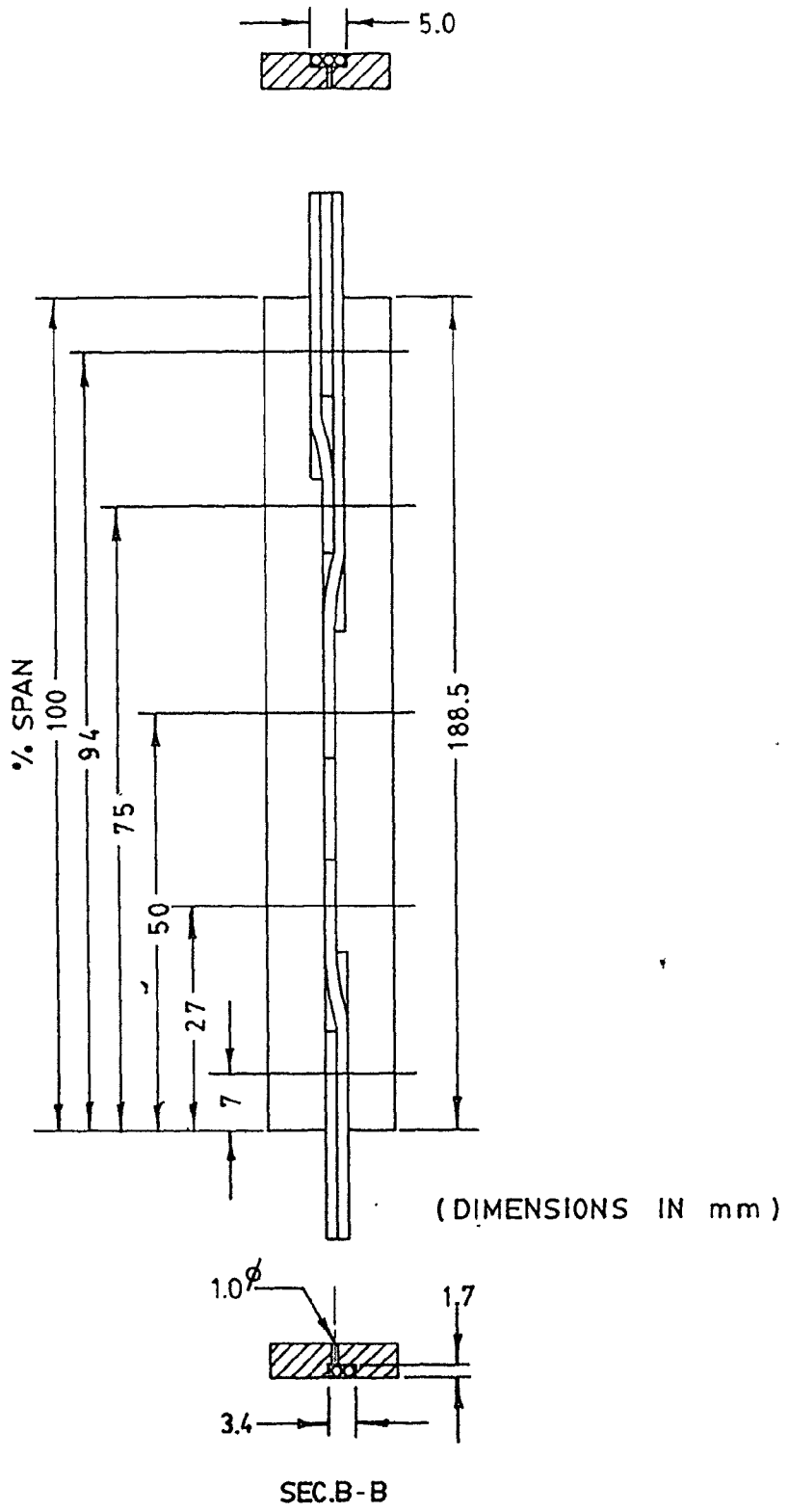

Figure 4.11 (Continued).

Inst.

The test passage static pressures were recorded on a water-filled multitube manometer (shown in the photograph of Figure 3.7) manufactured by T.E.M. Instruments (Model 10397). Its capacity was limited to 36 tubes but 130 static pressure readings were required. It was therefore, necessary to construct a switching station which would allow the measurements to be taken in four stages. Thirty readings were taken on each blade surface and thirty-five readings were taken on each cascade endwall. The switching station was made up of a silicone coated perforated rubber sheet sandwiched between two acrylic plates. Connections to the bank of manometers and to the test rig were made via short pieces of 3.175 mm (0.125 inch) stainless steel tubing. The unit was mounted on the plenum chamber and is shown in the photograph of Figure 3.7.

CHAPTER 5

OBJECTIVES AND EXPERIMENTAL PROCEDURES

This chapter outlines the series of tests which were conducted on the two-dimensional cascade rig. Since the test rig was a new construction, it was necessary to perform a series of preliminary tests in order to assess the flow within the inlet channel. The entire testing program can be categorized as follows:

5.1 Preliminary Tests

The two-dimensional Laplace equation was solved for the cascade configuration using the electrical analogue. The purpose was to determine the appropriate lengths of the inlet and exit channels and to provide a comparison between the theoretical and measured incidence angles at the inlet measuring station. The by-pass at the fan inlet was adjusted to eliminate vibrations. Flow measurements were taken at the throat of the inlet bellmouth duct. The mainstream flow was traversed in the spanwise and pitchwise directions at the inlet measuring station. The inlet flow periodicity was observed and adjusted with sidewall suction. The inner and outer endwall boundary layer displacement thickness was varied with the aid of the suction chambers. The boundary

layer probe was traversed in the pitchwise direction (within the boundary layer) to ensure that the suction effect was uniform. Under maximum suction conditions at both endwalls, the mainstream flow was traversed in the spanwise direction to ensure that it was unaffected by the reduction of the boundary layer. Measurements to calculate turbulence intensity were taken at the inlet measuring station. A detailed description of these tests and their results is given in Chapter 6.

5.2 Test Passage Measurements

Static pressure measurements were taken on the test passage surfaces (passage II Figure 4.1). The surface pressure distributions are shown and discussed in Chapter 7.

5.3 Tests at the Exit Measuring Stations

Pitchwise and spanwise traverses were conducted at exit measuring station A (Figure 4.1) for five distinct boundary layer displacement thicknesses. The exit plane measurements, corresponding to each inlet boundary layer displacement thickness, were used to plot contour maps of the local total pressure loss coefficient and the static pressure coefficient. These same measurements were used to show the spanwise variation in the pitchwise averaged values of the total pressure loss coefficient, the dimensionless axial flow velocity and the deviation. The total pressure loss

coefficient was calculated for each corresponding inlet boundary layer displacement thickness and the secondary loss coefficient was estimated and compared with some existing correlations. Measurements were taken at exit measuring station B (for one specific inlet condition) to show the effect of mixing on the calculated total pressure loss coefficient. These exit flow tests are explained and discussed in detail in Chapter 8.

CHAPTER 6

EXAMINATION OF THE INLET CHANNEL FLOW PARAMETERS

In cascade testing, the experimentor must have a good description of the inlet flow conditions before any confidence can be placed on downstream experimental measurements. This chapter presents the results of several flow measurements which were taken within the inlet channel to study the overall operating characteristics of this portion of the cascade test rig. These flow measurements were taken within the mainstream and within the endwall boundary layers at a Reynolds number of 3.68×10^5 based on the blade chord and on the average inlet velocity VI of 26.5 m/s (87 ft/s).

6.1 Flow Characteristics at the Bellmouth Throat

The flow at the bellmouth throat was traversed both in the spanwise and throat width directions with a pitot-static probe. Figure 6.1 shows the spanwise distribution of velocity plotted at representative throat width locations. The profiles are nearly identical, being flat and fully developed at a distance of approximately 4% of the blade span.

6.2 Pitchwise Distribution of Velocity and Incidence at the Inlet Measuring Station

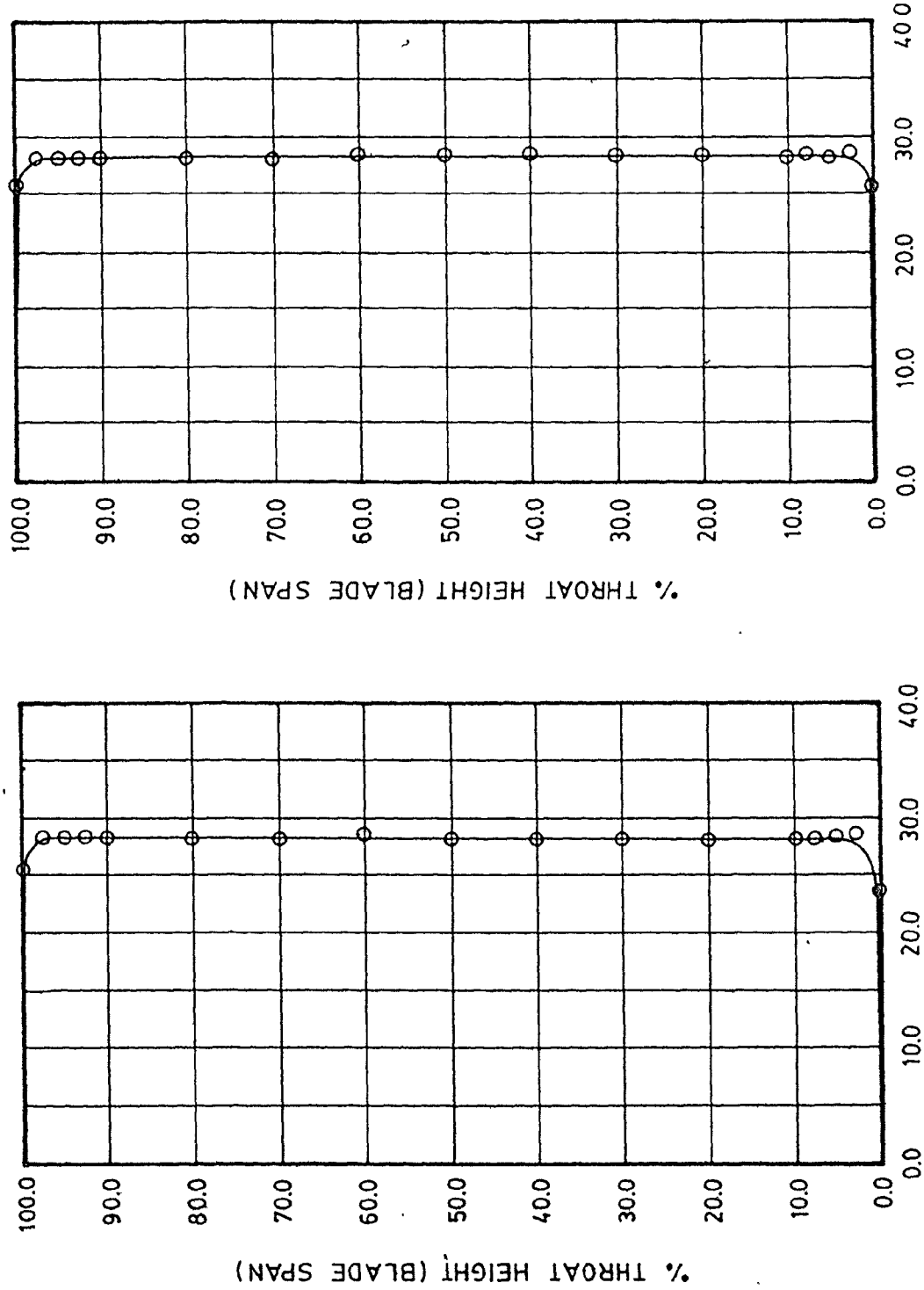

Figure 6.1 Velocity Distribution at the Bellmouth Throat at Various Throat Width Locations.

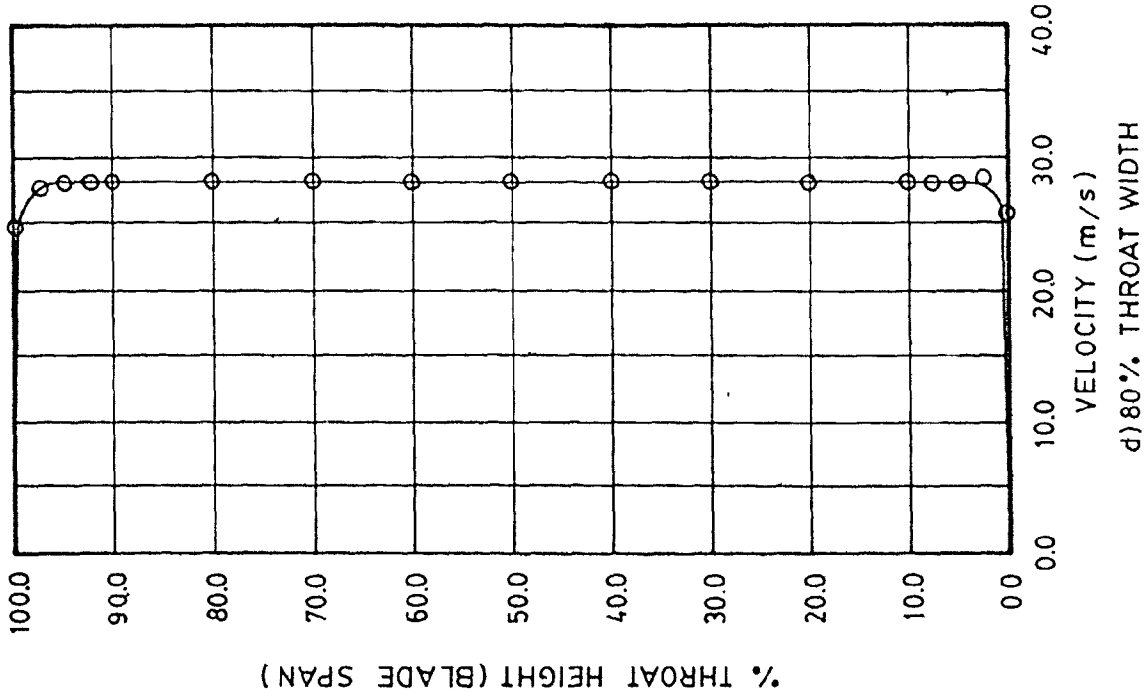

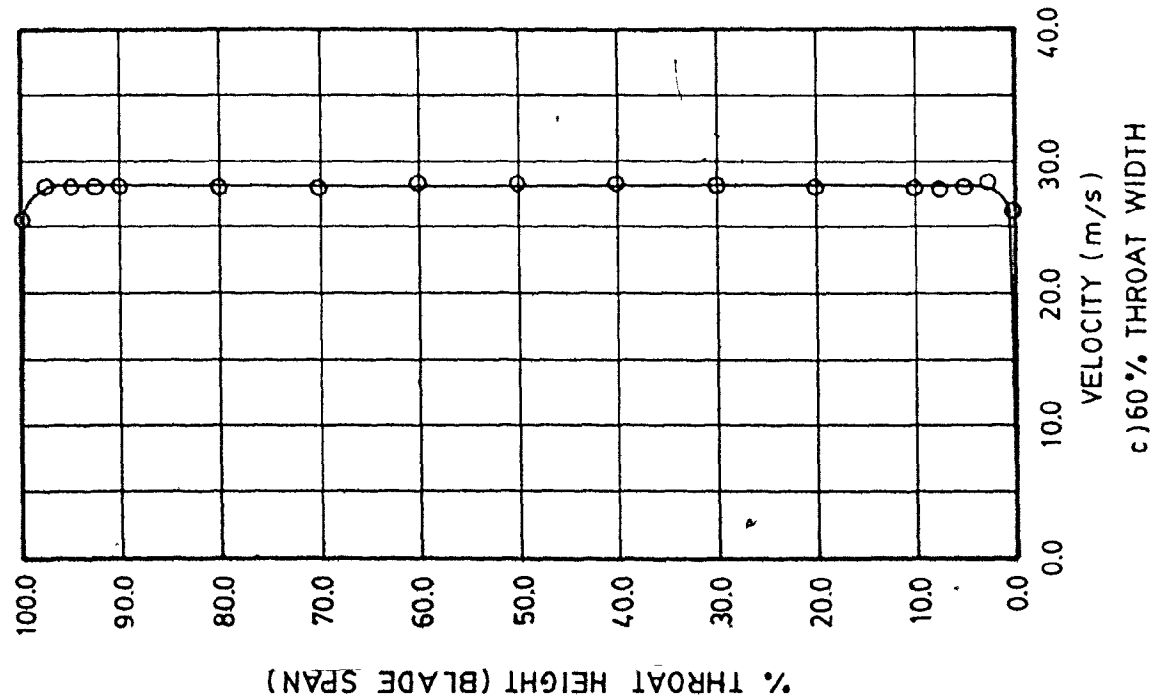

Figure 6.1 (Continued).

The mainstream was traversed in the pitchwise direction at three spanwise locations corresponding to blade heights of 20%, 50% and 80%. The measurements were taken with the wedge probe and the Kiel probe at 20 mm increments in the pitchwise direction and covered a distance of 2 S. The final velocity and incidence distributions for blade spans at 20%, 50% and 80% are shown in Figures 6.2, 6.3, and 6.4 respectively. The velocity has been expressed non-dimensionally as the ratio of the local values to the mean velocity VI (26.5 m/s (87 ft/s)) across the test passage at 50% blade span. The velocities were calculated using the pressure measurements obtained with the Kiel probe. The figures show that there is virtually no pitchwise or spanwise variation in the calculated velocities. Several preliminary tests had to be conducted with various combinations of mainstream and sidewall suction chamber mass flow rates. It was necessary to reduce the mainstream mass flow rate and increase the sidewall suction chamber mass flow rate to its maximum in order to produce the incidence distributions depicted in Figures 6.2, 6.3 and 6.4. The incidence variation (due to the upstream effect of the cascade blade leading edges) shows that reasonable periodicity was established. For the purpose of this study, the periodicity was defined as the cyclic variation of the flow incidence as a function of blade pitch. The periodicity was best established at 20% blade span and to a lesser extent at the 50% and 80%

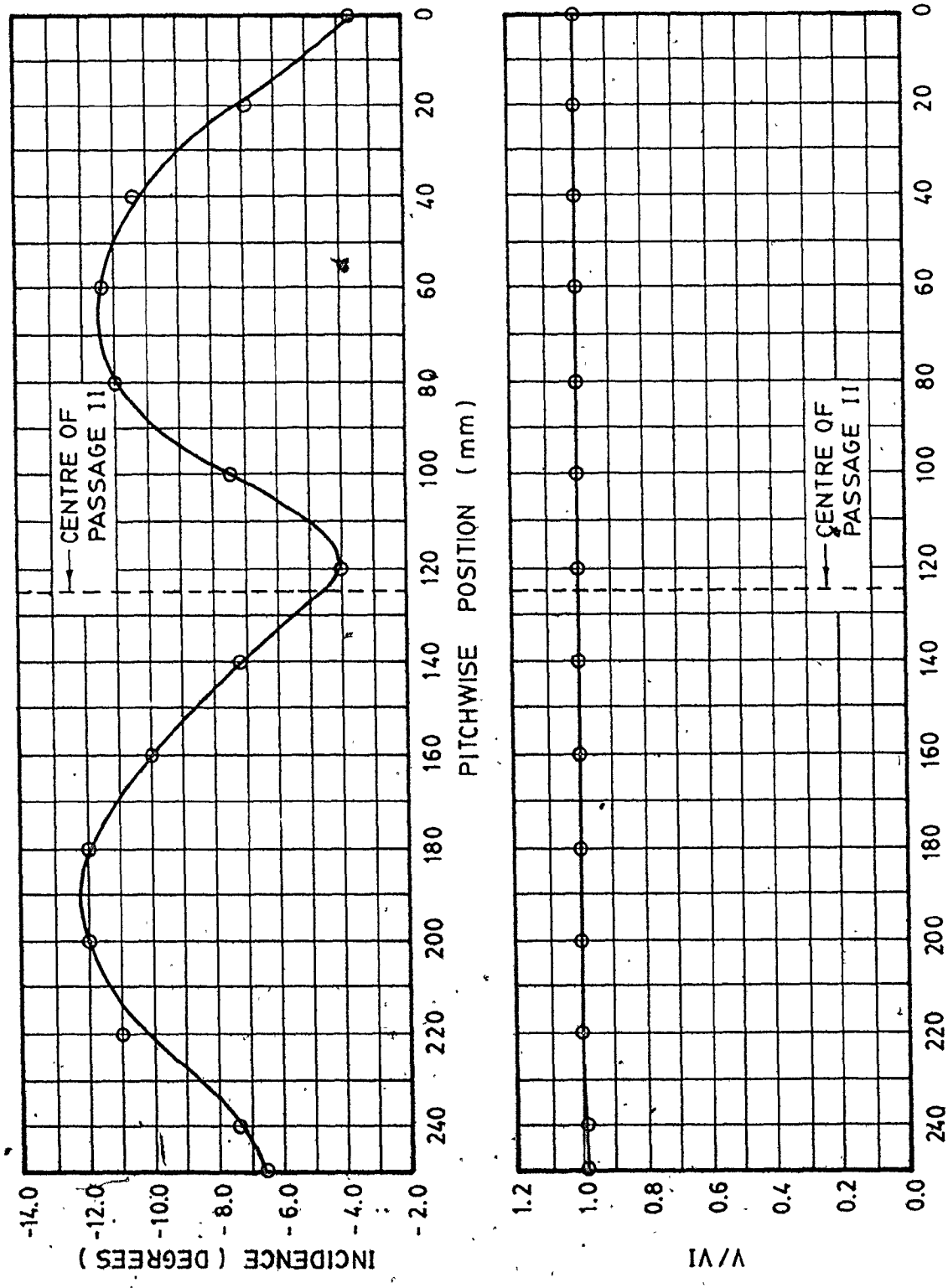

Figure 6.2 Pitchwise Distribution of Velocity and Incidence at the Inlet Measuring Station at 20% Blade Span.

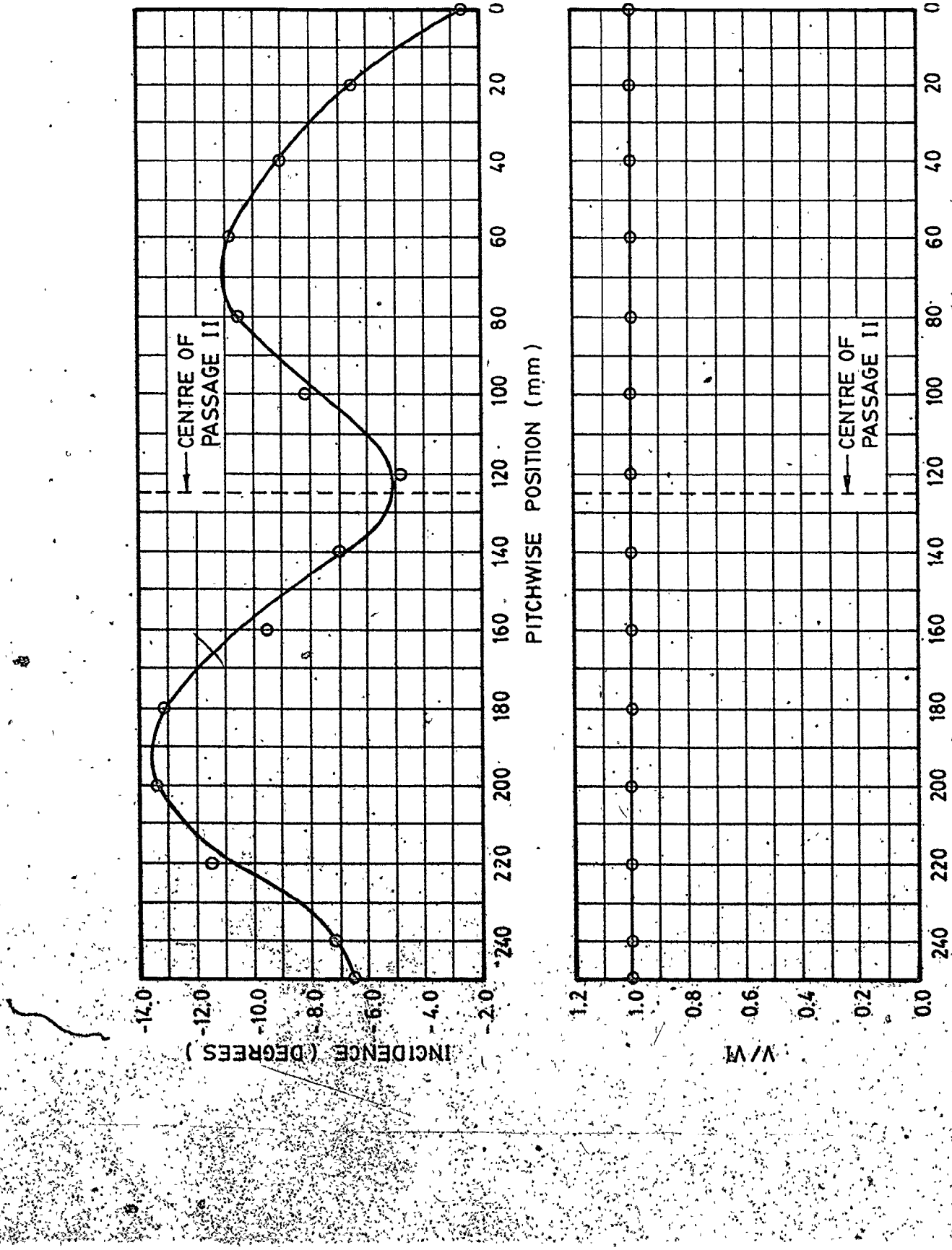

Figure 6.3 Pitchwise Distribution of Velocity and Incidence at the Inlet Measuring Station at 50% Blade Span.

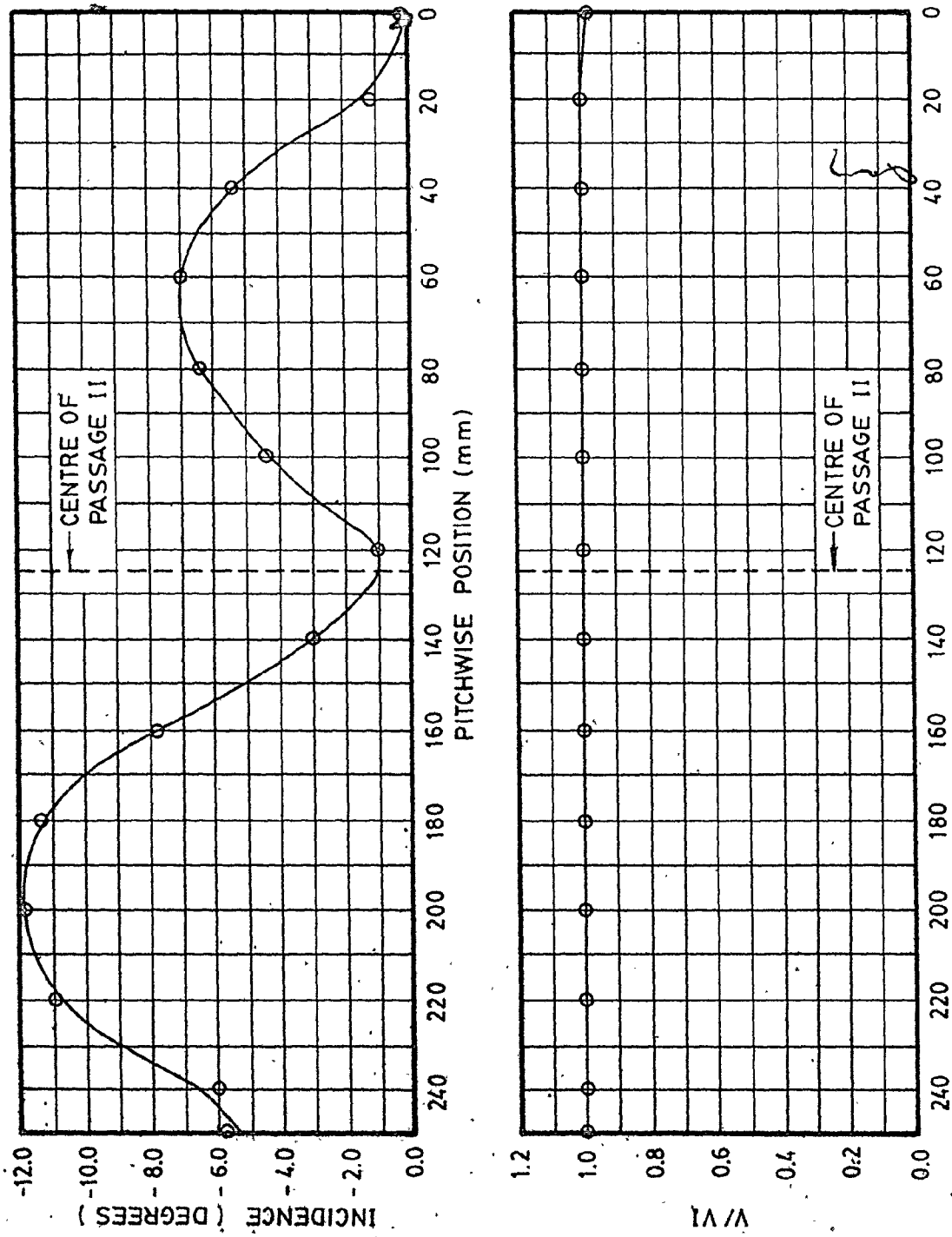

Figure 6.4 Pitchwise Distribution of Velocity and Incidence at the Inlet Measuring Station at 80% Blade Span.

blade span locations.

Figure 6.5 shows the results of the electrical analogue potential flow solution and the associated apparatus is shown in the photograph of Figure 6.6. The equipotentials on the special carbon impregnated paper were traced onto a mylar sheet and the streamlines were faired in to form curvilinear squares. The theoretical incidence angles were measured from this orthogonal plot at a position corresponding to the inlet measuring station (27.5 mm ahead of the blade leading edges) and are shown in Figure 6.7. The incidence depicted in Figure 6.7, when compared to the incidence in Figures 6.2, 6.3 and 6.4,is more negative overall and the periodicity is shifted by approximated 20 mm in the direction of the sidewall suction chamber. The differences described could be attributed to an inaccurate proportioning of the current at sinks 1 and 2 (Figure 6.5) in the electrical model.

6.3 Spanwise Distribution of Velocity and Incidence at the Inlet Measuring Station

The mainstream was also traversed in the spanwise direction at five pitchwise positions corresponding to the geometric projections of the centres of passages I, II and III (0 mm, 124.7 mm and 249.4 mm respectively) and to the geometric projections of the leading edges of blades 2 and 3 (62.3 mm, and 187 mm respectively) (Figure 4.1).

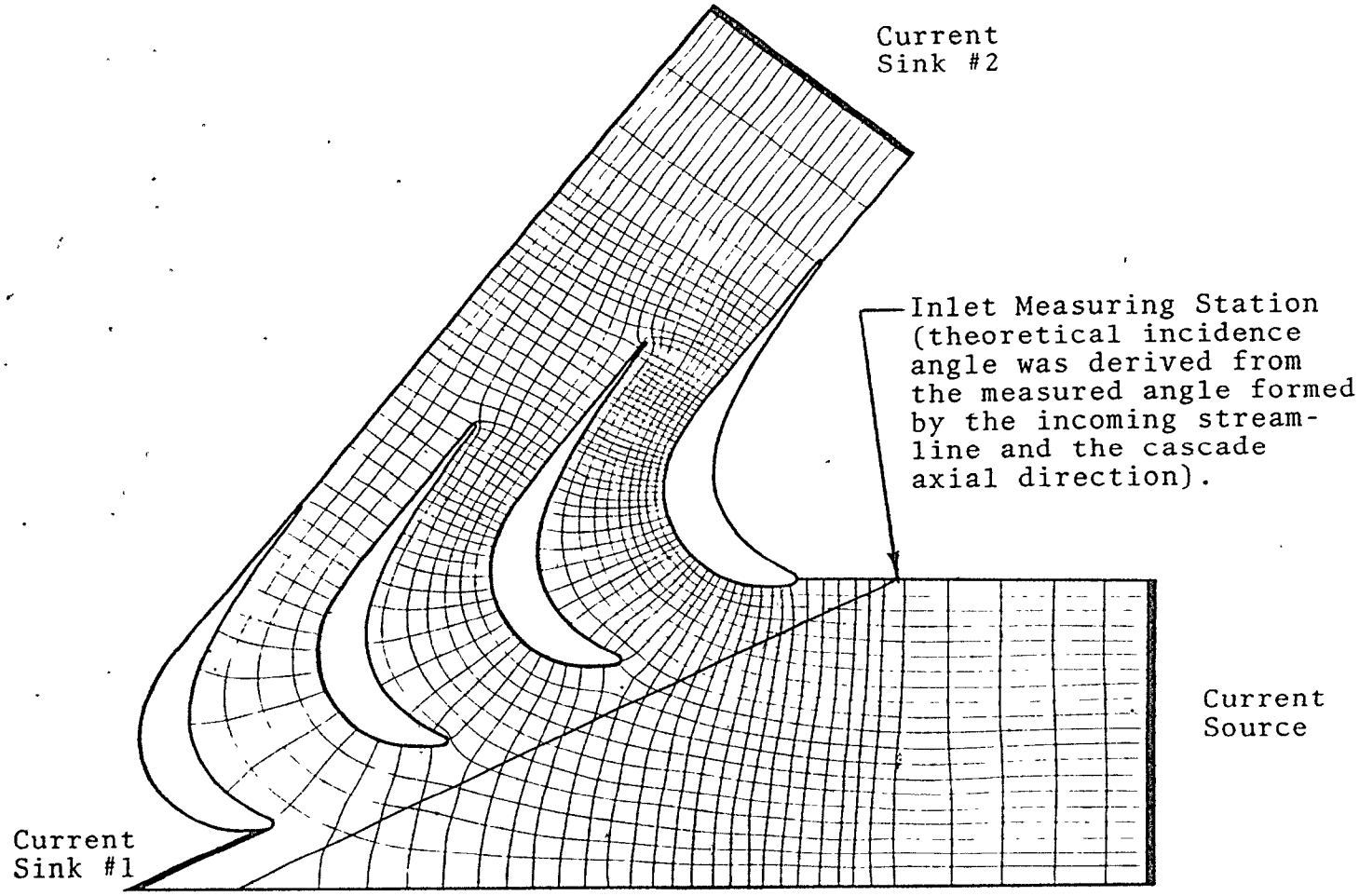

Figure 6.5 Cascade Equipotentials and Streamlines from the Electrical Analogue Potential Flow Solution.

CAPTIONS FOR FIGURE 6.6

A Kelk Field Plotter

B Stylus

C Keithley 179 TRMS Digital Multimeter

D Fluke 8000A Digital Multimeter

E Test Section Geometry

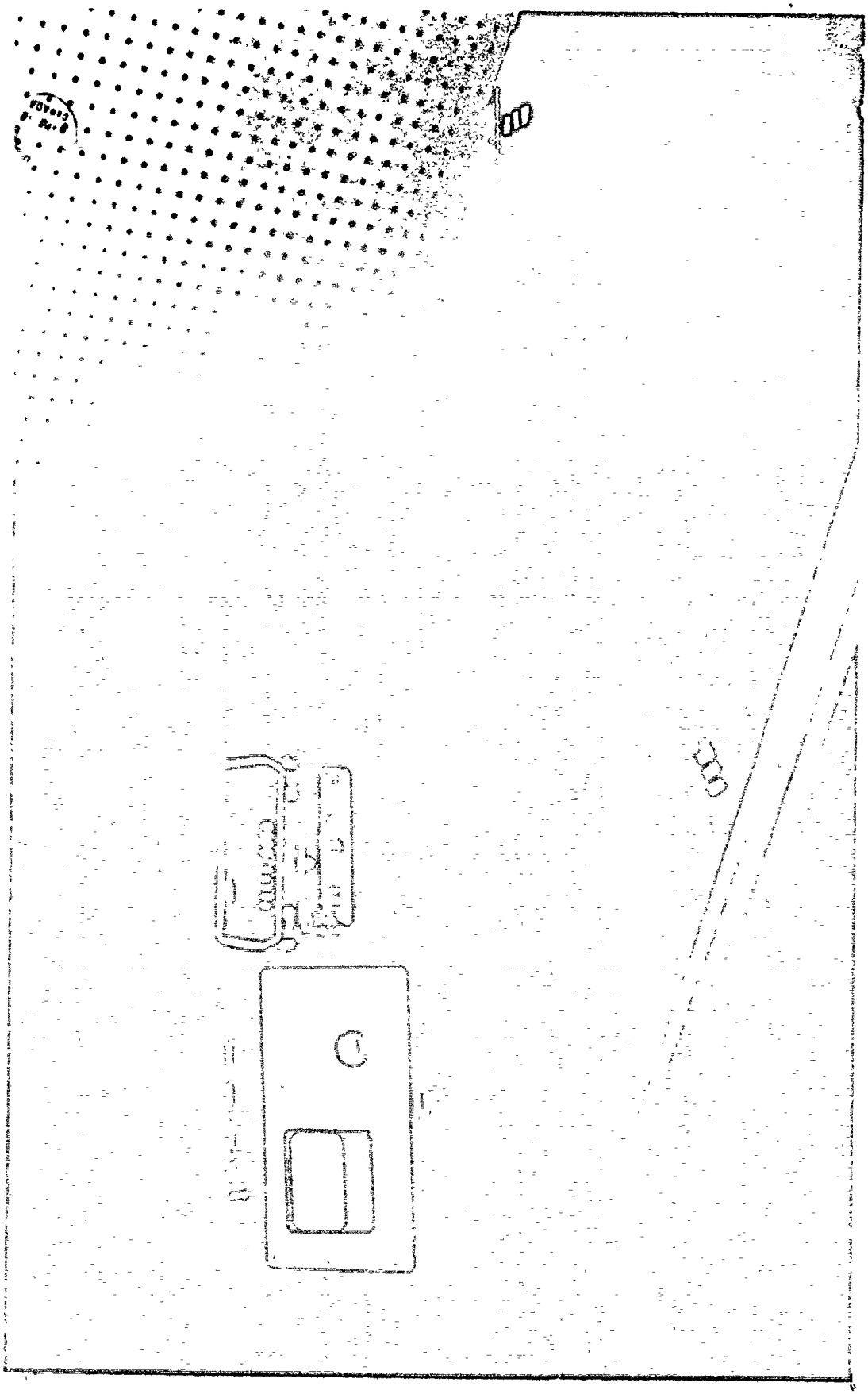

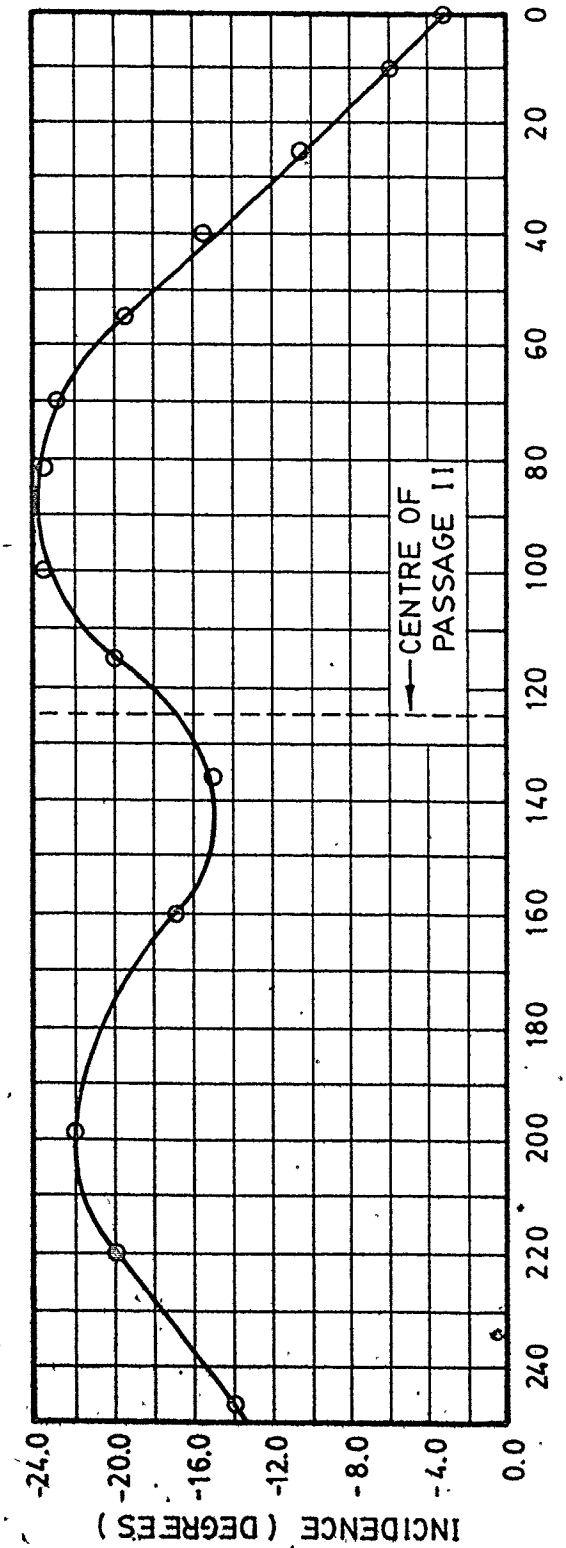

Figure 6.7 Pitchwise Distribution of Incidence from the Electrical Analogue Potential Flow Solution.

The flow measurements were taken with the Kiel and wedge probes in 10% increments from 10% to 90% of the blade span. The remaining portions of the traverses were completed with the use of the boundary layer probes described in Chapter 4 (a more detailed discussion of the boundary layer is provided in the next section of this chapter). The results of these traverses are shown in Figures 6.8 through 6.12. These Figures show that there is no spanwise variation in the calculated velocity within the mainstream (as expected from observation of Figures 6.2 through 6.4). The incidence change in the spanwise direction is generally within 6^{o}. This variation could be caused by non-uniform suction through the porous plate in the sidewall suction chamber.

It should be stated that preliminary measurements were taken with the five-hole probe which showed that the pitch angle was everywhere equal to zero at the cascade inlet measuring station (as is expected in a two-dimensional test facility of this type).

6.4 The Endwall Boundary Layer

The boundary layers were investigated with the specially designed probes described in Chapter 4. Since the mainstream velocity profile was well defined, it was decided to identify the edge of the boundary layer as the height at which the velocity reached 99.5% of the main-

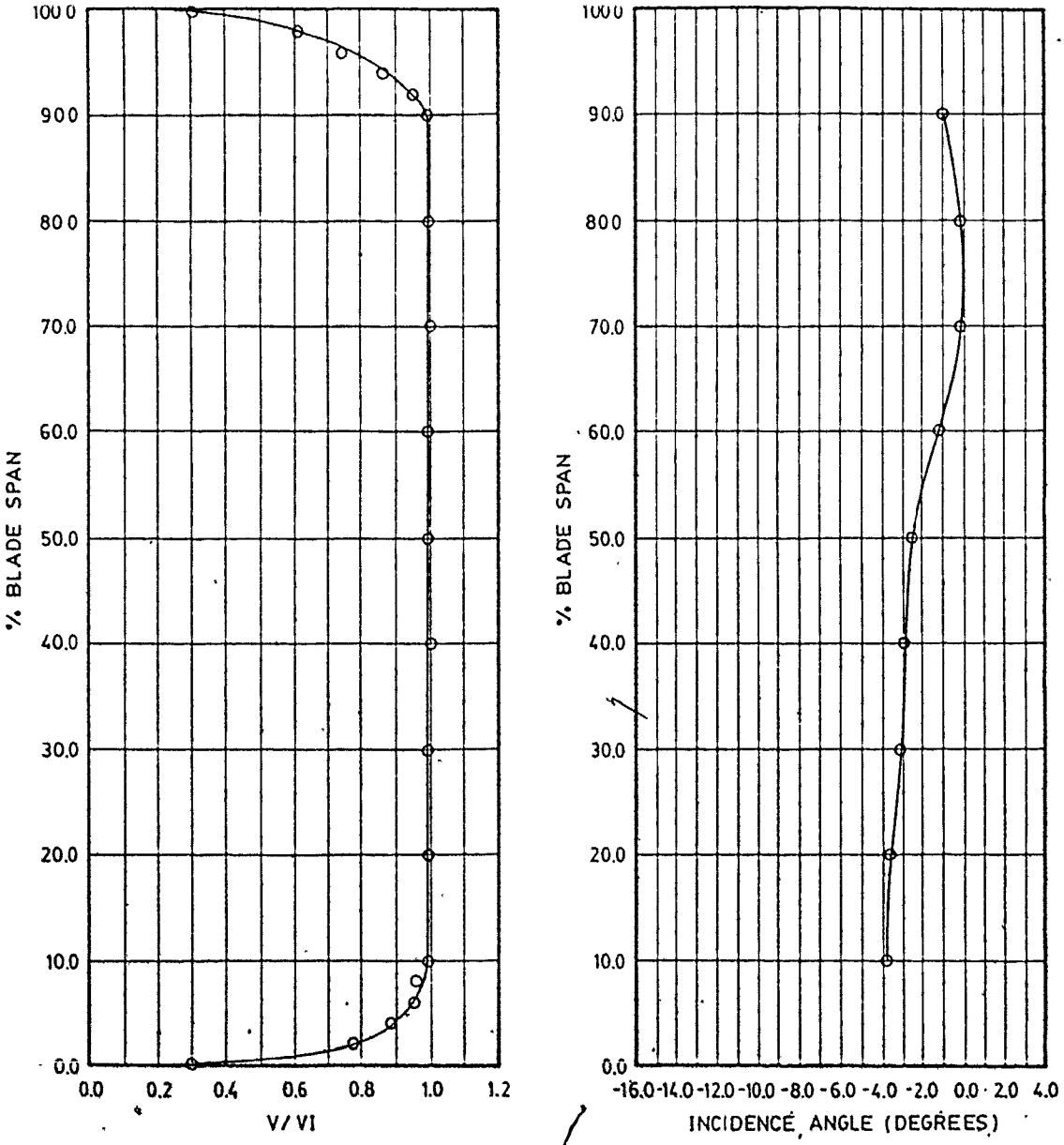

Figure 6.8 Spanwise Distribution of Velocity and Incidence at the Geometric Projection of the Centre of Passage I.

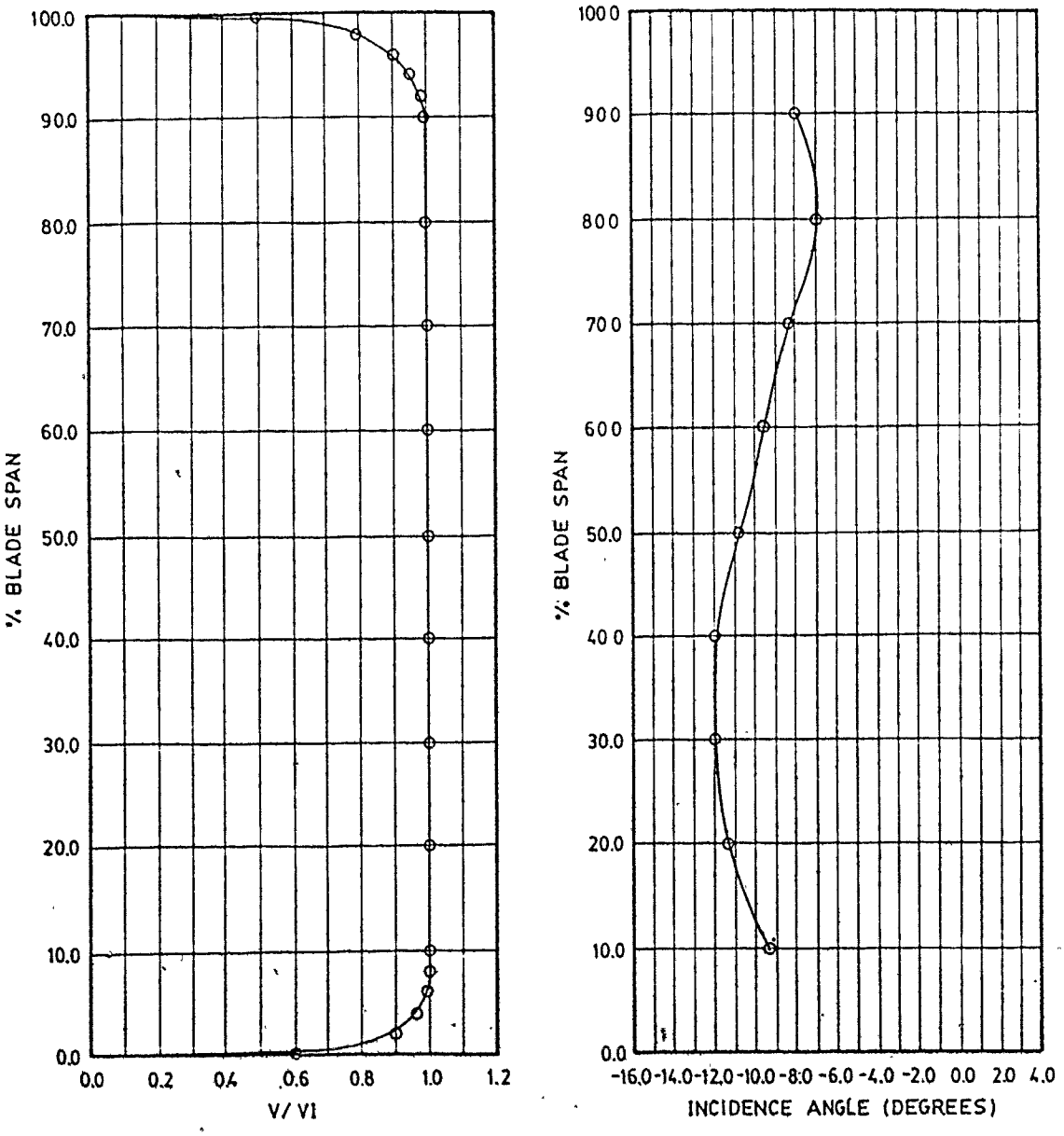

Figure 6.9 Spanwise Distribution of Velocity and Incidence at the Geometric Projection of the Leading Edge of Blade 2.

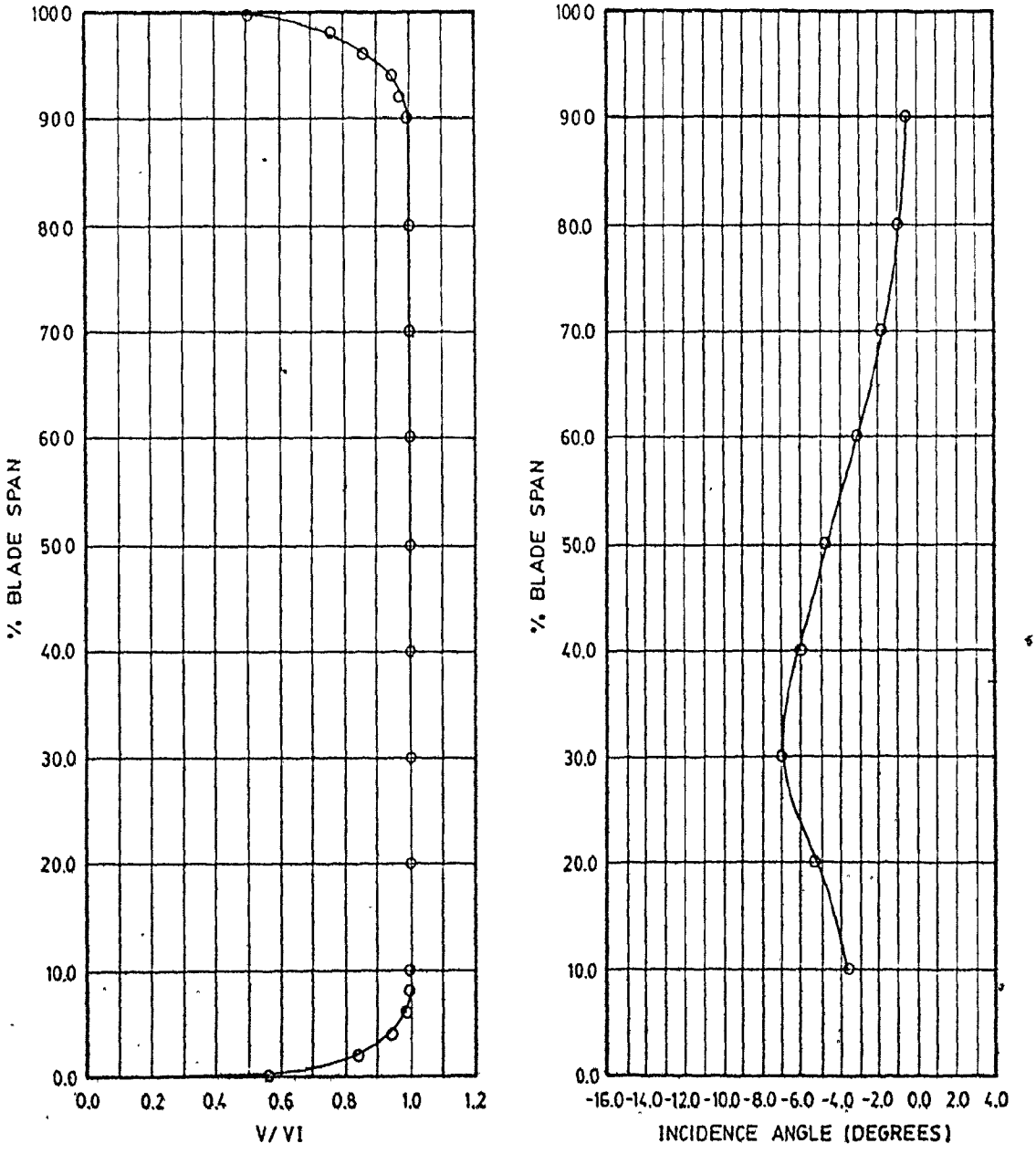

Figure 6.10 Spanwise Distribution of Velocity and Incidence at the Geometric Projection of the Centre of the Test Passage.

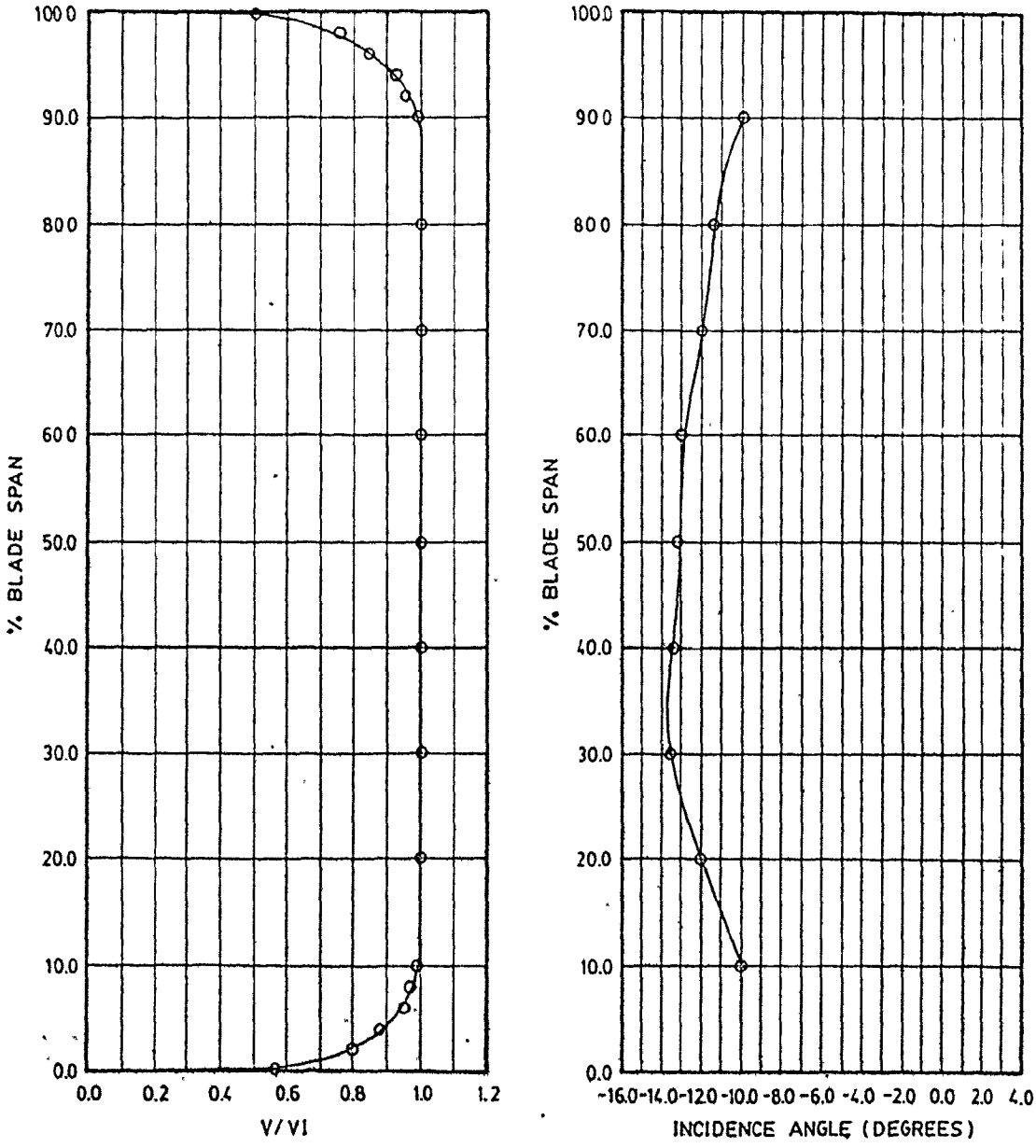

Figure 6.11 Spanwise Distribution of Velocity and Incidence at the Geometric Projection of the Leading Edge of Blade 3.

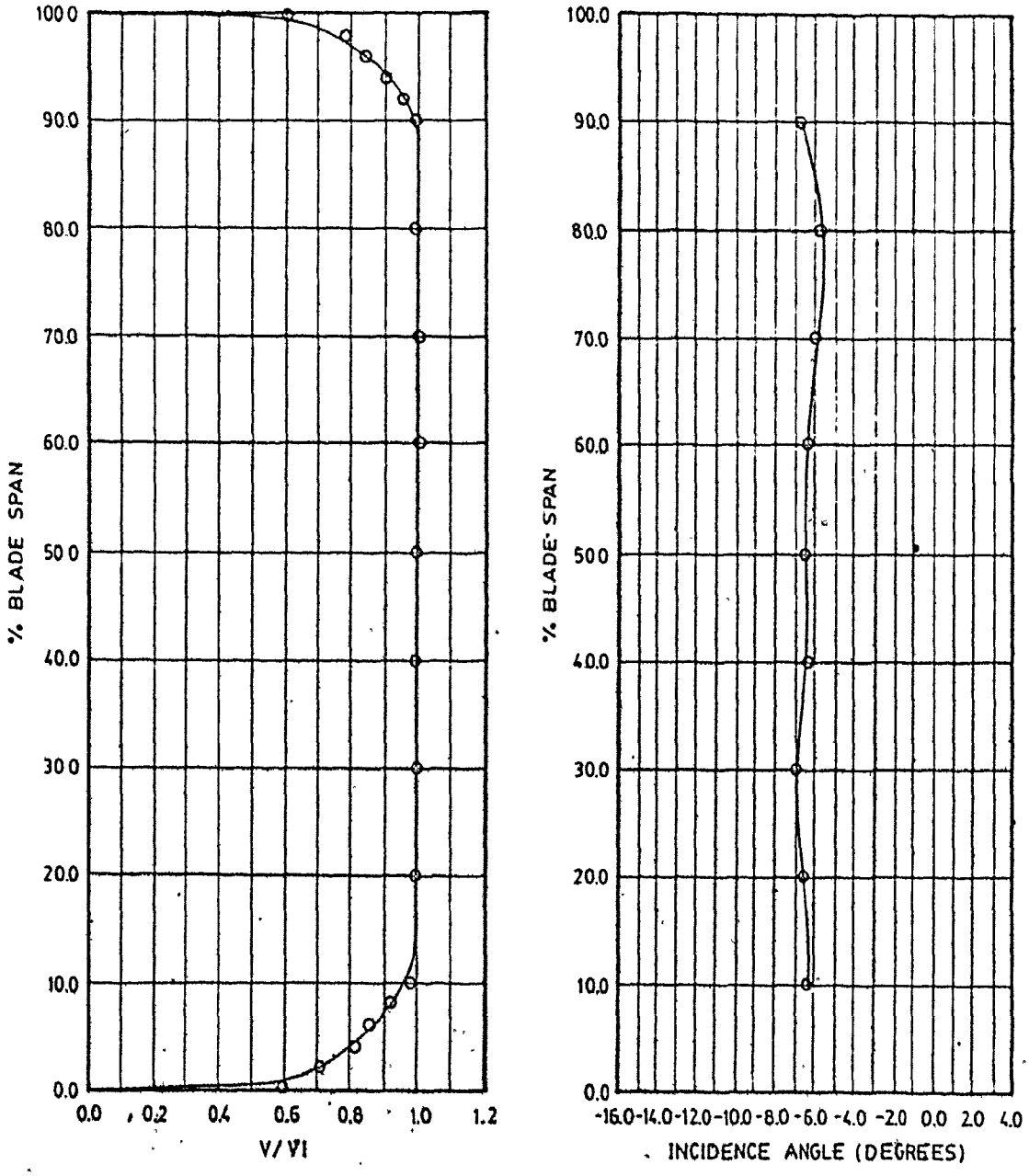

Figure 6.12 Spanwise Distribution of Velocity and Incidence at the Geometric Projection of the Centre of Passage III.

stream value. Measurements were taken at five pitchwise positions (measured from the origin shown in Figure 4.1) at both the inner and outer endwalls and the results are shown in Figure 6.13 a) through e). The profiles at the inner endwall were slightly more developed than those at the outer endwall and at locations a) through d) it was estimated that the boundary layer extended into the flow a distance equal to 10% of the blade span (18.9 mm). At location e) the profiles were fully developed at approximately 14% of the span (26.4 mm). The distributions were found to fit a 1/7th power law turbulent boundary layer profile.

6.5 Endwall Boundary Layer Control

The suction system described in Chapter 4 was used to control the characteristics of the boundary layer at the inlet to the cascade. Since the shape of the profiles shown in Figure 6.13 were relatively independent of pitchwise position, it was decided to take the present measurements at the geometric projection of the centre of the test passage.

Preliminary investigations showed that the suction system was capable of providing enough suction to control the boundary layer over a reasonable range of the displacement thickness. With the exhauster fans in operation (one for each chamber), it was possible to obtain below atmospheric pressures of up to 39.88 mm of water (15.7

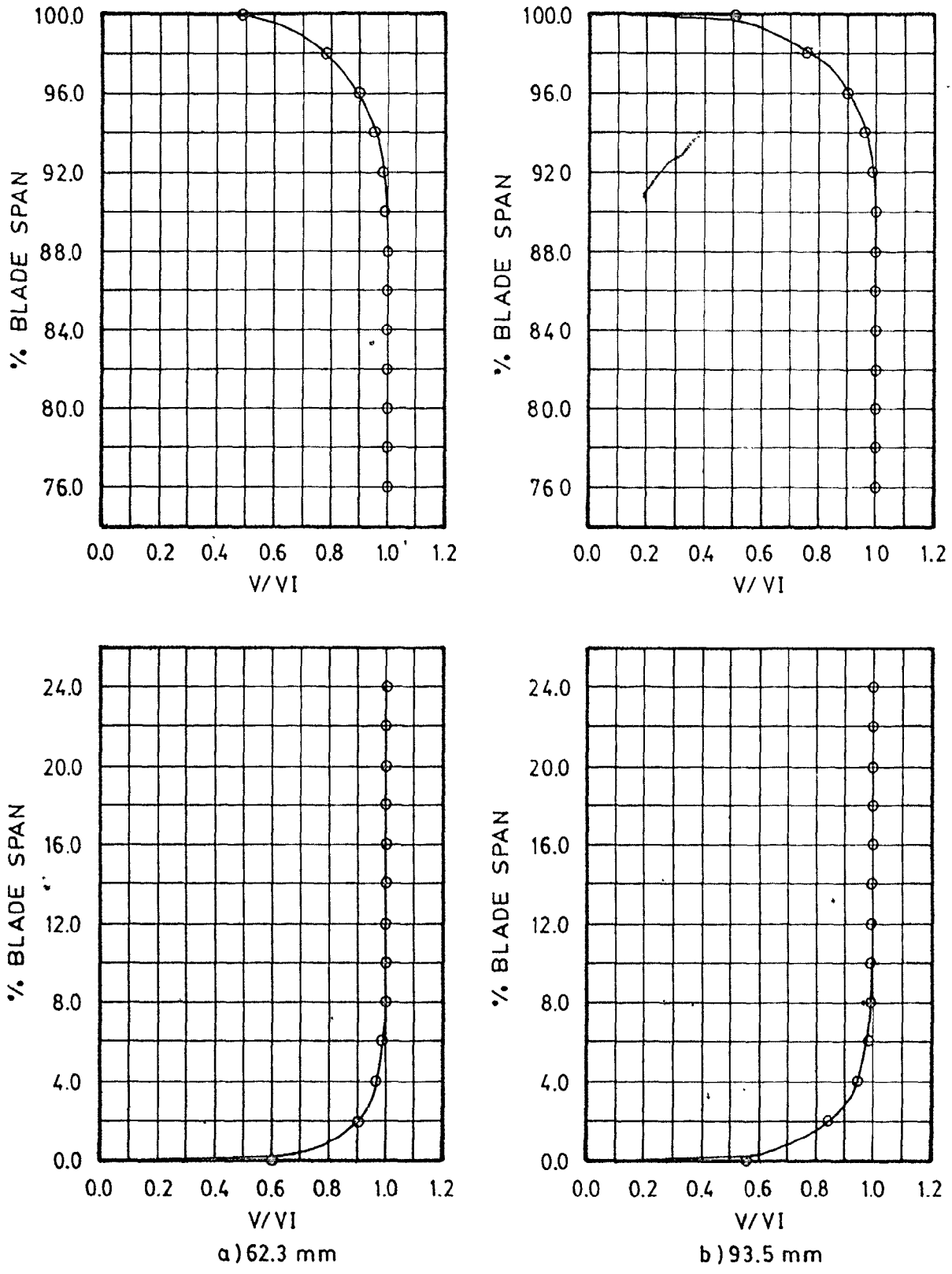

Figure 6.13 Boundary Layer Profiles at the Inner and Outer Endwalls.

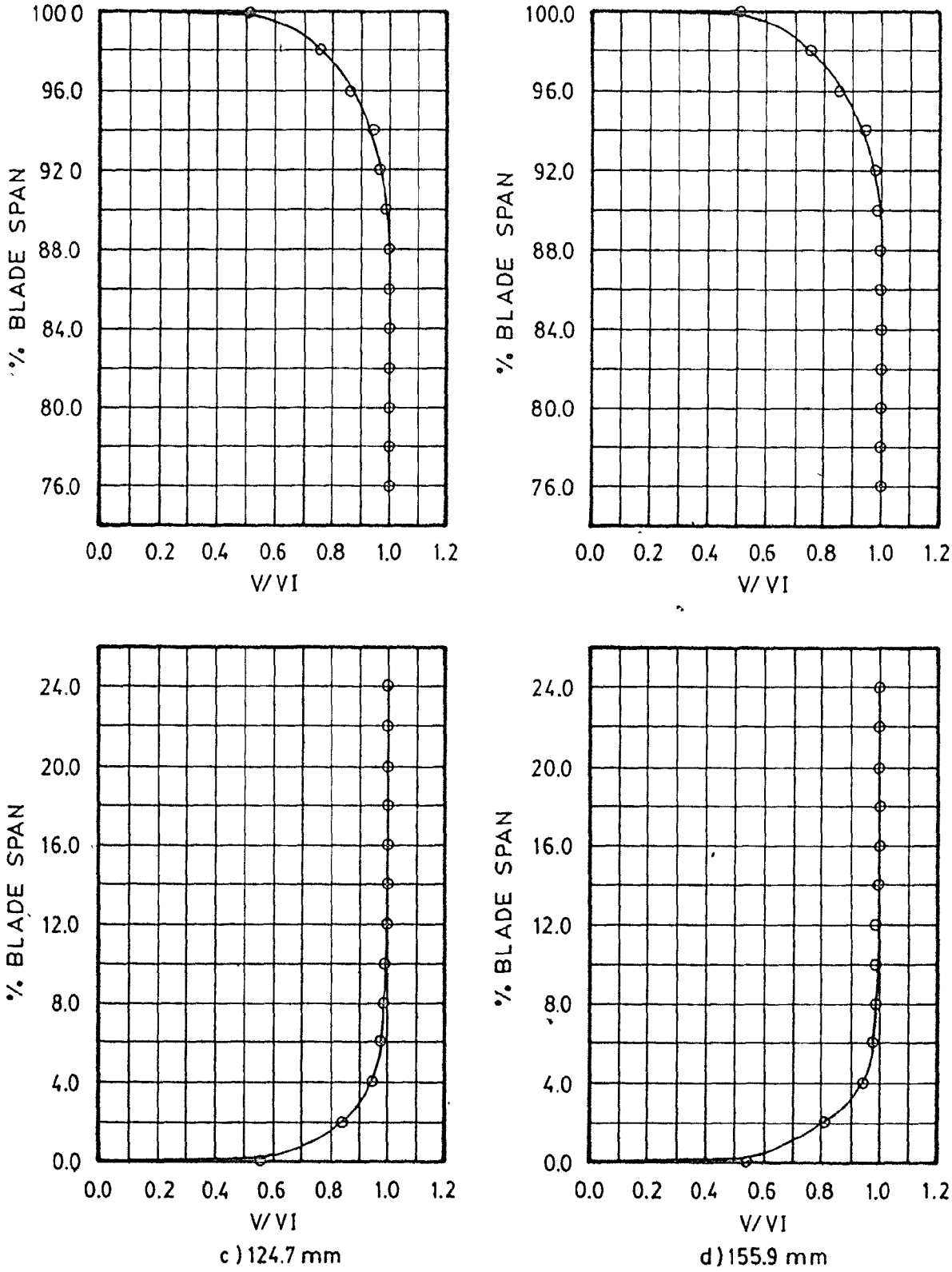

Figure 6.13 (Continued).

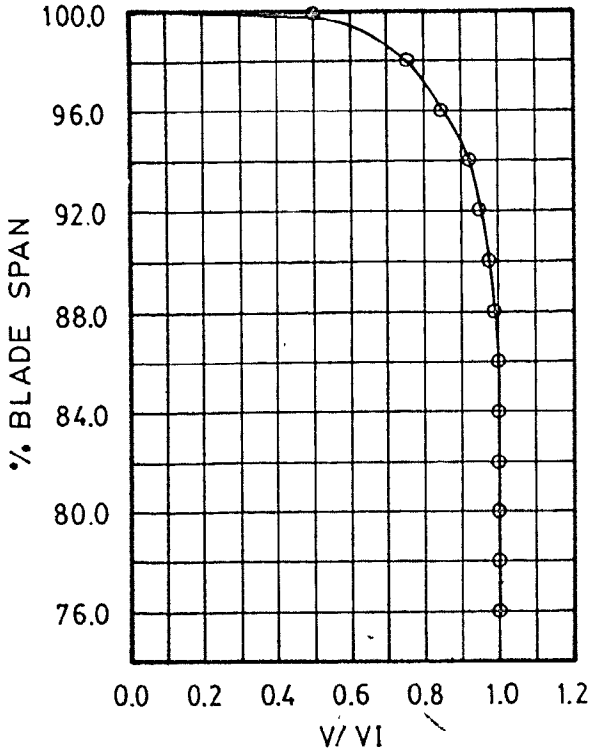

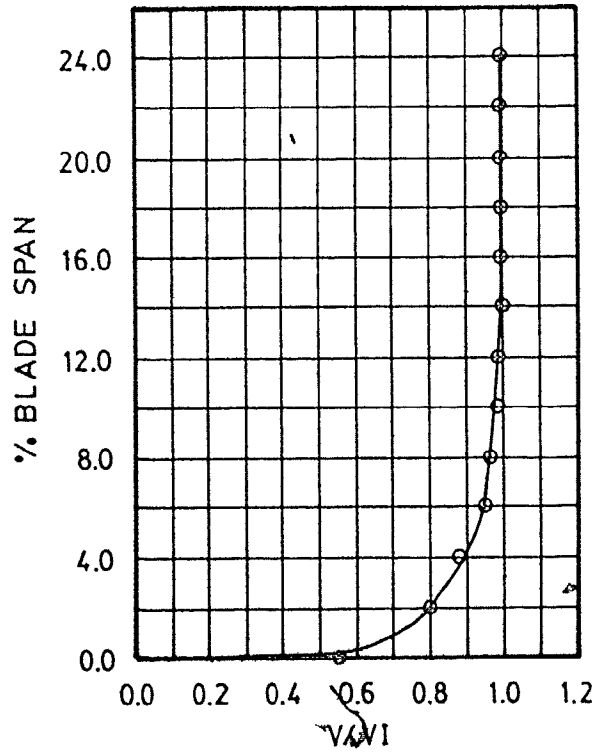

e) 187.0 mm

Figure 6.13 (Continued).

inches) within the inner and outer endwall suction chambers. Under no suction conditions, a below atmospheric pressure of 4.57 mm of water (1.8 inches) was observed in each chamber. Under maximum suction conditions, the boundary layer probes were traversed (within the boundary layer) in the pitchwise direction. No variations in the pitot pressure were observed, indicating that the suction through the porous surface was uniform.

Four values of suction were chosen for the investigation, each being finely regulated by the gate valves installed in the suction lines. The results of the spanwise traverses are shown in Figures 6.14 and 6.15. The shape factor H^* and the dimensionless boundary layer displacement thickness δ_1^*/C, corresponding to each applied suction condition, are provided on the diagrams. The plotting symbols have been arranged in order of increasing suction. The first symbol represents the conditions of no suction and the remainder represent values of applied suction corresponding to -11.68 mm (-4.6 inches), -18.79 mm (-7.4 inches), -25.65 mm (-10.1 inches) and -39.88 mm (-15.7 inches) of water respectively. Values of suction pressure below -25.65 mm (-10.1 inches) of water produced no significant reduction in δ_1^* and for this reason it was decided not to exceed this value during the examination of the exit flow parameters (Chapter 8).

Under maximum suction conditions in both chambers,

---

*H = displacement thickness/momentum thickness.

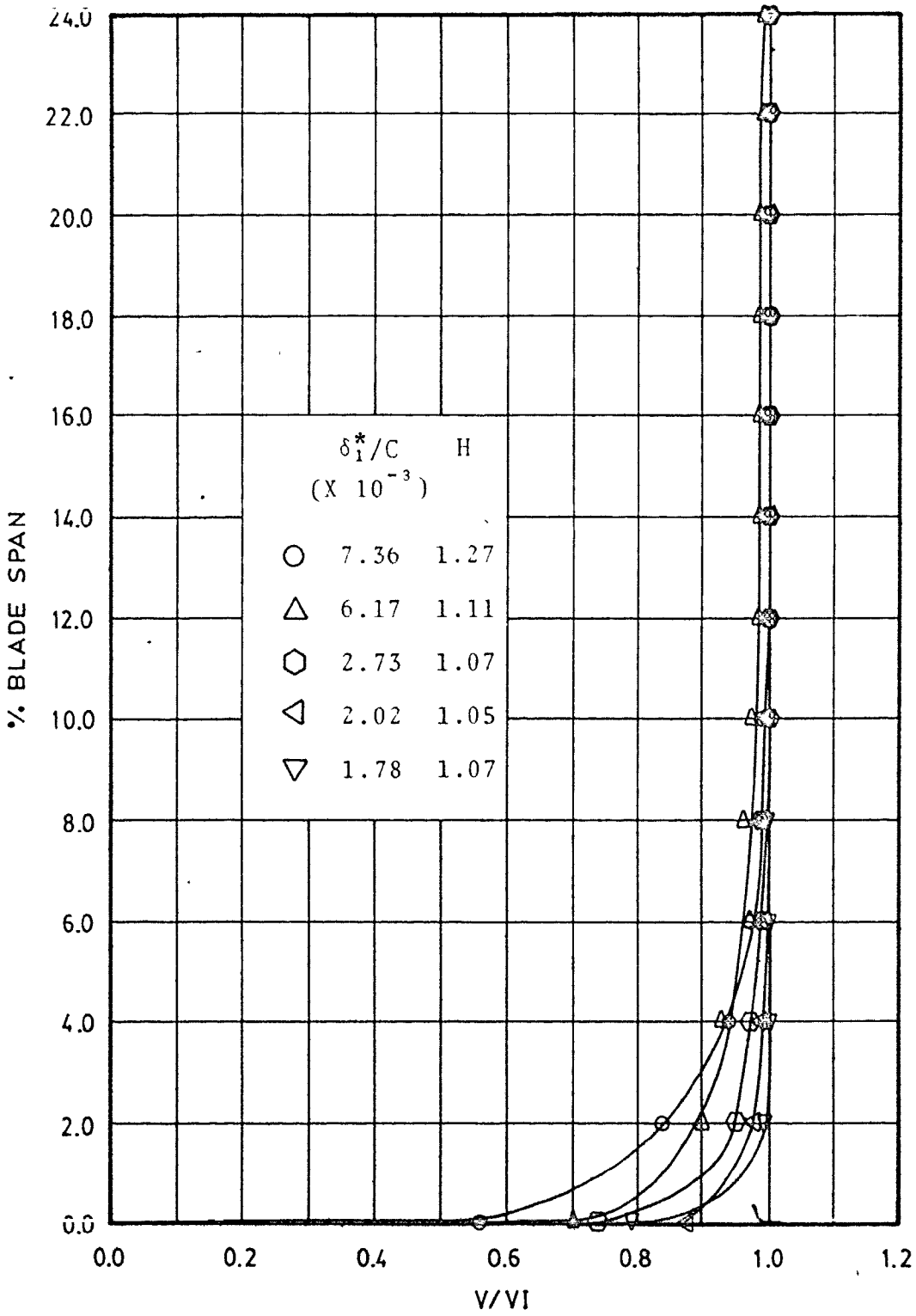

Figure 6.14 The Effect of Suction on the Boundary Layer Profiles at the Inner Endwall at the Geometric Centre of the Test Passage.

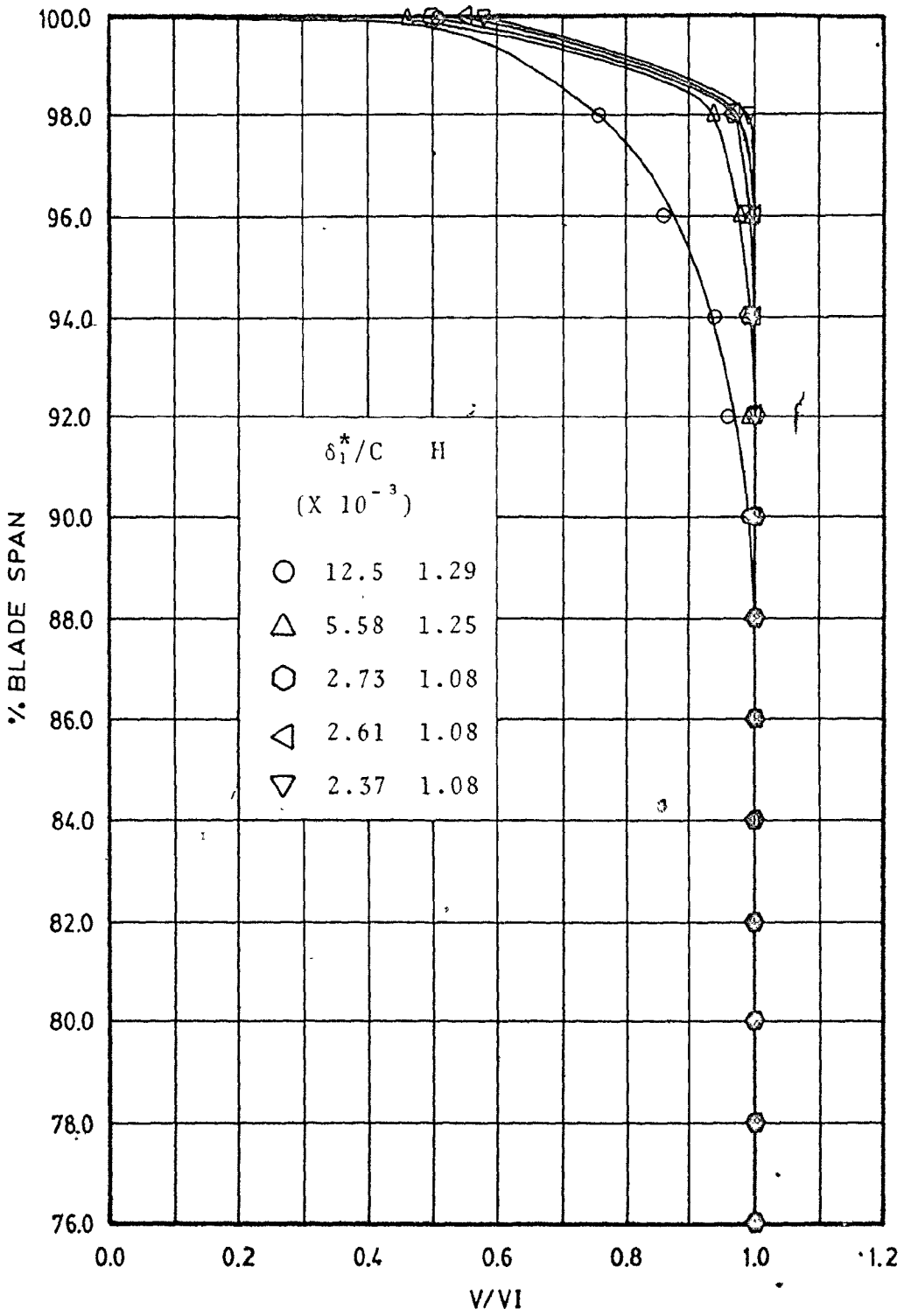

Figure 6.15 The Effect of Suction on the Boundary Layer Profiles at the Outer Endwall at the Geometric Centre of the Test Passage.

a complete spanwise traverse was conducted with the Kiel probe to ensure that the mainstream was unaffected by reductions in the boundary layer. The resulting velocity profile was identical to those shown in Figures 6.8 through 6.12.

6.6 Turbulence Intensity at the Inlet Measuring Station

The turbulence intensity was calculated from measurements taken with a DISA Constant Temperature Anemometer Type 55A01 at the geometric projection of the centre of the test passage. The measurements were taken (without boundary layer suction) at three spanwise locations using a miniature DISA hot wire probe Type 55P13. The probe was calibrated in the potential core of the calibration nozzle shown in the photograph of Figure 6.16. The shop air supply was sufficient to produce core speeds in excess of 50 m/s. The calibration curve is shown in Figure 6.17. At each of the three spanwise locations, the r.m.s. turbulence level was measured over a speed of 0 to 40 m/s. The percentage turbulence intensity is defined as follows:

$$\% \text{ turbulence} = \frac{u}{V} \times 100 = \frac{e_{r.m.s.} \times 100}{V \frac{dE}{dV}} \qquad (6.1)$$

where

$e_{r.m.s.}$ is the r.m.s. voltage measured with the true r.m.s. digital multimeter.

CAPTIONS FOR FIGURE 6.16

A Constant Temperature Anemometer

B Fluke Digital Multimeter

C Keithley TRMS Digital Multimeter

D Shop Air Supply

E Calibration Nozzle

F Hot Wire Probe

G Pitot-Static Probe

H Betz Manometer

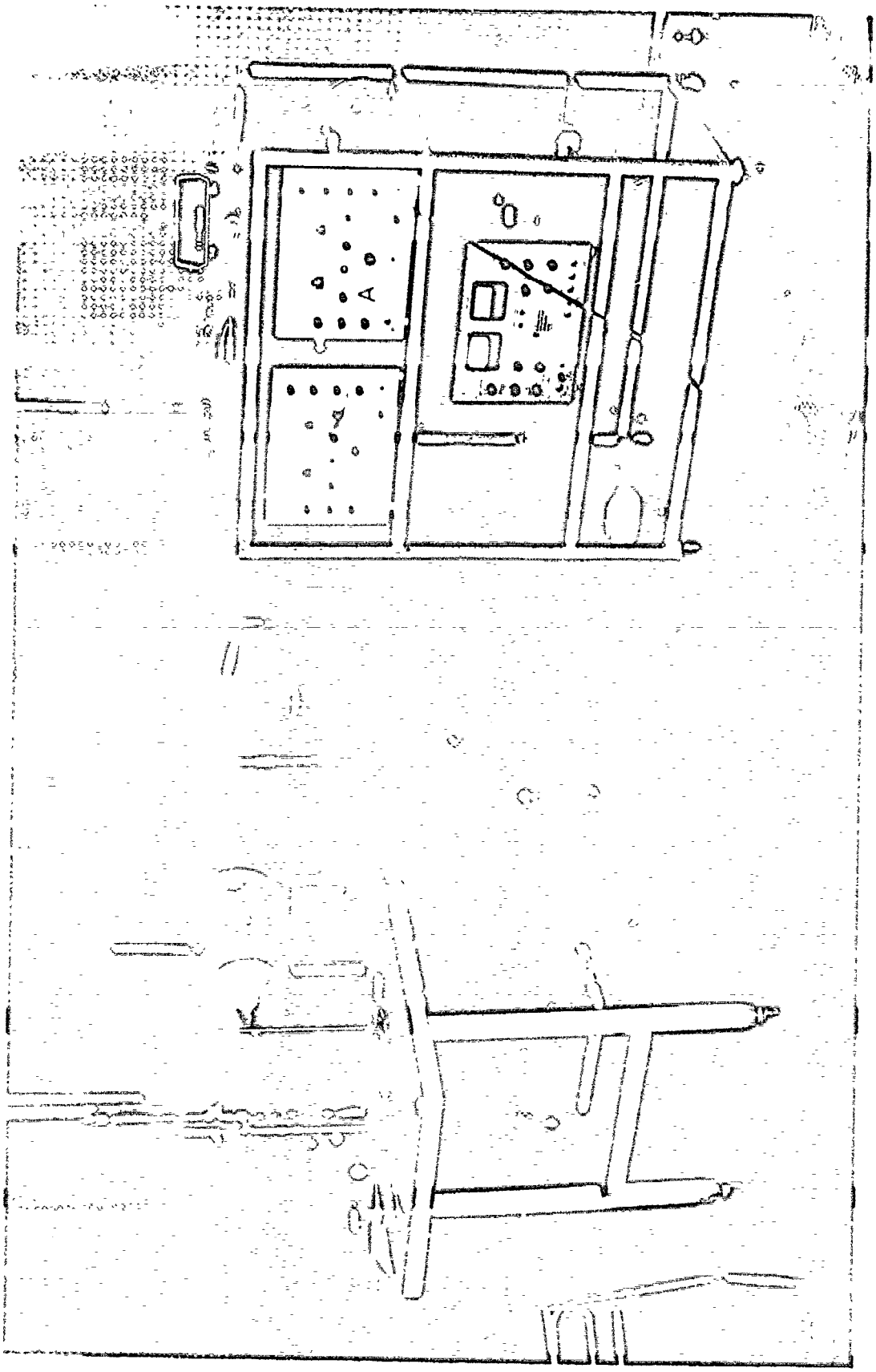

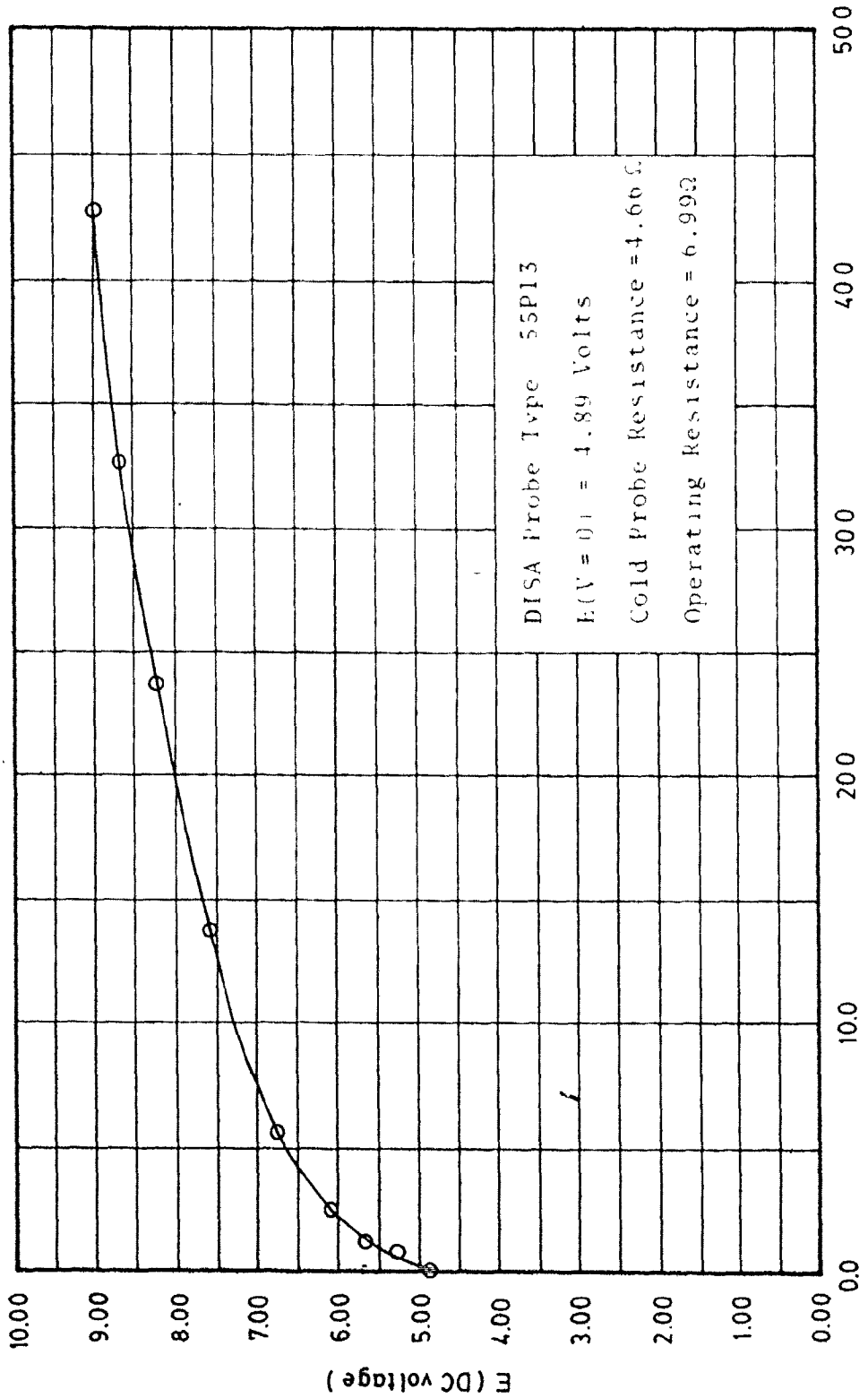

Figure 6.17 Calibration Curve for the Hot Wire Probe.

$\frac{dE}{dV}$ is the slope of the calibration curve at speed V. The calculated turbulence intensities shown in Figure 6.18 are considerably lower than those reported by Elshammaa {17} for the three-dimensional cascade test rig.

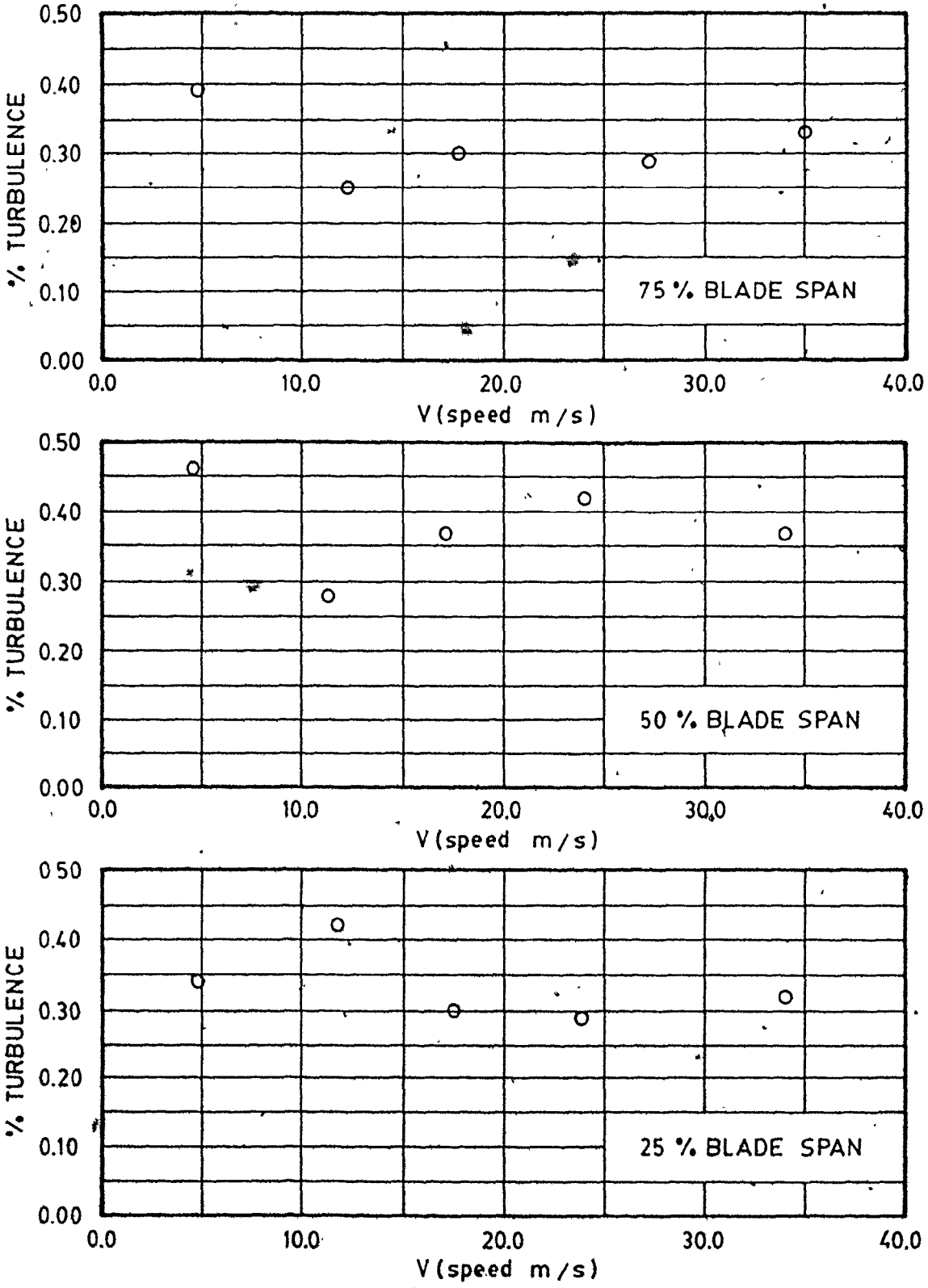

Figure 6.18 Turbulence Intensity at Various Percentages of the Blade Span.

CHAPTER 7

THE CASCADE TEST PASSAGE PRESSURE DISTRIBUTION

The pressure distributions presented in this chapter were developed from a total of 130 static pressure readings which were taken within the test passage. The readings were taken without boundary layer suction. Chapter 4 provides the axial, pitchwise and spanwise positions of the passage static pressure taps. The pressure distributions are presented in the form of a dimensionless static pressure coefficient defined as:

$$Cp_S = \frac{P - P_1}{\frac{1}{2}\rho\ VI^2} \qquad (7.1)$$

where

- P is the measured static pressure at a pressure tap.
- P_1 is the measured free stream static pressure at the inlet measuring station.
- $\frac{1}{2}\rho VI^2$ is the dynamic head at the inlet measuring station based on the average velocity across the test passage at mid-span.

The contour maps in this chapter show the variation in Cp_S in 0.1 increments.

7.1 Pressure Distribution on the Blade Surfaces

Contours of the static pressure coefficient for the blade pressure and suction surfaces are shown in Figures 7.1 and 7.2 respectively. Over the first 50% of the axial chord (Figure 7.1), there is only a slight variation in the measured static pressure on the blade pressure surface. The near symmetric pressure distribution about the blade midspan indicates that no spanwise pressure gradient exists. This is due to the two-dimensional nature of the test section with its constant pitch/chord ratio. Over the remaining portion of the blade surface, the pressure decreases rapidly indicating that the flow is accelerating as it approaches the throat of the test passage.

On the suction surface of the blade (Figure 7.2), the axial pressure gradient is steepest near the leading edge. At about 10% axial chord there is a zone of low pressure (Cp_s = -1.0). Spanwise pressure gradients are observed over the remaining portion of the suction surface and these are thought to be associated with the secondary flow occurring within the test passage. A comparison with Elshammaa's results {17} (same blade profile in an annular test rig) shows that the Cp_s contour patterns are quite similar but Elshammaa's radial distribution of pressure on the suction surface is more pronounced.

Figure 7.3 a) through e) shows the variation of the static pressure along the blade pressure and suction

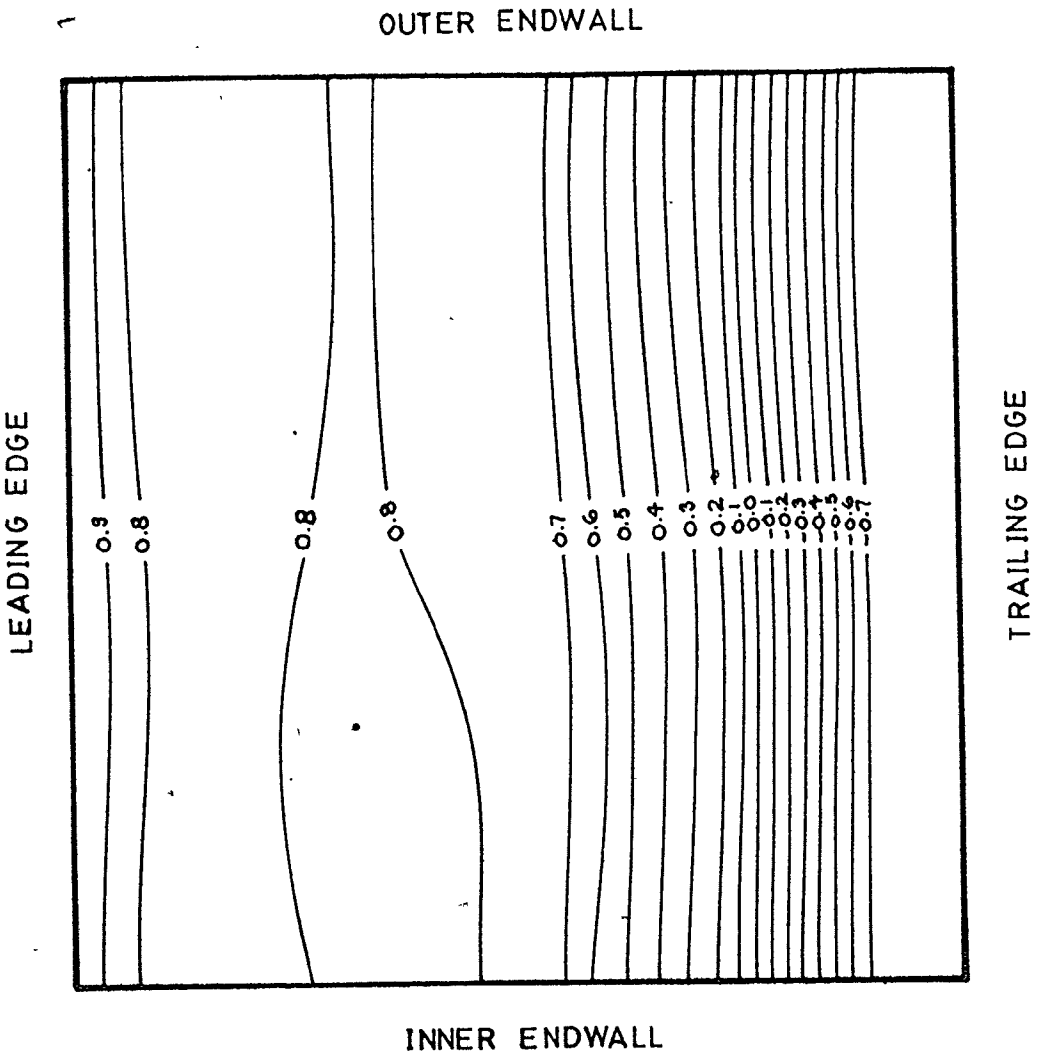

Figure 7.1 Cp_s Contours on the Blade Pressure Surface.

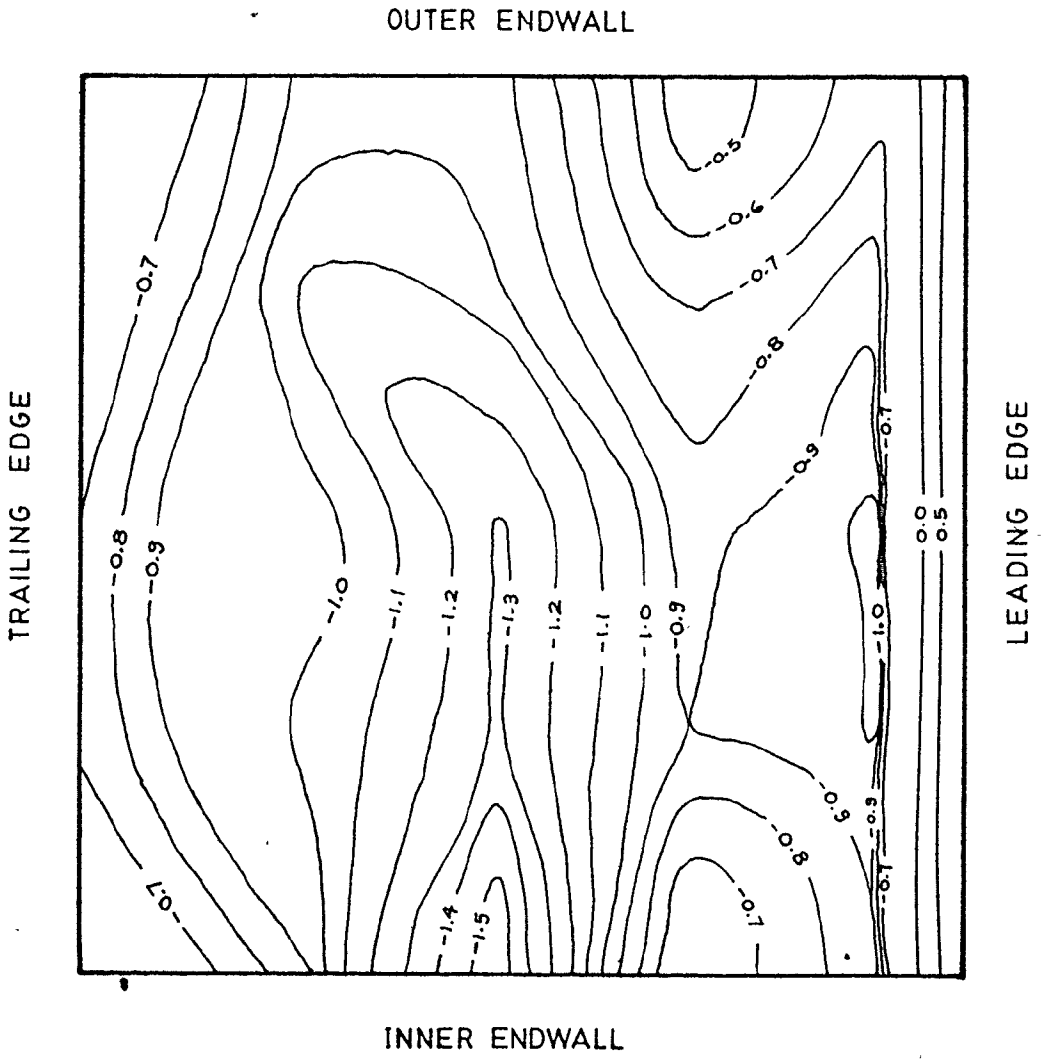

Figure 7.2 Cp_s Contours on the Blade Suction Surface.

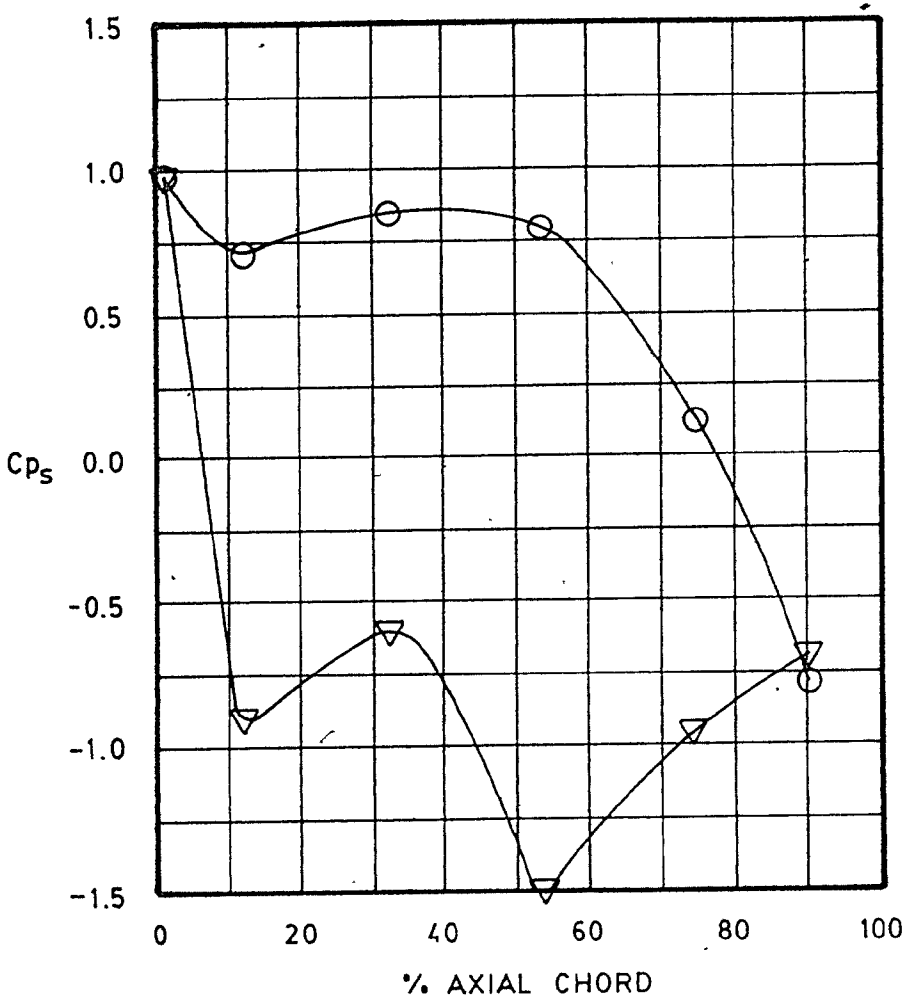

a) Z/H = 7 %

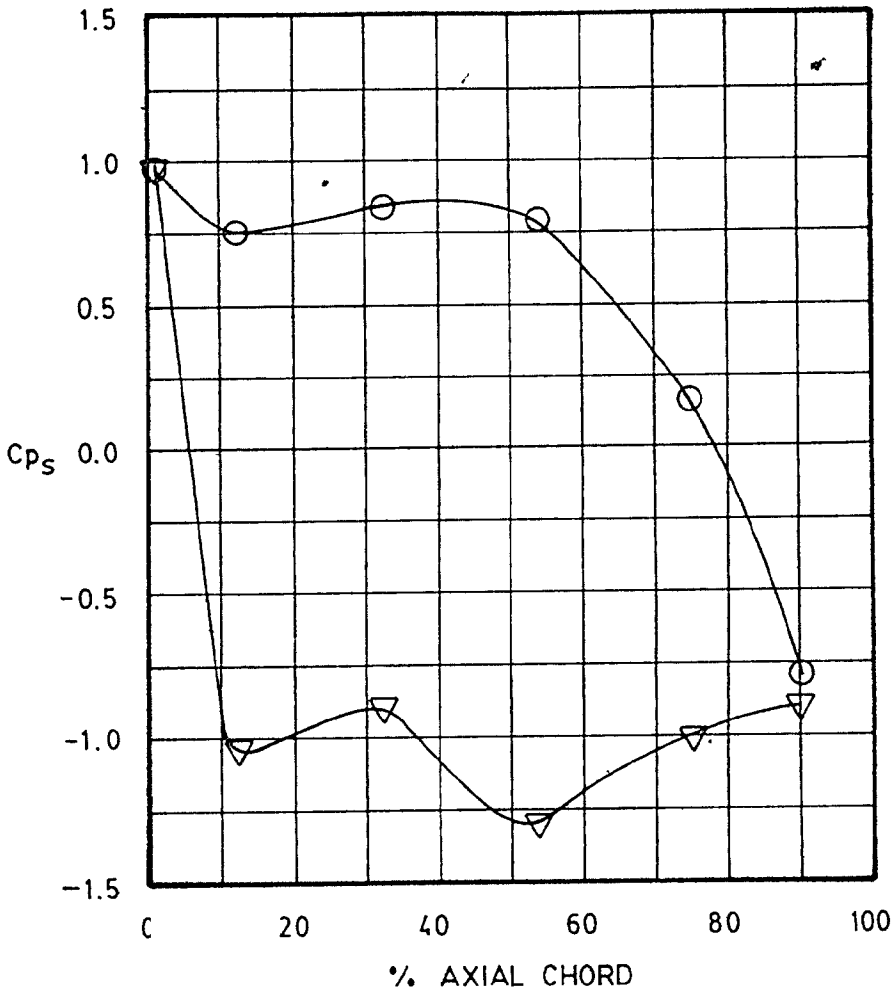

b) Z/H = 27 %

Figure 7.3 Blade Surface Pressure Distribution.

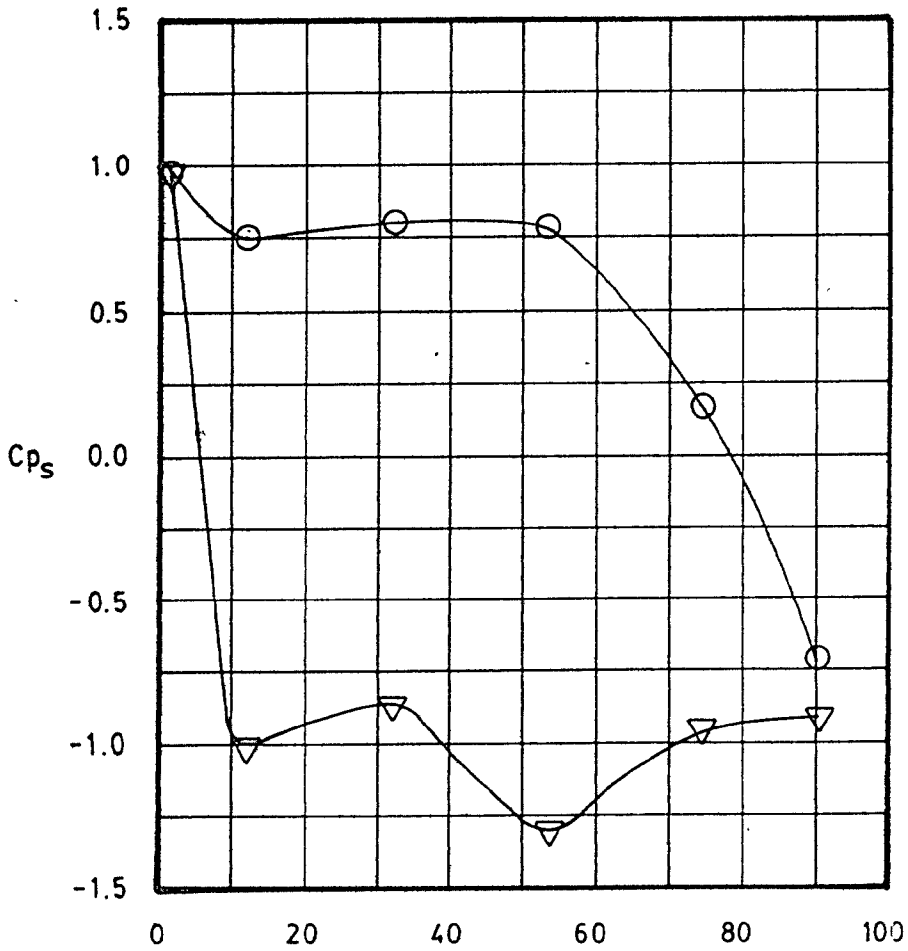

c) Z/H = 50 %

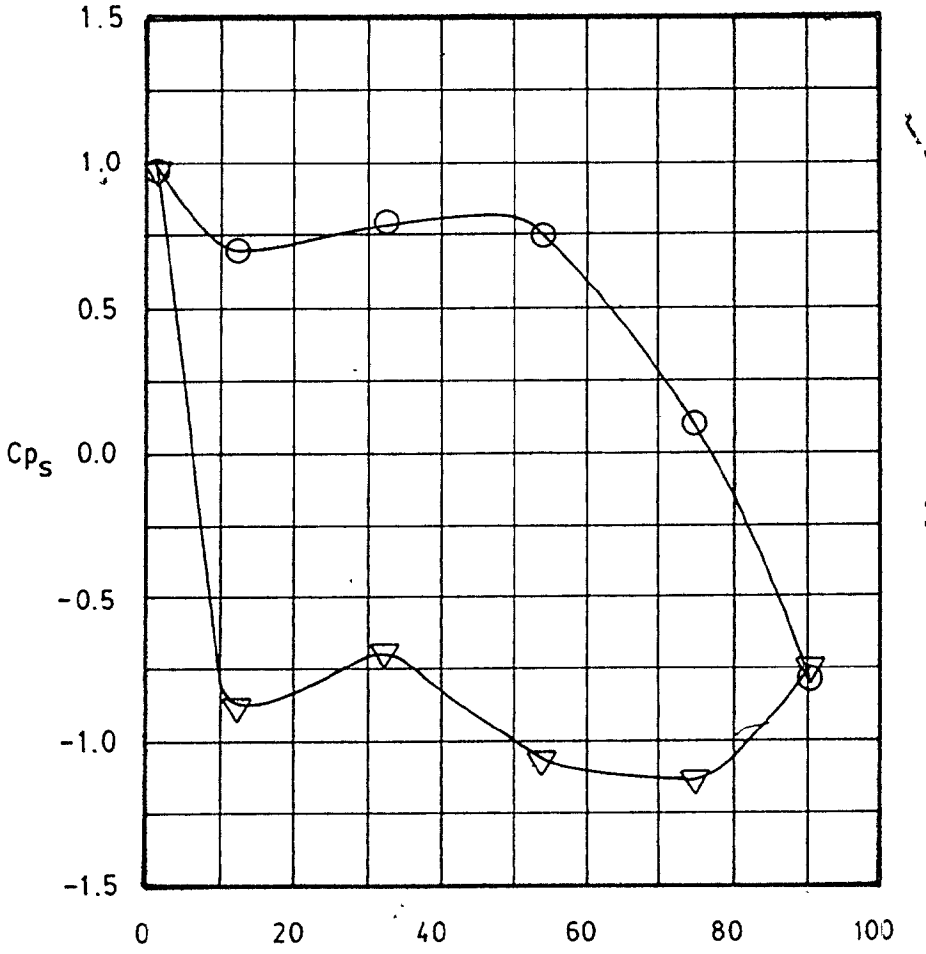

d) Z/H = 75 %

Figure 7.3 (Continued).

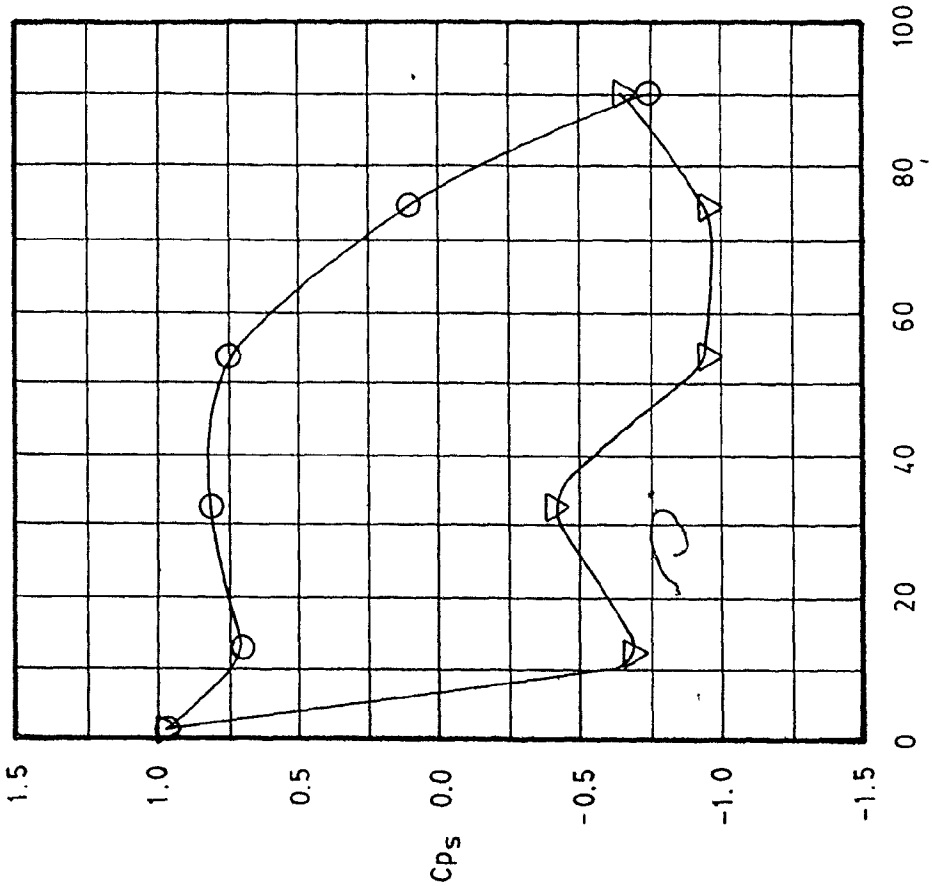

e) Z/H=94 %

Figure 7.3 (Continued).

surfaces (at 7%, 27%, 50%, 75% and 94% blade span) giving an indication of the blade loading (defined as the area enclosed by the curves). By studying Figures 7.1 and 7.2, it can be seen that there is almost no spanwise pressure gradient at midspan and one would expect to see the highest blade loading at this position. This is verified in Figure 7.3 c). Elshammaa {17} found that the maximum blade loading occurred at 75% blade span due to the varying pitch/chord ratio. The blade loading is somewhat less near the endwalls (Figure 7.3 a) and e)). The pressure on the pressure surface of the blade is fairly constant within the first 50% axial chord then decreases rapidly towards the trailing edge, indicating that the flow is accelerating in this region.

The pressure distribution on the suction surface, over the first 11% axial chord, shows a rapid flow acceleration. Up to approximately 32% axial chord, the static pressure rises slightly due to possible local flow separation. The pressure drops again to about 53% axial chord and then shows a rising trend towards the cascade exit. The rise in static pressure up to the throat (73% axial chord) could be caused by separation due to the secondary flow. Once past the throat region, the flow decelerates and the pressure continues to rise.

In Figure 7.4 a two-dimensional potential flow solution, reported by Elshammaa {17}, is compared with the

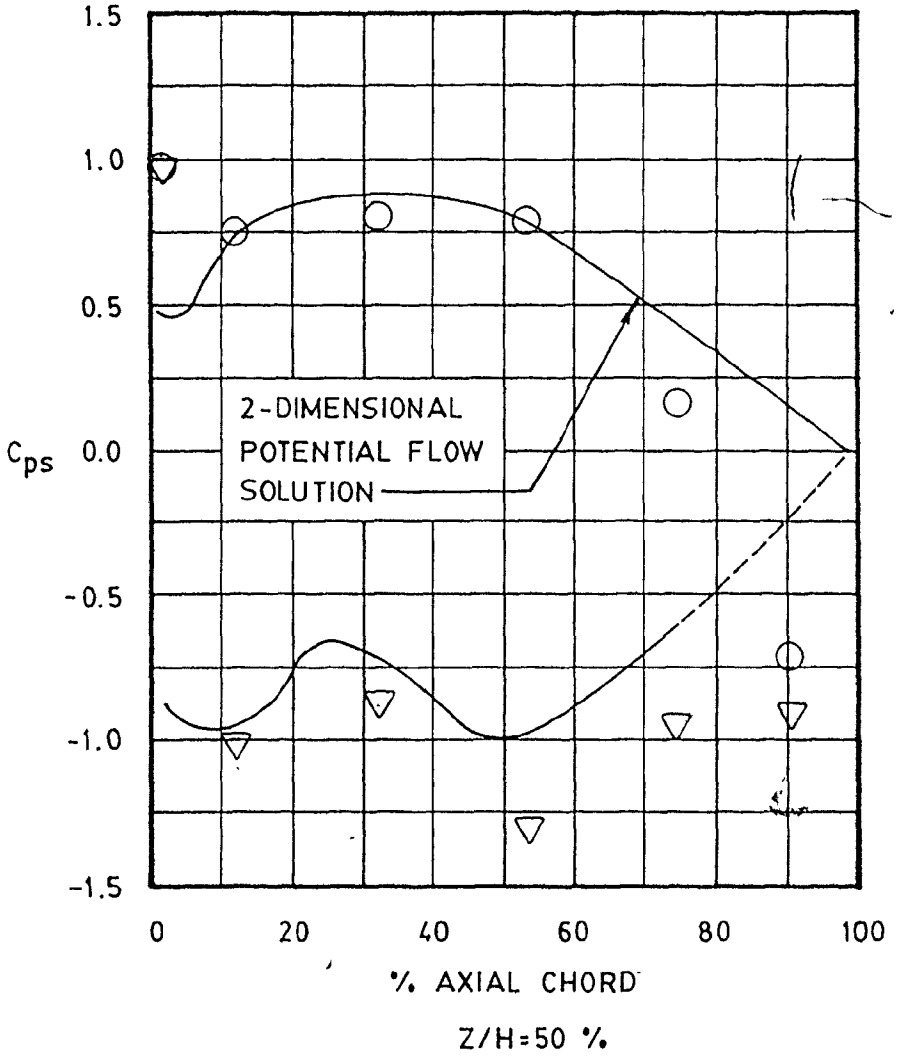

Figure 7:4 Comparison of the Blade Surface Pressure Distribution at 50% Blade Span with the Two-Dimensional Potential Flow Solution Reported in Ref. {17} .

present blade surface pressure distribution at 50% blade span. The agreement is quite good on both surfaces up to about 50% axial chord. Throughout the remainder of the passage, the measured pressure distribution shows some deviation but generally follows the pattern depicted in the analytical model.

7.2 Pressure Distribution on the Test Passage Endwalls

The cascade inner and outer endwall pressure distributions are given in Figures 7.5 and 7.6 respectively. Because the rig is two-dimensional (constant pitch/chord ratio), both distributions show a similar pattern. The zone of minimum pressure (Cp_s = -1.0) is located upstream from the blade throat at a position close to the suction surface. This same pattern was recognized by Langston et al. {26} and was associated with local separation due to the cross-channel migration of the endwall boundary layer. The authors compared their endwall pressure distribution to that calculated from a potential flow solution (for their particular cascade) and found considerable differences.

The orientation of the pressure gradients in Figures 7.5 and 7.6 (almost parallel to the pitchwise direction) indicate that the boundary layer fluid was indeed being swept towards the blade suction surface. Figure 7.7 shows the pitchwise variation in the static pressure

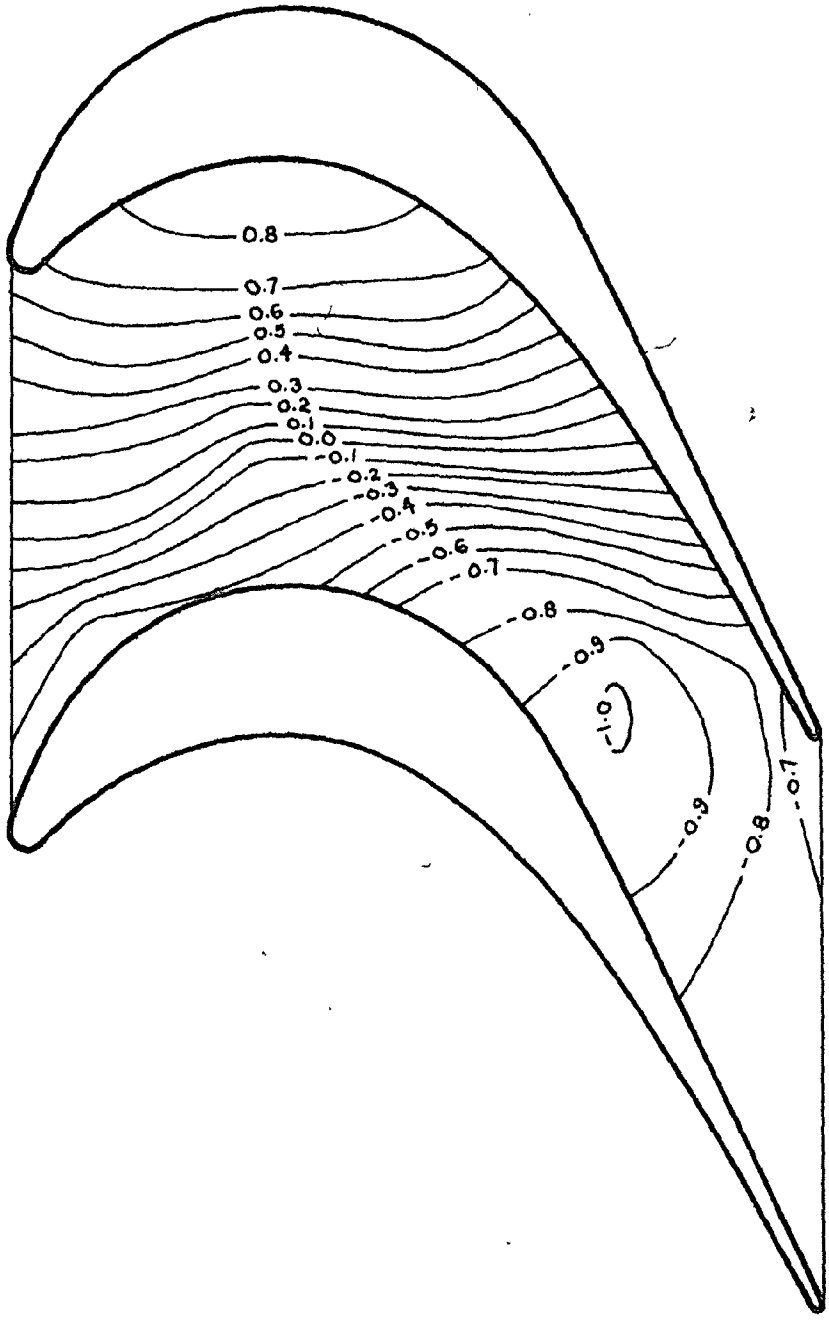

Figure 7.5 Cp_s Contours on the Inner Endwall.

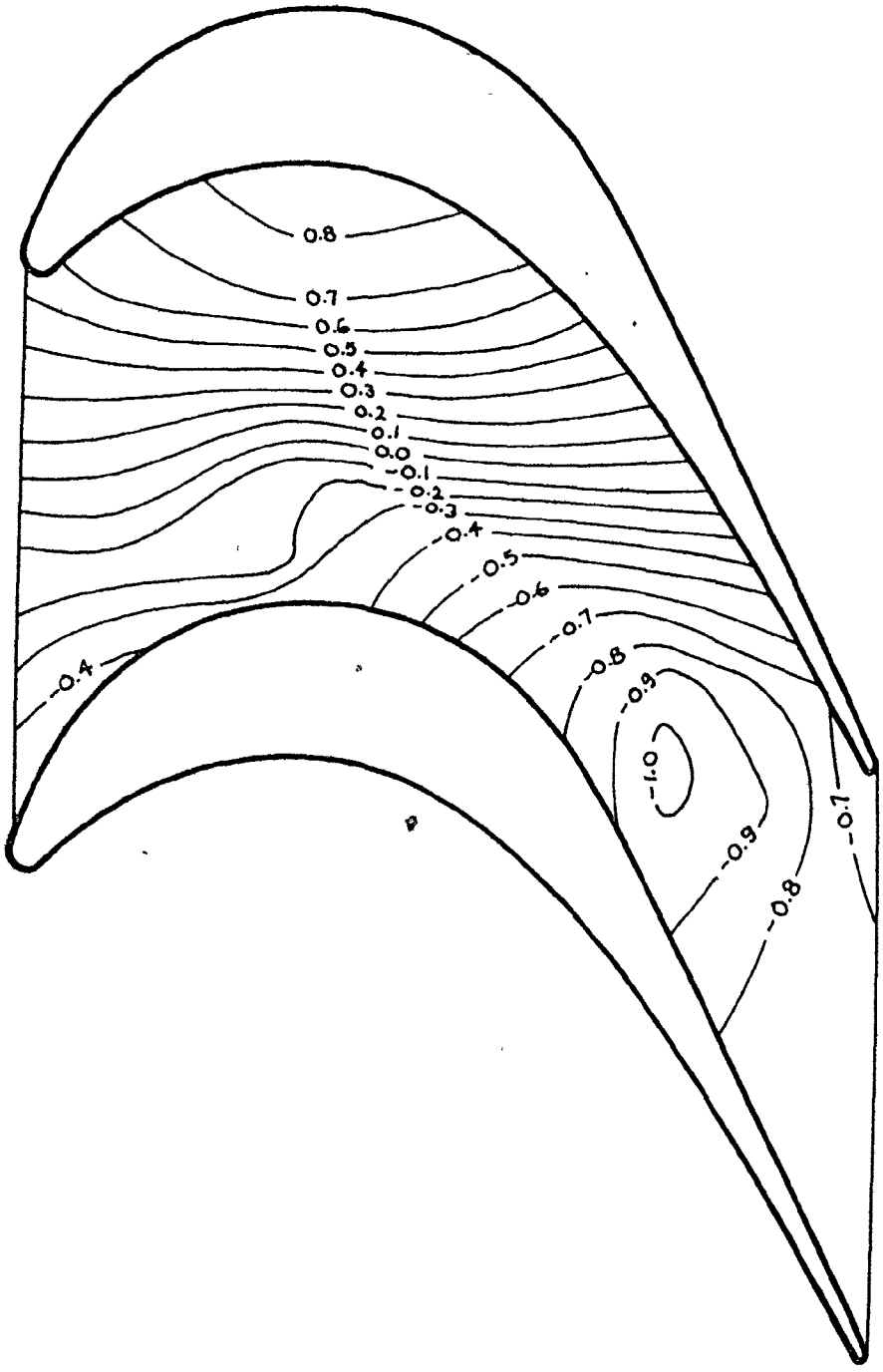

Figure 7.6 Cp_s Contours on the Outer Endwall.

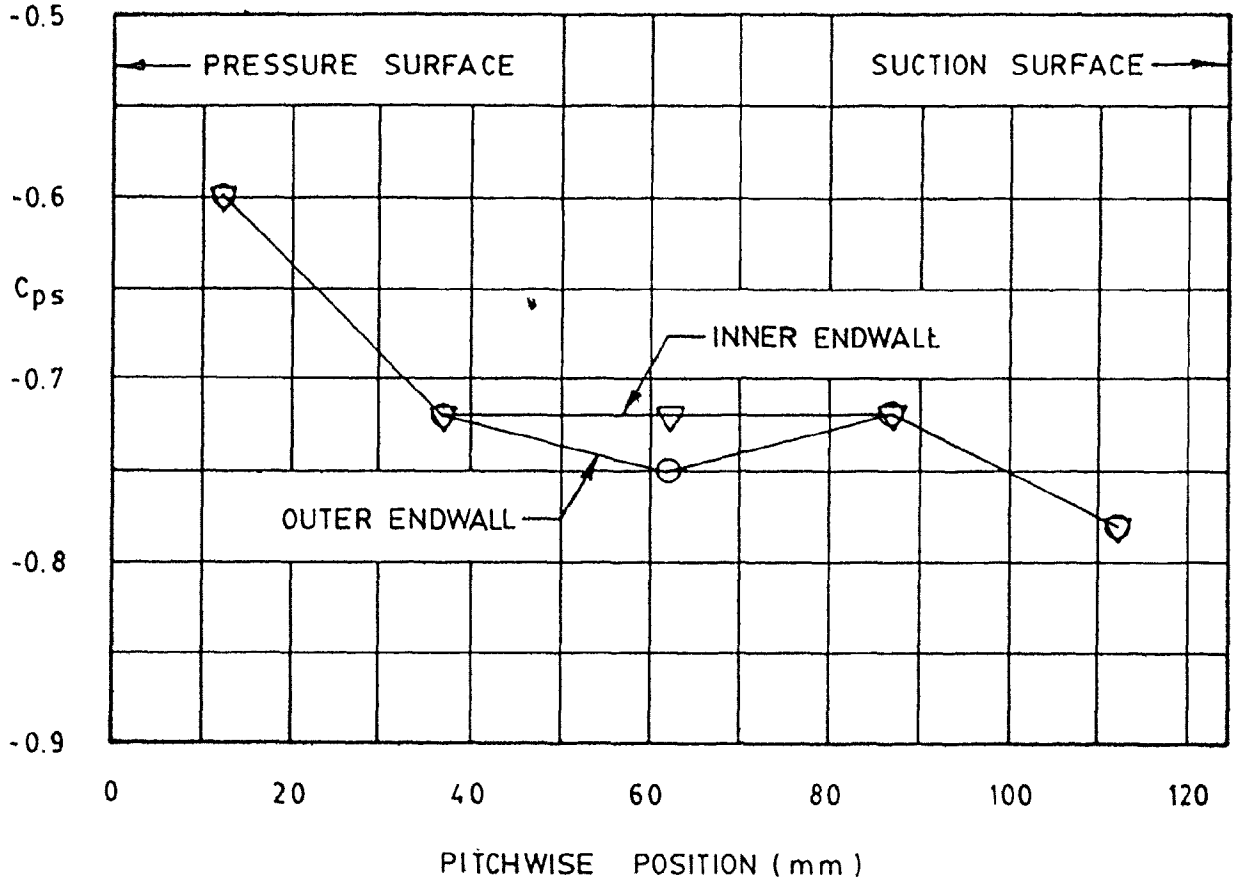

Figure 7.7 Endwall Static Pressure Distribution at the Cascade Exit.

across the cascade exit measured at both endwalls. Since the rig is two-dimensional, the distributions are almost identical. Tests conducted by Turner [27], at the exit of a rectilinear turbine-nozzle cascade, showed a similar pattern.

CHAPTER 8

EXAMINATION OF THE EXIT FLOW PARAMETERS

The effect of the inlet endwall boundary layers on the measured exit flow parameters is of primary interest in the present study. Five inlet flow conditions were selected, each being a distinct combination of the endwall boundary layer displacement thicknesses. For each inlet flow condition, the exit flow at exit measuring station A was traversed in the spanwise and pitchwise directions. The tests were conducted at a Reynolds number of 3.68×10^5 based on the blade chord. For the first test, measurements were taken over a distance of 2 S (from the geometric projection of the centre of passage III to the geometric projection of the centre of passage I) in the pitchwise direction in order to examine the flow periodicity at the cascade exit. The remaining four tests covered the geometric projection of the test passage (passage II). The three-dimensional five-hole probe was used to determine the flow pitch angle and the total and static pressure and the flow yaw angle was measured with the wedge probe. The probe readings in the spanwise direction were taken from 10% to 90% blade span in 10% increments. Similar measurements were taken at exit measuring station B (for the first inlet flow

condition) in order to assess the effect of flow mixing on the calculated losses.

The total and static pressure distributions in the plane of exit measuring station A are presented non-dimensionally in the form of the local total pressure loss coefficient Cp_0 and the local static pressure coefficient Cp_S . These were calculated from the total and static pressure readings and are defined as follows:

$$Cp_0 = \frac{P_{01} - P_0}{\frac{1}{2}\rho\ VI^2} \qquad (8.1)$$

$$Cp_S = \frac{P_1 - P}{\frac{1}{2}\rho\ VI^2} \qquad (8.2)$$

where

P_{01} is the measured inlet free stream total pressure at mid-span.

P_0 is the measured total pressure at a point in the plane of exit measuring station A .

$\frac{1}{2}\rho VI^2$ is the dynamic head at the inlet measuring station based on the average velocity across the test passage at mid-span.

P_1 is the measured inlet free stream static pressure corresponding to P_{01}.

P is the measured static pressure corresponding to P_0.

The data for calculating Cp_0, Cp_s, the pitchwise averaged values and the total pressure loss coefficient was reduced with the aid of a Hewlett-Packard 97 calculator.

Within this chapter, a description of each of the five selected inlet flow conditions is given. Contour plots of Cp_0 and Cp_s, corresponding to each inlet condition, are presented and discussed. The distribution of the pitchwise averaged values of the total pressure loss coefficient (Cp_{0m}), the exit angle deviation ($\Delta\alpha_2$) and the dimensionless axial velocity (Va/VI), for each inlet condition, are given, analyzed and compared with existing cascade data. The measured overall total pressure loss coefficients (Y_T) and secondary loss coefficients (Y_s) (corresponding to each inlet condition) are tabulated and compared to those calculated by existing correlations.

8.1 Chosen Inlet Conditions for the Exit Flow Studies

The various combinations of the endwall boundary layer displacement thicknesses, explained herein, were selected in a manner which was thought to show the greatest effect on the measured exit flow parameters. The chosen inlet conditions may be stated as follows:

a) No boundary layer suction at either the inner or the outer cascade inlet channel endwall.

b) Boundary layer suction at the inner endwall (corresponding to a suction chamber pressure of -11.68 mm (-4.6 inches) of water).

c) Boundary layer suction at the outer endwall (same value of suction pressure as in Case b)).

d) Boundary layer suction at both endwalls (same value of suction pressure as in Cases b) and c)).

e) Boundary layer suction at both endwalls (corresponding to suction chamber pressures of -25.65 mm (-10.1 inches of water).

Values of suction pressure below -25.65 mm (-10.1 inches) of water were not considered in the selection of the inlet conditions (see Chapter 6 Section 6.5).

8.2 Contour Plots of the Local Total Pressure Loss Coefficient

Figures 8.1 through 8.5 show the distribution of the local total pressure loss coefficient for the inlet conditions a) through e) respectively. The contours were plotted in 0.1 increments, in order to provide a reasonable picture of the total loss distribution. The reader views these plots from an assumed vantage point within the cascade passage looking downstream. An examination of the overall loss pattern presented in Figure 8.1 shows that reasonable periodicity was established in the plane of exit measuring station A.

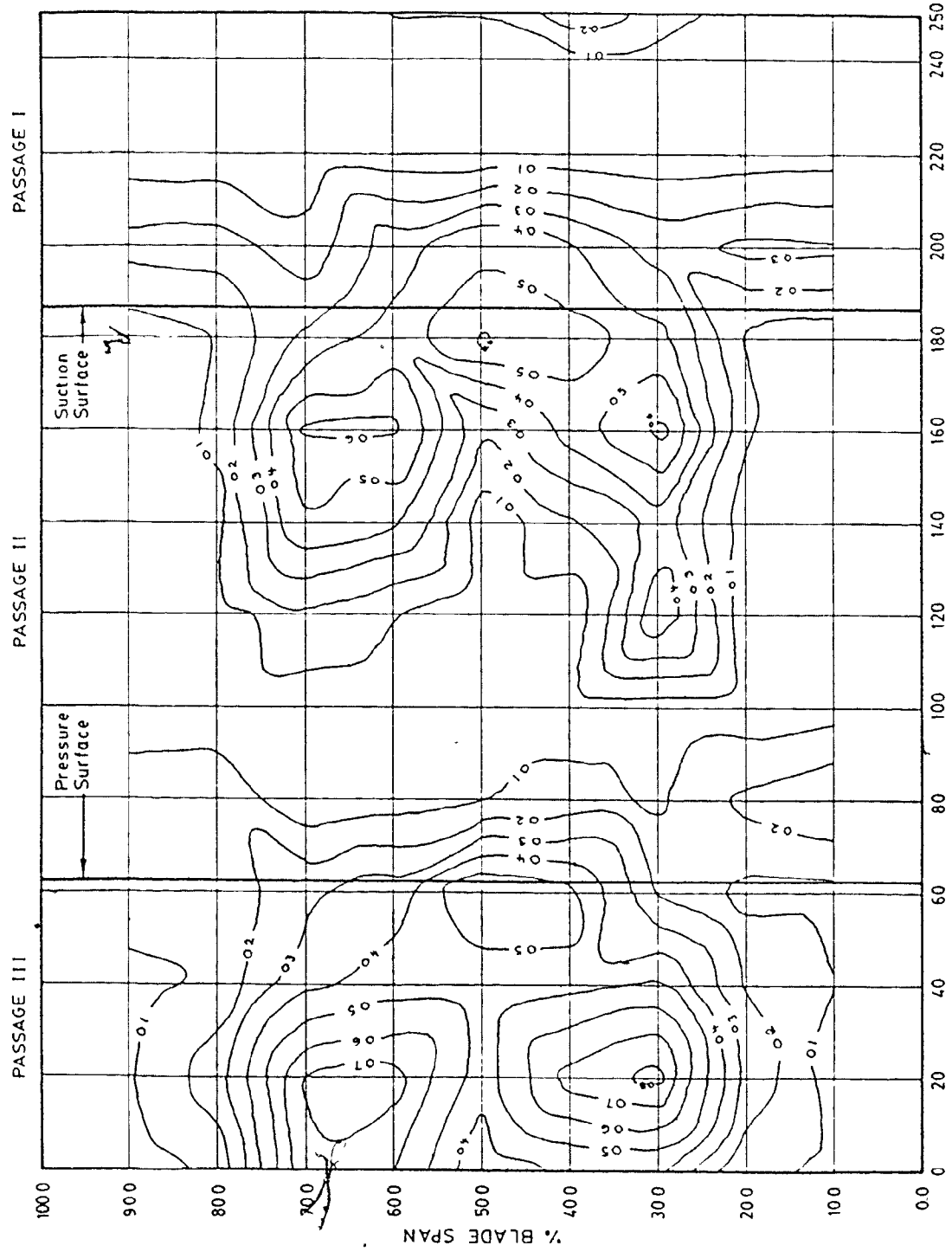

Figure 8.1 Distribution of the Local Total Pressure Loss Coefficient for Inlet Condition a) (No Suction).

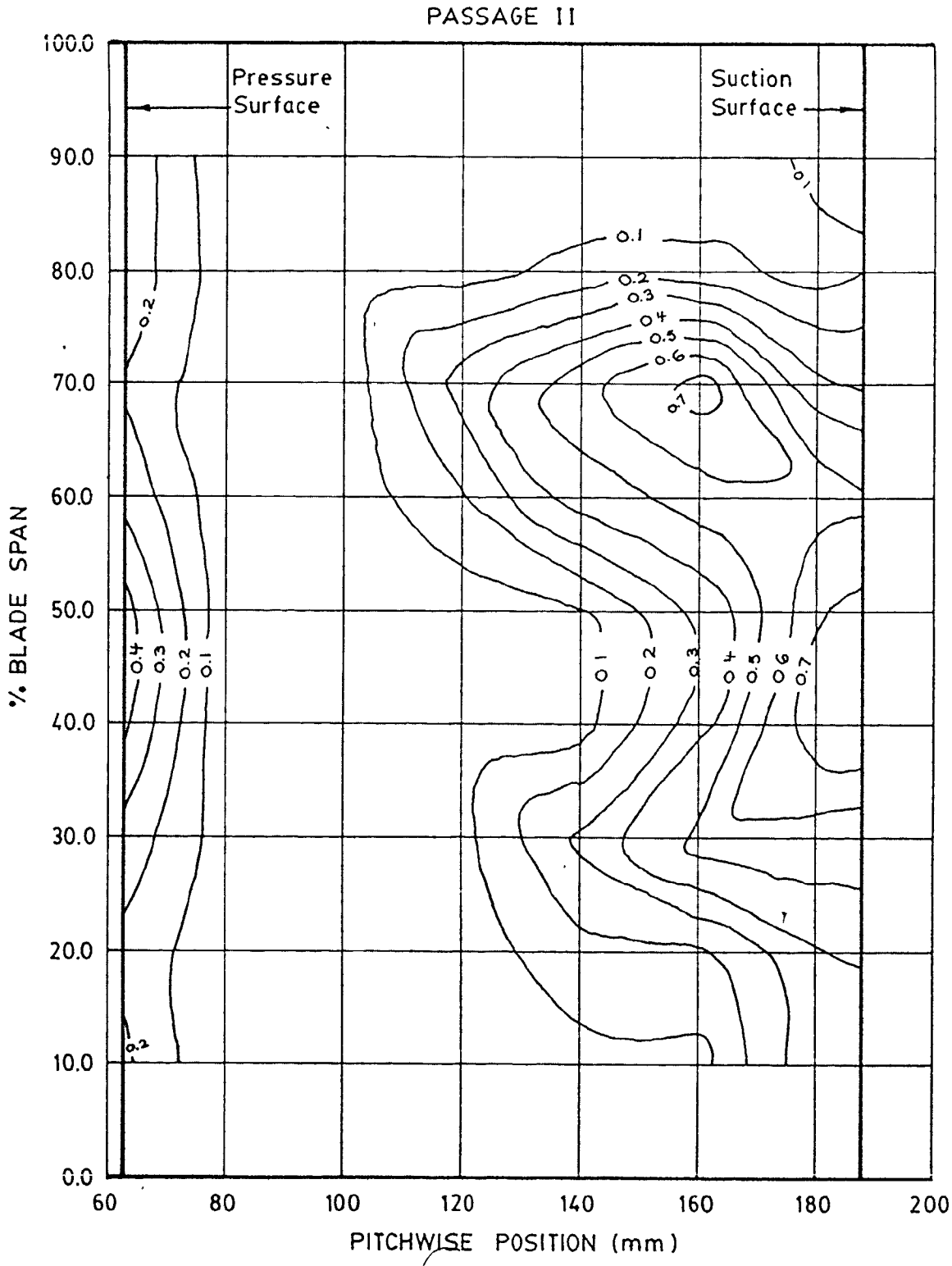

Figure 8.2 Distribution of the Local Total Pressure Loss Coefficient for Inlet Condition b) (Suction at the Inner Endwall Corresponding to -11.68 mm (-4.6 inches) of water).

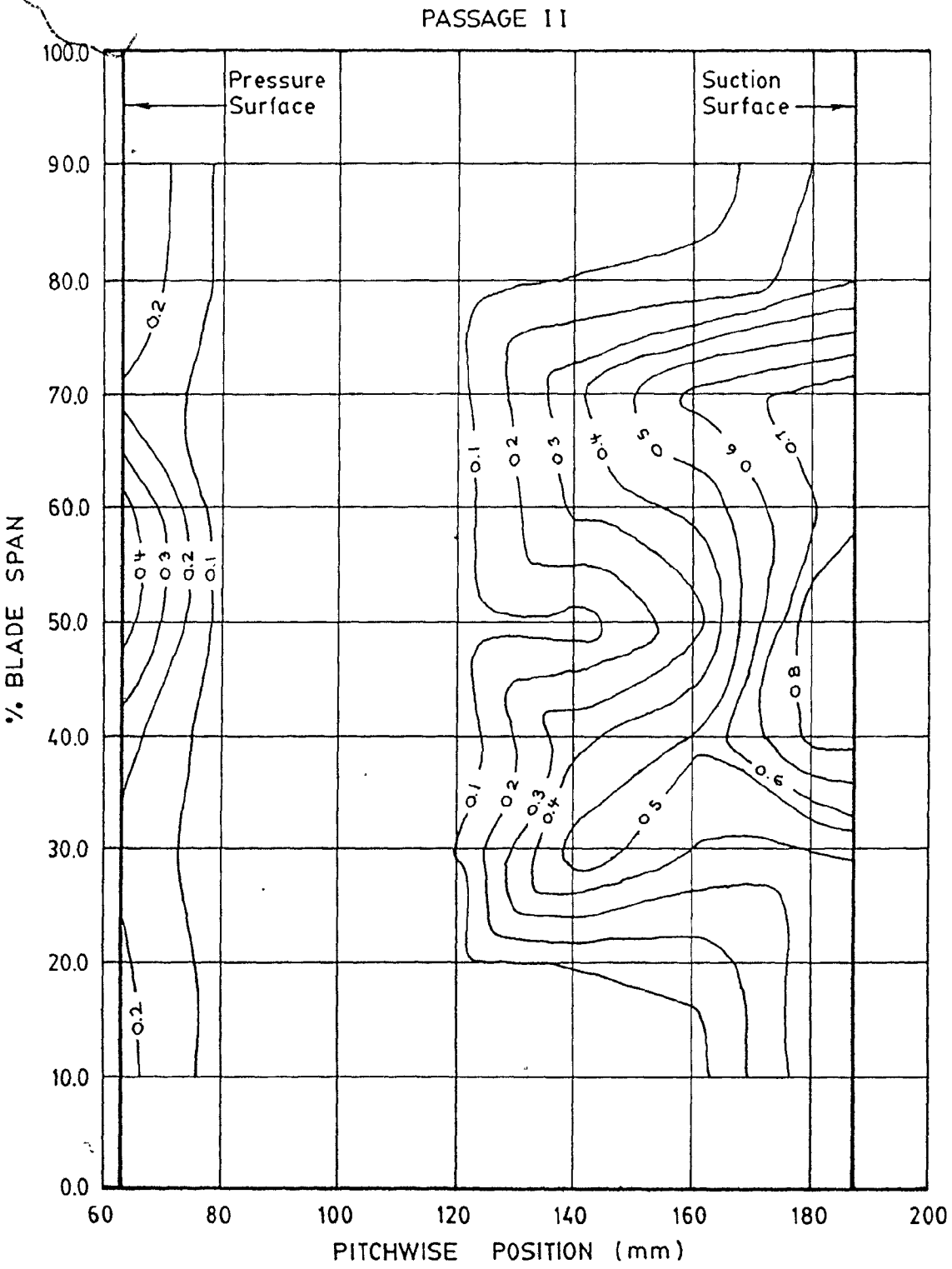

Figure 8.3 Distribution of the Local Total Pressure Loss Coefficient for Inlet Condition c) (Suction at the Outer Endwall Corresponding to -11.68 mm (-4.6 inches) of water).

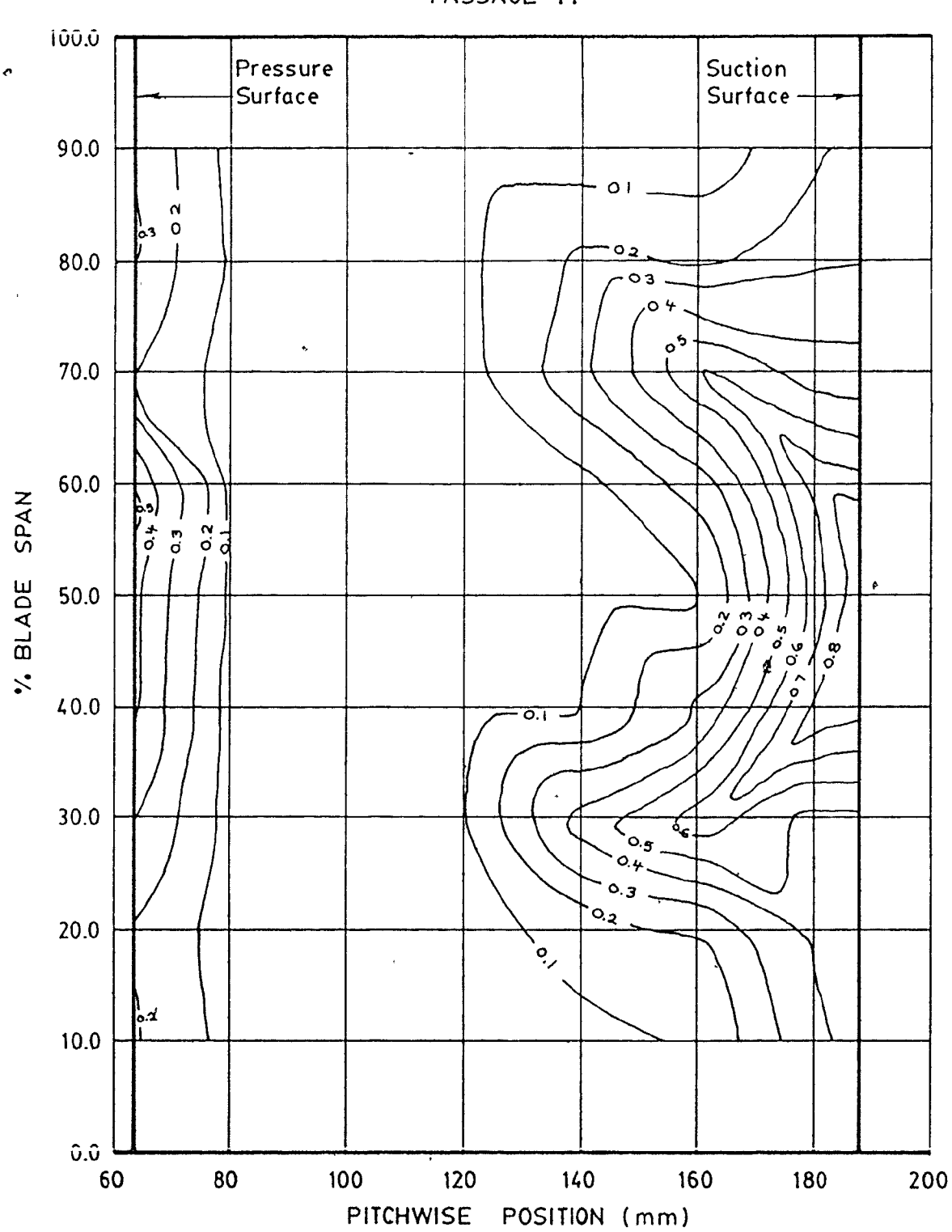

Figure 8.4 Distribution of the Local Total Pressure Loss Coefficient for Inlet Condition d) (Suction at Both Endwalls Corresponding to -11.68 mm (-4.6 inches) of water).

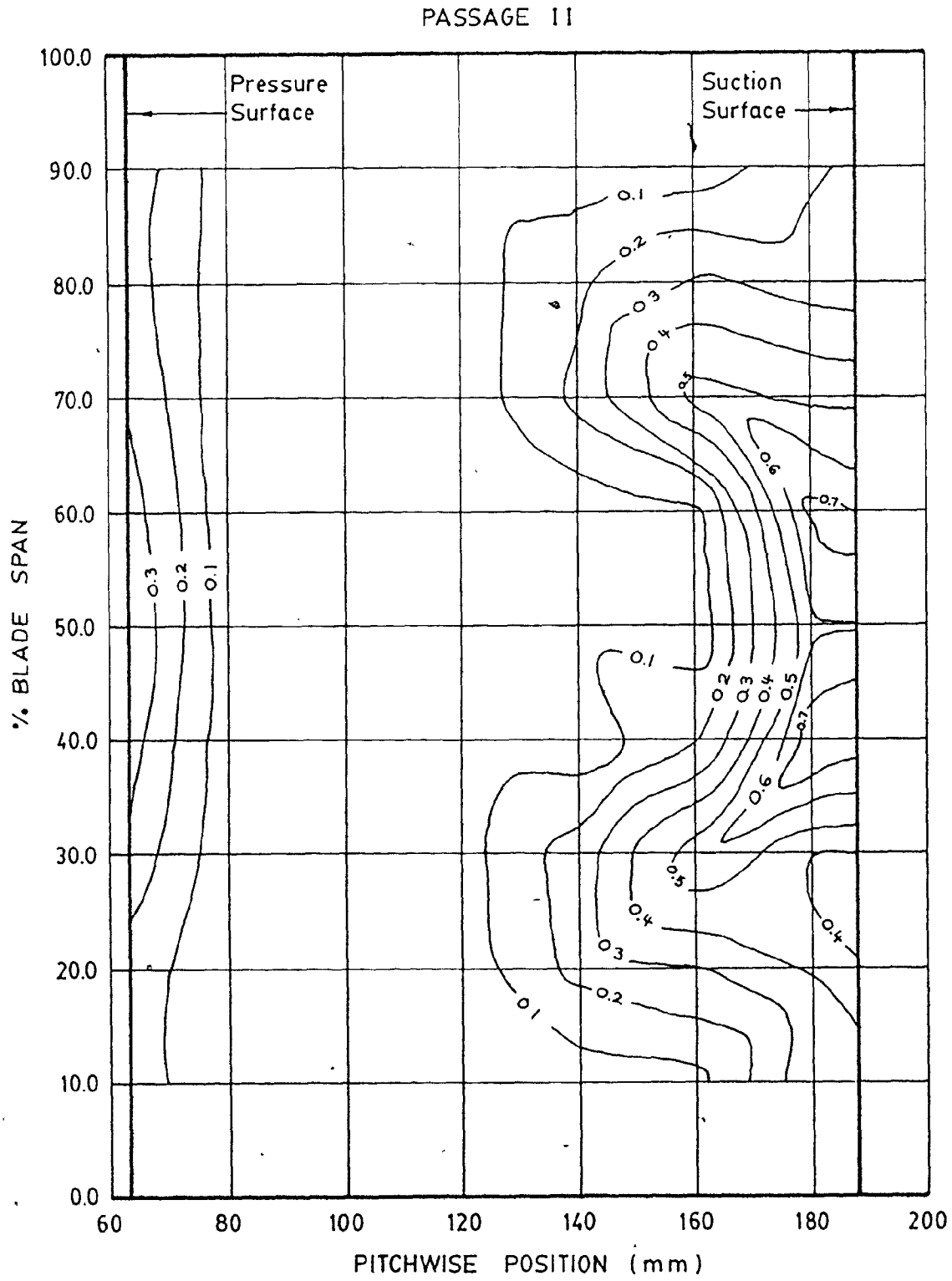

Figure 8.5 Distribution of the Local Total Pressure Loss Coefficient for Inlet Condition e) (Maximum Suction at Both Endwalls Corresponding to -26.65 mm (-10.1 inches) of water).

In Figure 8.1 there are two high loss cores (Cp_0 = 0.5) close and parallel to the projection of the blade suction surface at 32% and 65% blade span. These cores are thought to be associated with the secondary vortices formed by the roll up of the inner and outer endwall boundary layers over the blade suction surface. This sequence of events is shown pictorially in Figure 8.6. At 30% and 65% blade span, two higher loss peak zones (Cp_0 = 0.6) are observed. The loss pattern depicted in Figure 8.1 is relatively symmetric about mid-span due to the two-dimensional nature of the test rig. Another large loss core (Cp_0 = 0.5) occurs at 45% blade span. Its presence in the vicinity of the projection of the suction surface could be due to the merging of the two upstream endwall boundary layer fluids on the suction surface within the test passage.

Present in all the loss contour plots (Figures 8.1 through 8.5) are two low loss zones near the projection of the cascade endwalls. The zone near the inner endwall extends to approximately 20% blade span and the zone near the outer endwall extends from approximately 80% blade span. Both zones extend across the passage an estimated distance of 70% blade pitch measured from the projection of the blade suction surface and there are no indications of vortices within these zones. There is also a low loss passage close to and spanning the projection of the blade pressure surface which is common to all of the total

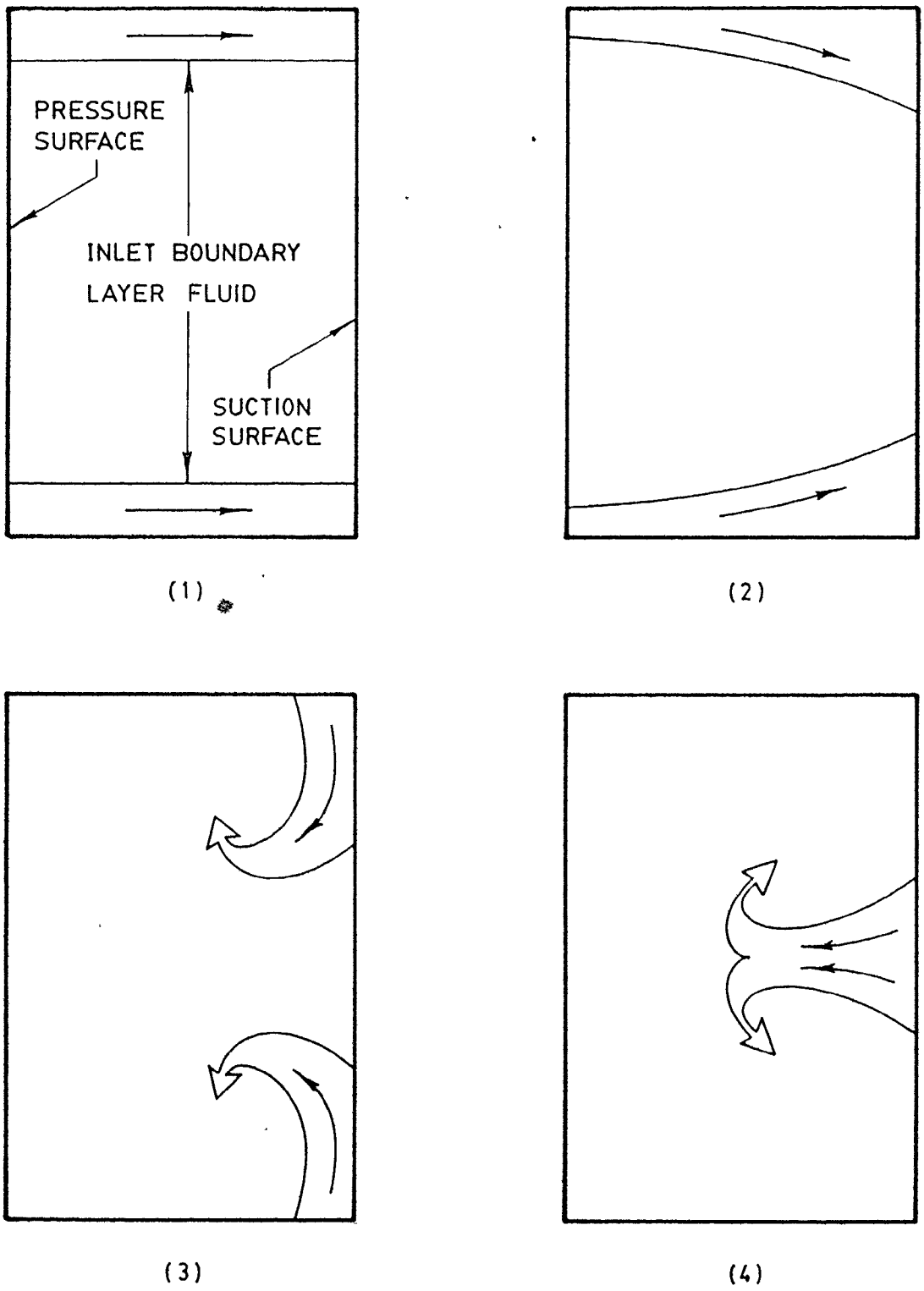

Figure 8.6 Formation of the 'Passage Vortex'.

loss contour plots.

Figure 8.2 exhibits the loss distribution with suction applied at the inner endwall. When compared with Figure 8.1, it can be seen that the removal of a portion of the inner endwall boundary layer fluid eliminates the loss peak zone at 30% blade span,however, the outer high loss peak zone is not greatly affected. The comparison also shows that the portion of the low loss spanwise passage nearer the inner endwall has broadened.

The results obtained when boundary layer suction was applied at the outer endwall are shown in Figure 8.3. The original high loss peak zone (Figure 8.1) at 65% blade span has now vanished and the high loss peak zone at 30% blade span has been somewhat reduced. Also, the low loss spanwise passage has broadened.

With boundary layer suction at both endwalls (Figure 8.4), the high loss peak zones at 30% and 65% blade span have disappeared entirely and a widening of the low loss spanwise passage is observed near mid-span. With a further increase in the boundary layer suction at both endwalls (Figure 8.5), the entire loss pattern again migrates towards the projection of the suction surface resulting in a further broadening of the low loss spanwise passage.

Similar trends, to the ones just described, were noticed in the tests carried out by Elshammaa {17} on the same blade profile in an annular cascade, however, the high

loss cores were positioned closer to the outer endwall. Also, the reduction in the inlet boundary layers did not shift the entire loss distribution towards the suction surface to the same extent observed in the present tests. The varying pitch/chord ratio, the orientation of the blades and the radial pressure gradients occurring in the annular test rig would all have a combined effect on the position of the vortex cores.

Came [5] tested a rectilinear cascade of 84.2^{o} deflection by varying the incidence and the inlet boundary layer displacement thickness. He presented his results in the form of total pressure loss contours and spanwise variations and pointed out that a single core of high loss was visible near the end of each blade. He also showed that when the upstream endwall boundary layer displacement thickness was increased, the relative loss peaks grew in size and migrated into the passage away from the blade suction surface.

Langston et al. [26] conducted similar tests on a planar cascade with 110^{o} of turning and obtained results similar to those of Came [5]. He took measurements at various axial locations within the passage and found that the loss cores near the endwalls climbed up the suction surface and increased in size with increased blade turning angle. The loss peaks at the cascade exit occurred at about 25% blade span (similar to the present tests).

Rectilinear cascade tests were also conducted by Woods [28] on 132° turning angle impulse type rotor blades. He varied the cascade aspect ratio by changing the blade span with a moveable endwall. His tests showed the presence of two high total pressure loss cores near the cascade endwalls. From his total pressure loss contours, Woods concluded that the secondary flow influenced the flow in the blade passage and the flow in the suction surface boundary layer. His tests showed that the mid-span loss coefficient increased with decreasing aspect ratio which he attributed to the effects of secondary flow. Woods also noted that the secondary flow had the effect of moving the loss peaks closer to mid-span as the blade height was reduced and consequently the size of the low loss zone near the endwalls increased.

In three-dimensional cascades, the radial pressure gradients move the low energy fluid along the blade span and cause the loss cores to be shifted even further into the passage. Rohlik et al. [10] showed, with the aid of an annular turbine nozzle blade cascade, how a portion of the outer wall boundary layer fluid was transported across the blade passage towards the suction surface and down the trailing edge where it was discharged near the inner annular wall. His results were presented in the form of loss contours and flow visualization photographs. Tests conducted on an annular cascade of 50° deflection nozzle guide vanes by Sjolander [29]

showed the formation and location of two high loss peaks located close to the blade suction surface at approximately 25% blade span (similar to the present tests). It is evident from the literature that the cascade type (rectilinear or annular) and geometry, as well as flow turning, have a significant effect on the magnitude and position of the high loss cores associated with the secondary flow.

8.3 Contour Plots of the Local Static Pressure Coefficient

The measured static pressure distributions corresponding to the selected inlet conditions a) through e) are shown in Figures 8.7 through 8.11, respectively. If the flow through the cascade was truly two-dimensional, then the Cp_s contours would be straight lines parallel to the blade surfaces and normal to the cascade endwalls. An examination of the present results shows that there are no significant changes in the measured static pressure near the projection of the blade suction surface. The zones of low pressure (highest Cp_s values) approximately coincide with the zones of high total pressure loss seen in Figures 8.1 through 8.5. Langston {26} presented an isobar plot of the static pressure coefficient in a plane within the cascade close to the exit plane. The closed isobars showed a low pressure zone away from the endwall and close to the suction surface. He stated that this pressure zone was the centre of the 'Passage Vortex'.

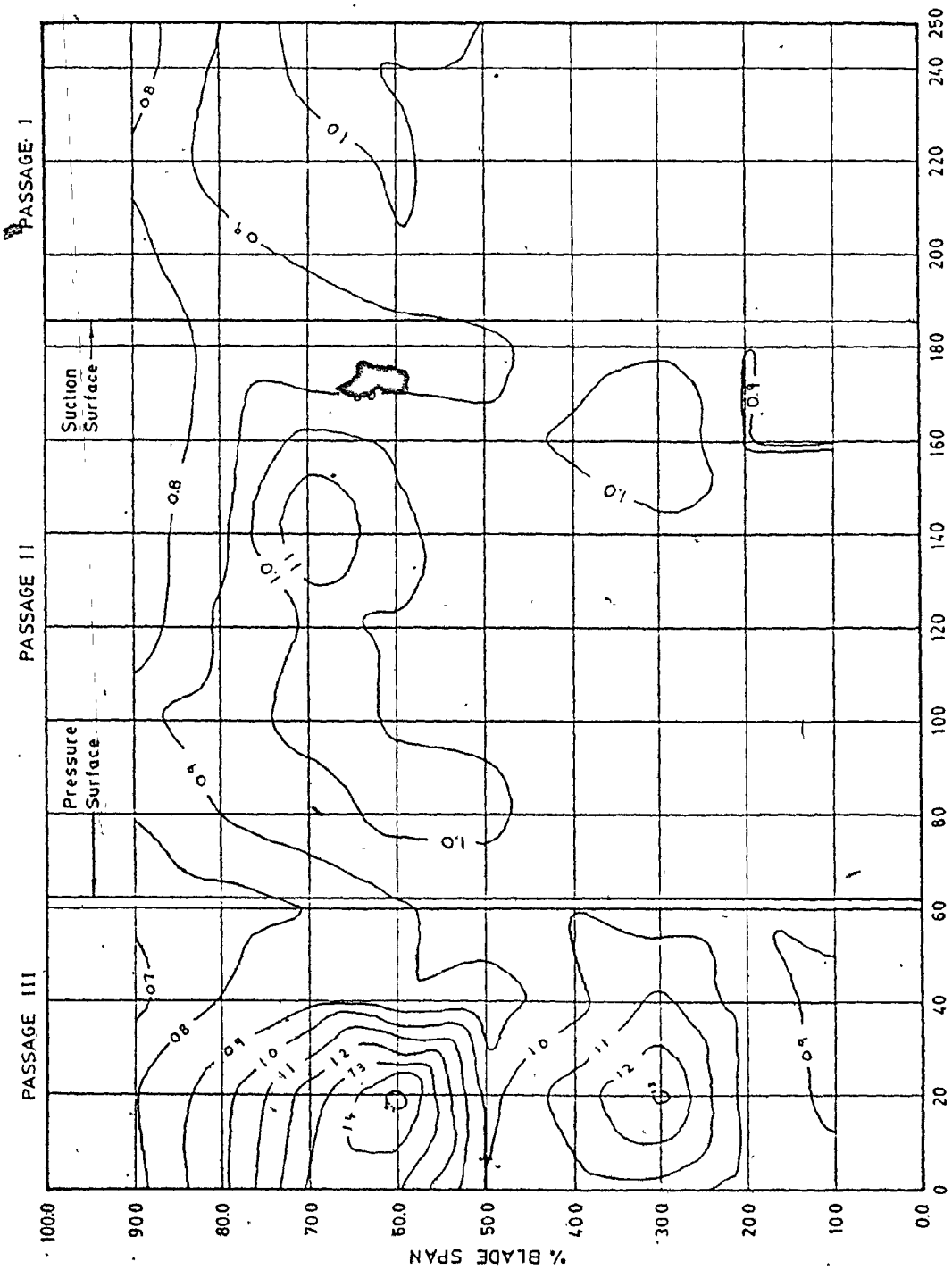

Figure 8.7 Distribution of the Local Static Pressure Coefficient for Inlet Condition a) (No Suction).

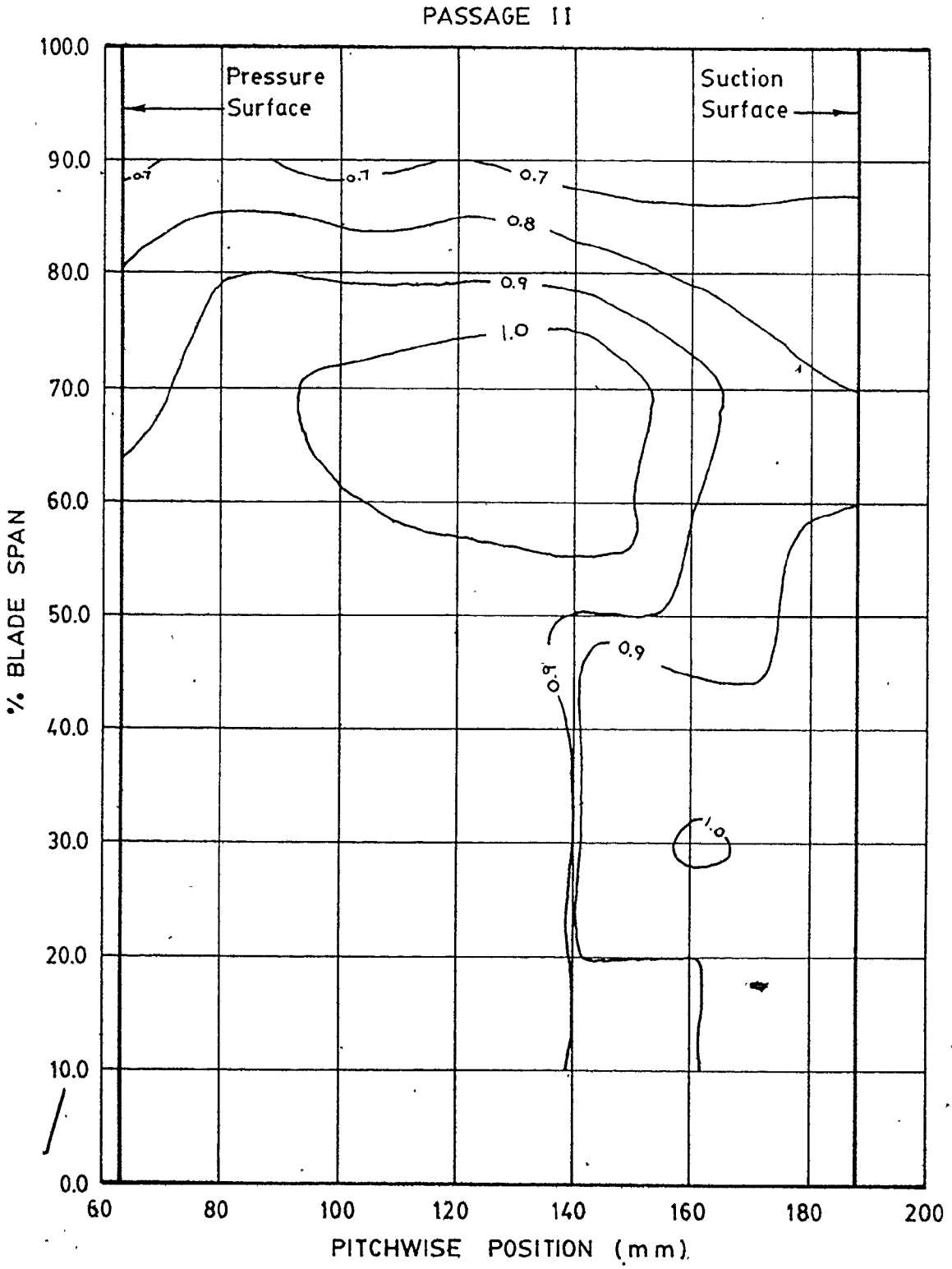

Figure 8.8 Distribution of the Local Static Pressure Coefficient for Inlet Condition b) (Suction at the Inner Endwall Corresponding to -11.68 mm (-4.6 inches) of water).

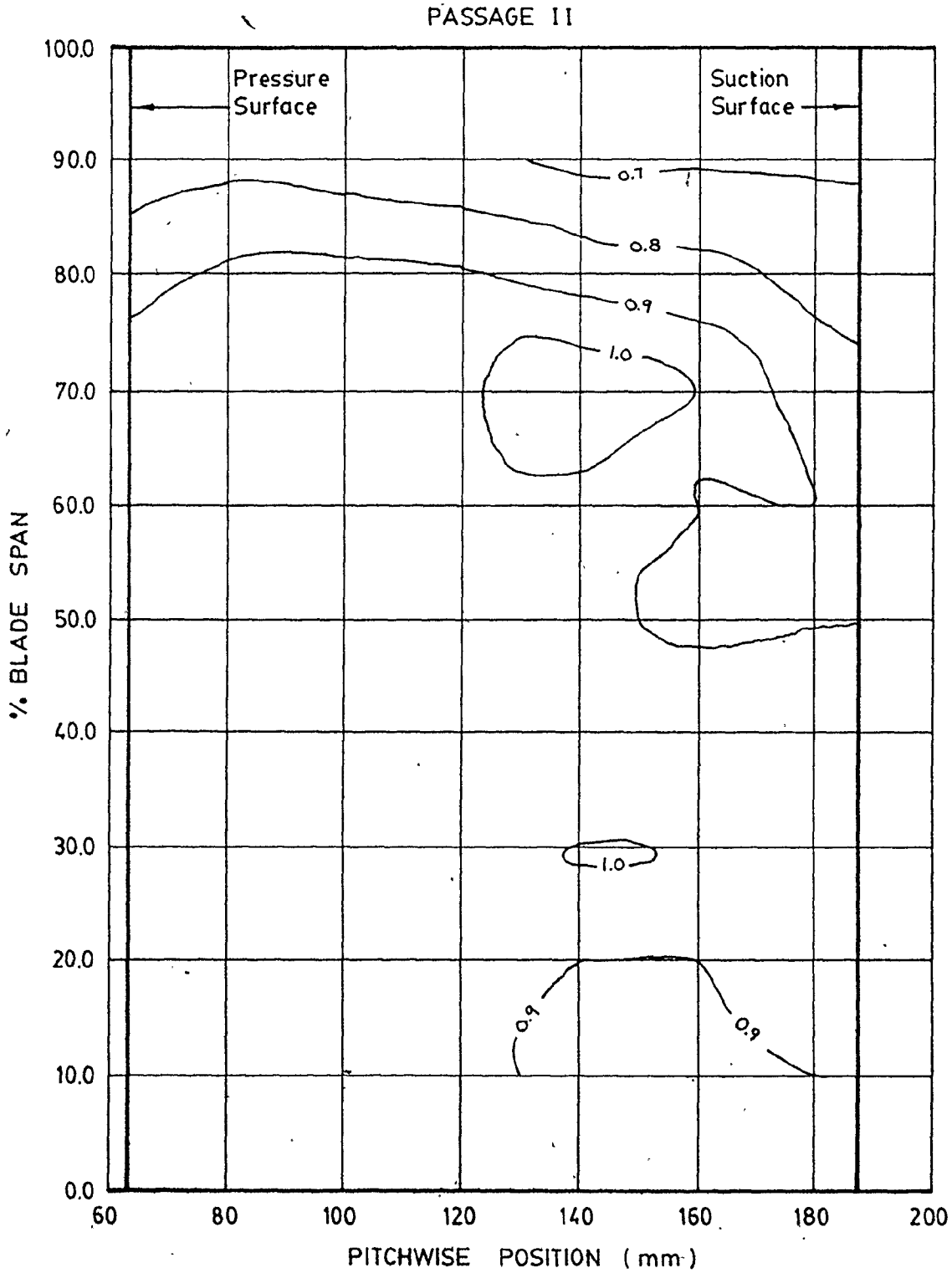

Figure 8.9 Distribution of the Local Static Pressure Coefficient for Inlet Condition c) (Suction at the Outer Endwall Corresponding to -11.68 mm (-4.6 inches) of water).

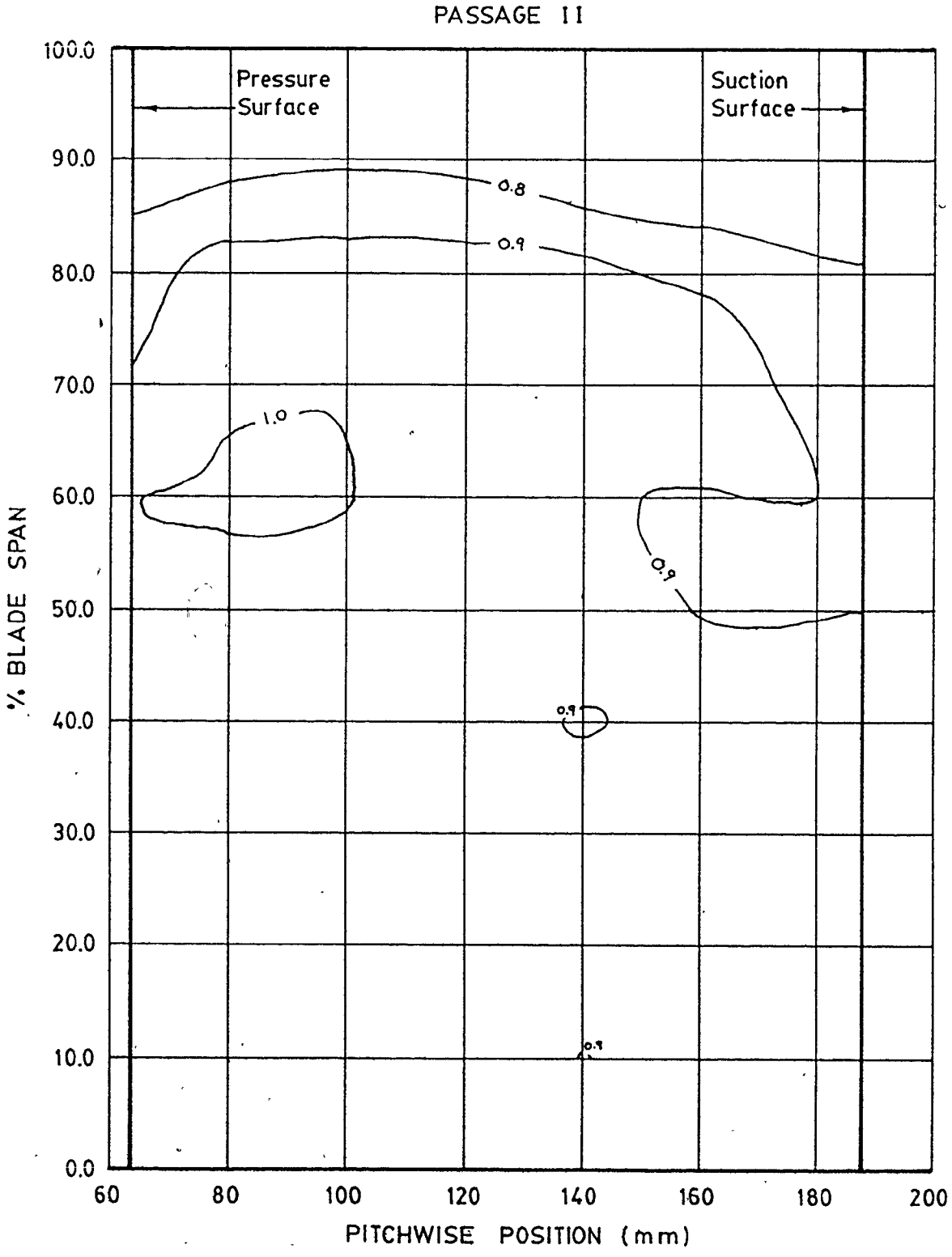

Figure 8.10 Distribution of the Local Static Pressure Coefficient for Inlet Condition d)(Suction at Both Endwalls Corresponding to -11.68 mm (-4.6 inches) of water).

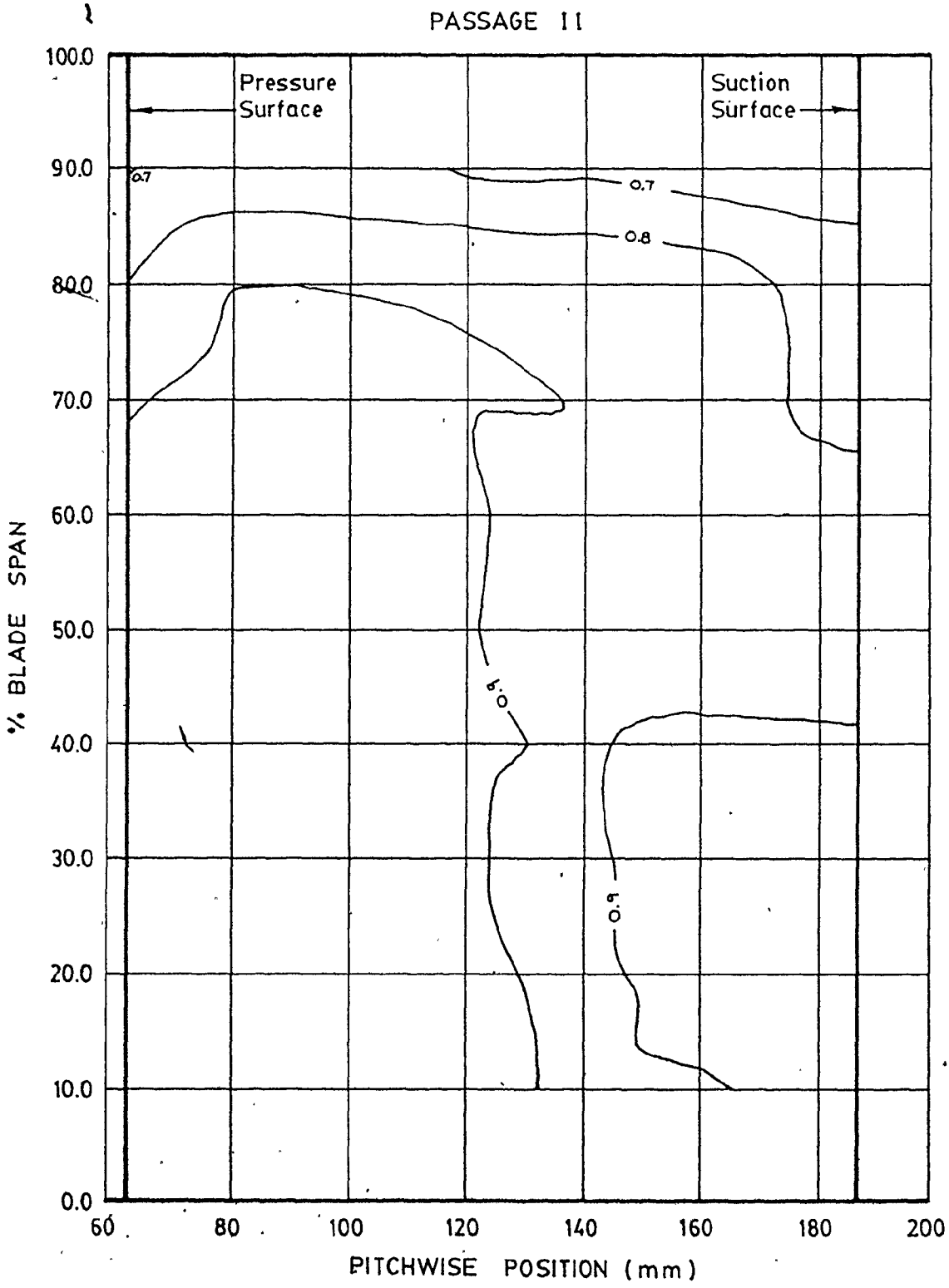

Figure 8.11 Distribution of the Local Static Pressure Coefficient for Inlet Condition e) (Maximum Suction at Both Endwalls Corresponding to -26.65 mm (-10.1 inches) of water).

8.4 Spanwise Variation of the Pitchwise Averaged Flow Parameters

With the hope of achieving a better appreciation of the effects of the secondary flow on the exit flow parameters, it was decided to plot the pitchwise mass averaged total pressure loss coefficient (Cp_{0m}), the deviation ($\Delta\alpha_2$), and the dimensionless axial velocity (Va/VI) in 10% increments of the blade span. The local values of Cp_0, $\Delta\alpha_2$, and Va are all functions of a spanwise and a pitchwise position. The pitchwise mass averaged values have, therefore, been defined as follows:

$$Cp_{0m} = \frac{\sum_0^S Cp_0 (V\cos\alpha\cos\theta)}{\sum_0^S (V\cos\alpha\cos\theta)} = \frac{\sum_0^S Cp_0 \, Va}{\sum_0^S Va} \qquad (8.3)$$

$$\Delta\alpha_2 = \frac{\sum_0^S \Delta\alpha_2 \, Va}{\sum_0^S Va} \qquad (8.4)$$

$$\frac{Va}{VI} = \frac{\sum_0^S Va}{nVI} \qquad (8.5)$$

where

$V\cos\alpha\cos\theta$ = Va and n is the number of pitchwise measurements at a specific spanwise location.

The mass averaged values for the inlet conditions a) through e) are presented in Figures 8.12 through 8.16 respectively. An examination of the spanwise variation of Cp_{0_m} shows that the high loss peaks correspond to the location of the secondary vortices. A reduction in the end wall boundary layer displacement thickness shifts the corresponding portion of the curve towards the ordinate, thereby, showing a decrease in the total pressure loss. Woods {28} presented the total pressure loss coefficients in a similar manner. His results also showed the presence of two high loss peaks, one on either side of the blade mid-span. As mentioned earlier in this chapter, Woods' {28} spanwise loss distributions showed that the mid-span loss coefficient increased with decreasing aspect ratios.

Distributions presented by Came { 5 }, showed that the high loss peaks grew and migrated towards the blade mid-span when the flow turning and upstream endwall boundary layer displacement thickness were increased.

The spanwise distributions of $\Delta\alpha_2$ show overturning ($\Delta\alpha_2$ negative) near the endwalls and underturning ($\Delta\alpha_2$ positive) at two locations on either side of the blade mid-span. The overturning and underturning can be associated with the direction of the 'Passage Vortex' (shown in Figure 2.1). A reduction in the endwall boundary layer is shown to reduce the overall deviation. The maximum underturning was found to be approximately 8^{o} compared to 18^{o} in Elshammaa's {17}

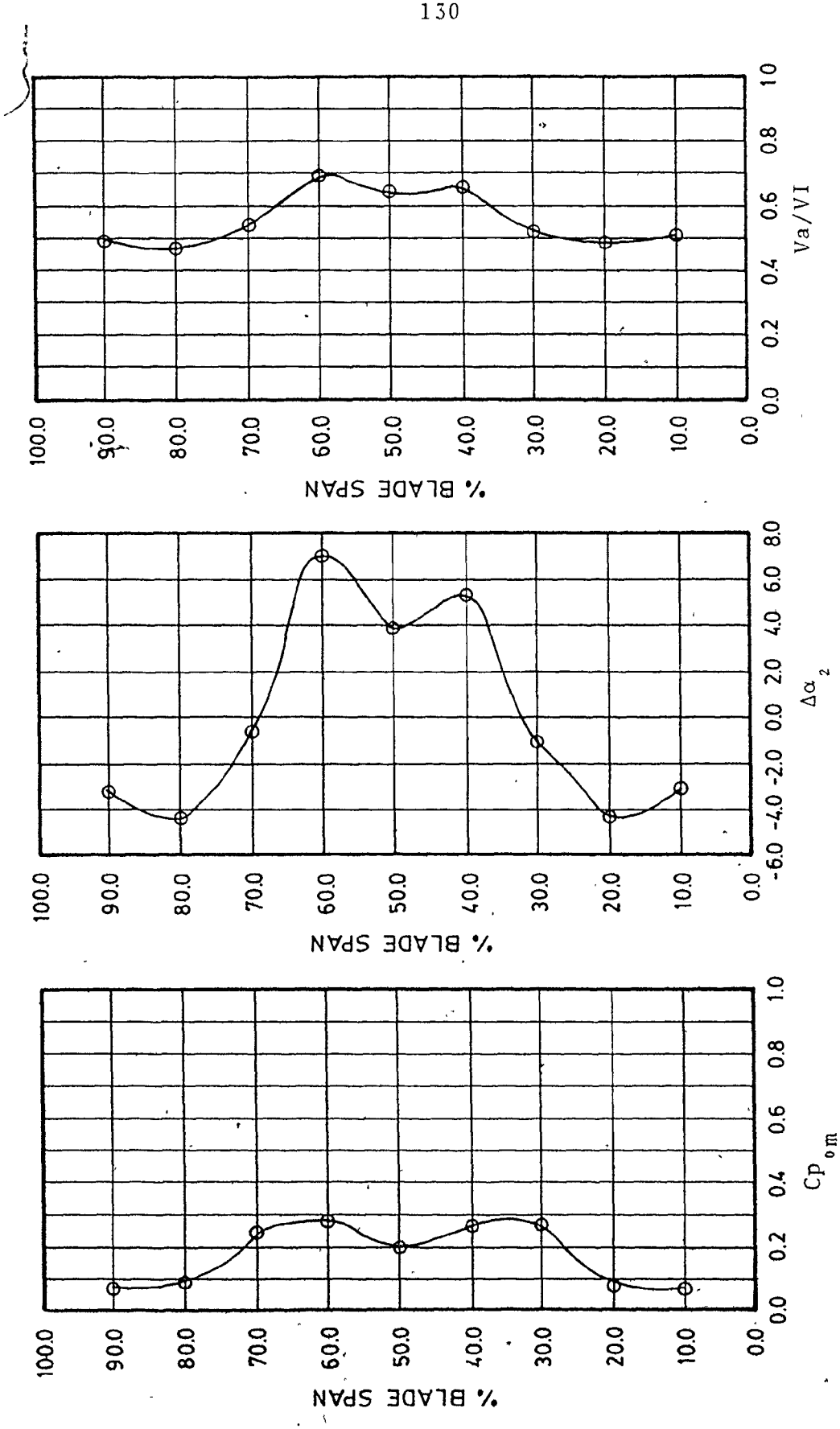

Figure 8.12 Spanwise Distribution of Pitchwise Averaged Flow Parameters for Inlet Condition a) (No Suction).

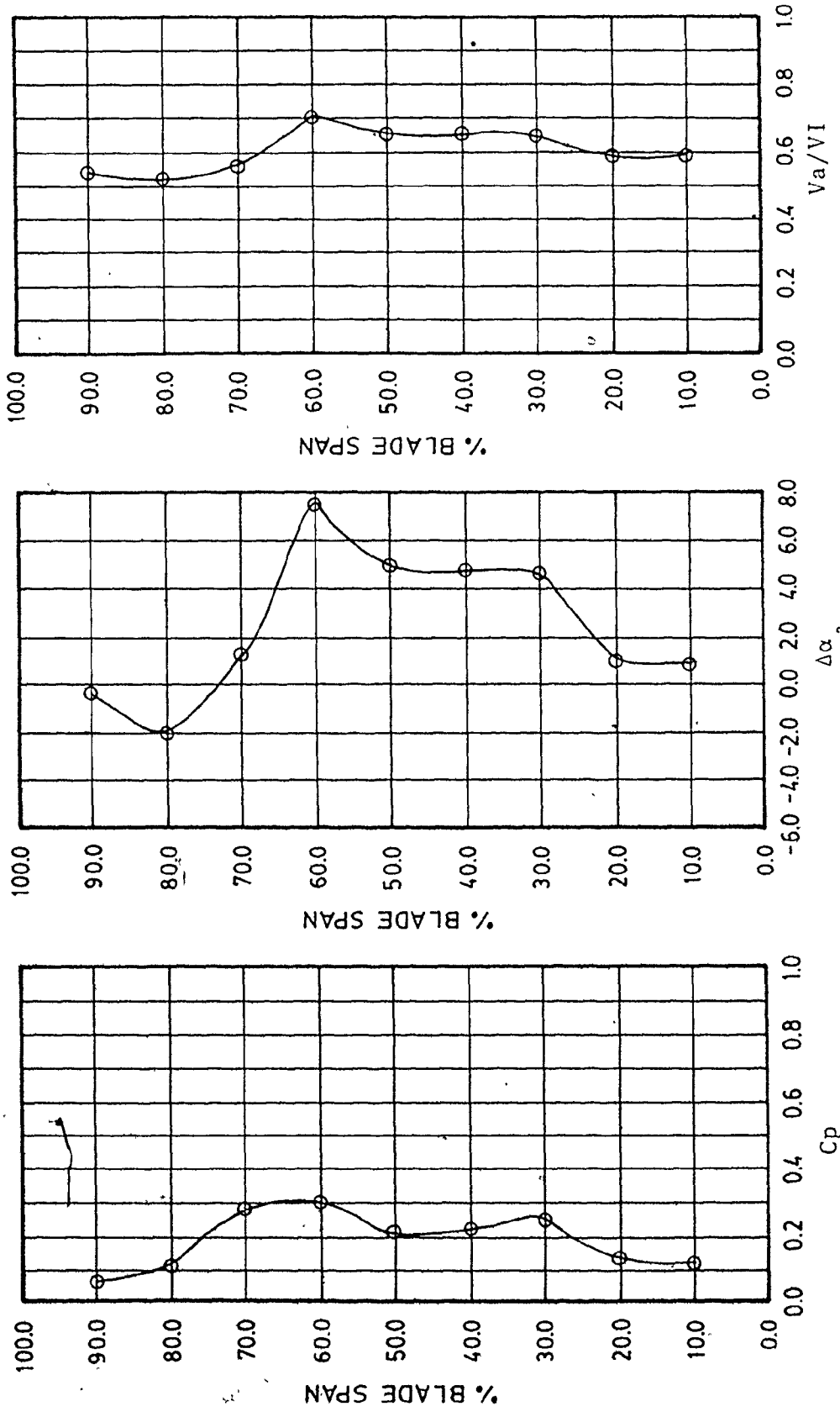

Figure 8.13 Spanwise Distribution of Pitchwise Averaged Flow Parameters for Inlet Condition b) (Suction at the Inner Endwall Corresponding to -11.68 mm (-4.6 inches) of water).

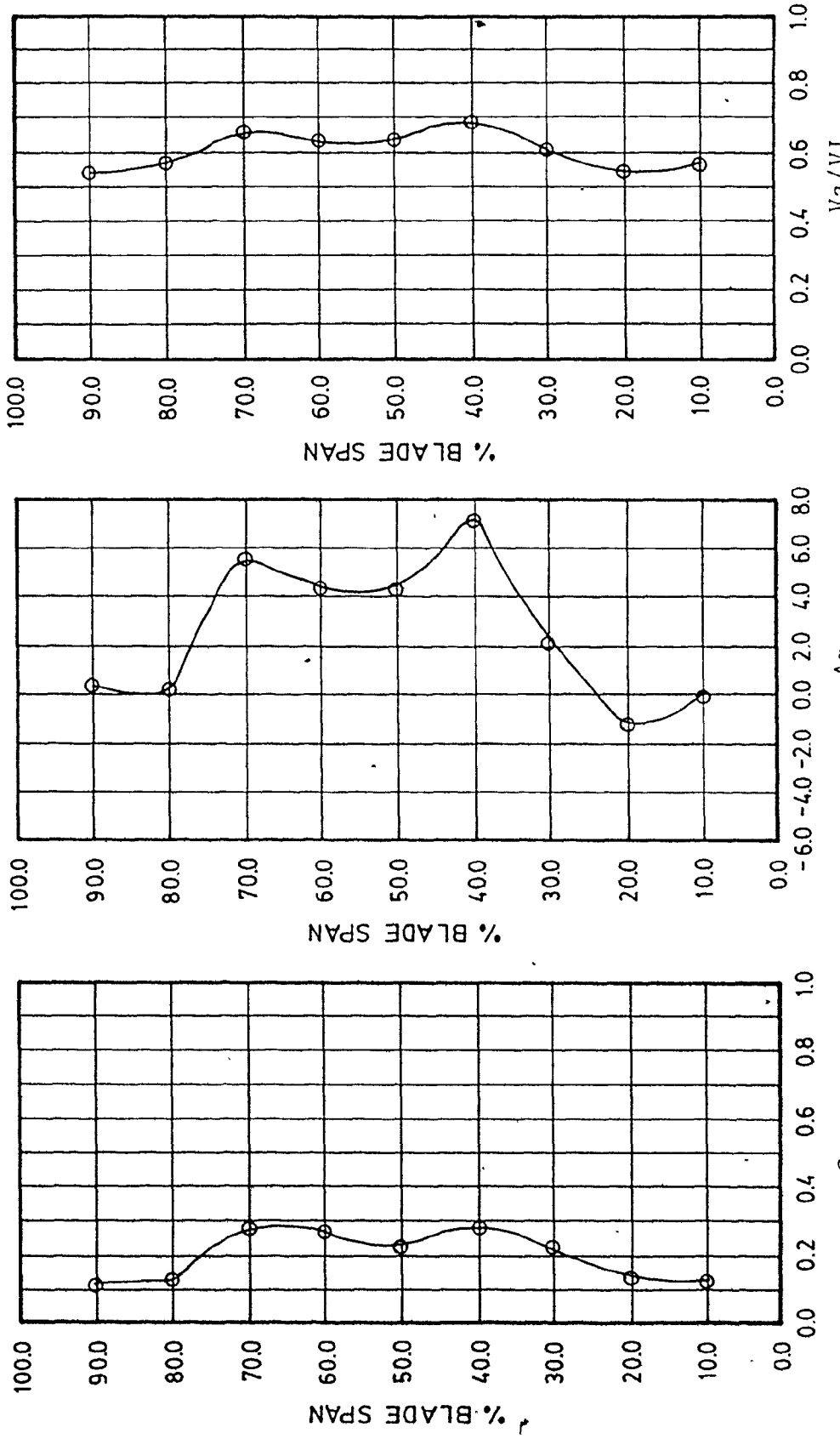

Figure 8.14 Spanwise Distribution of Pitchwise Averaged Flow Parameters for Inlet Condition c) (Suction at the Outer Endwall Corresponding to -11.68 mm (-4.6 inches) of water).

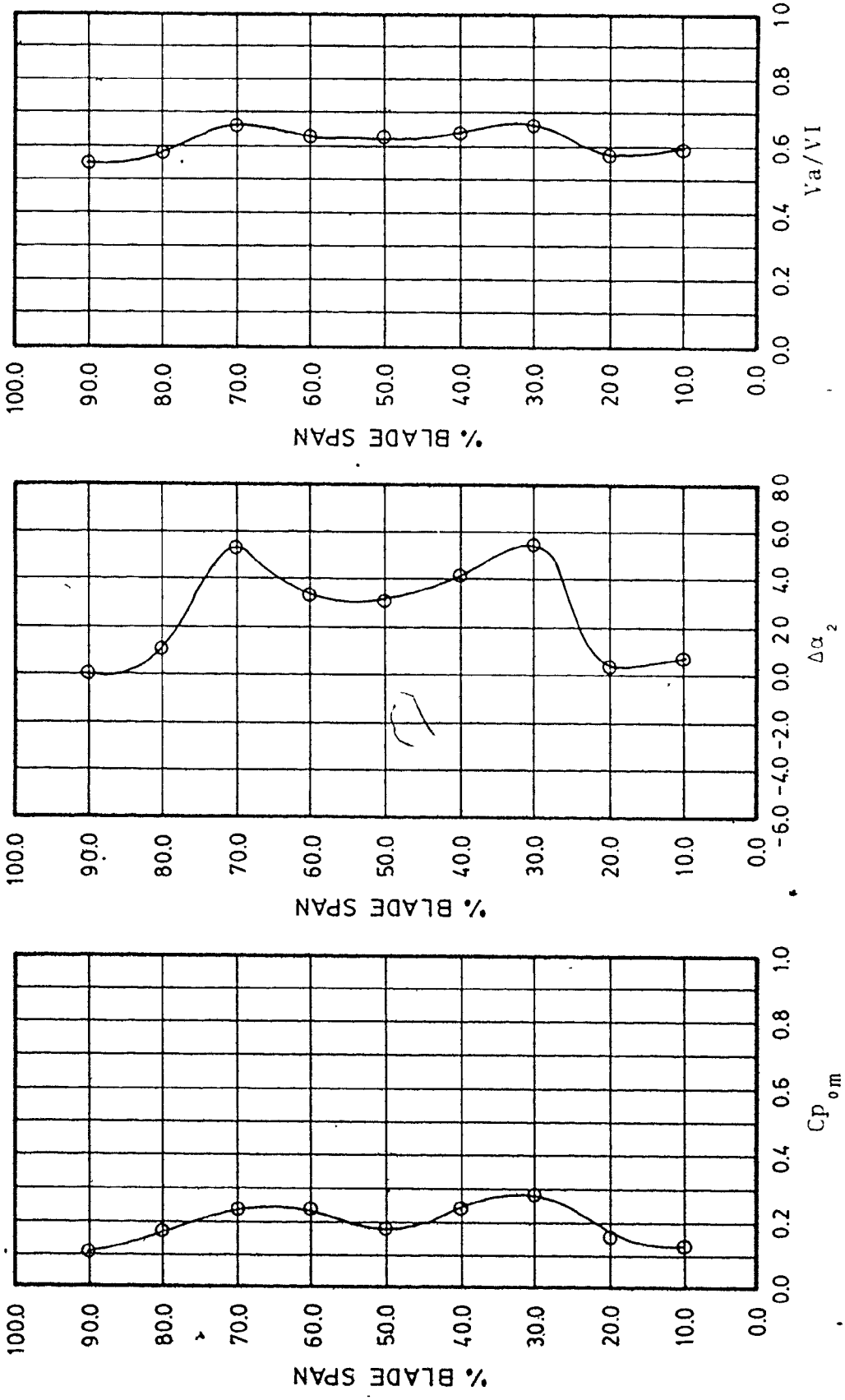

Figure 8.15 Spanwise Distribution of Pitchwise Averaged Flow Parameters for Inlet Condition d) (Suction at Both Endwalls Corresponding to -11.68 mm (-4.6 inches) of water).

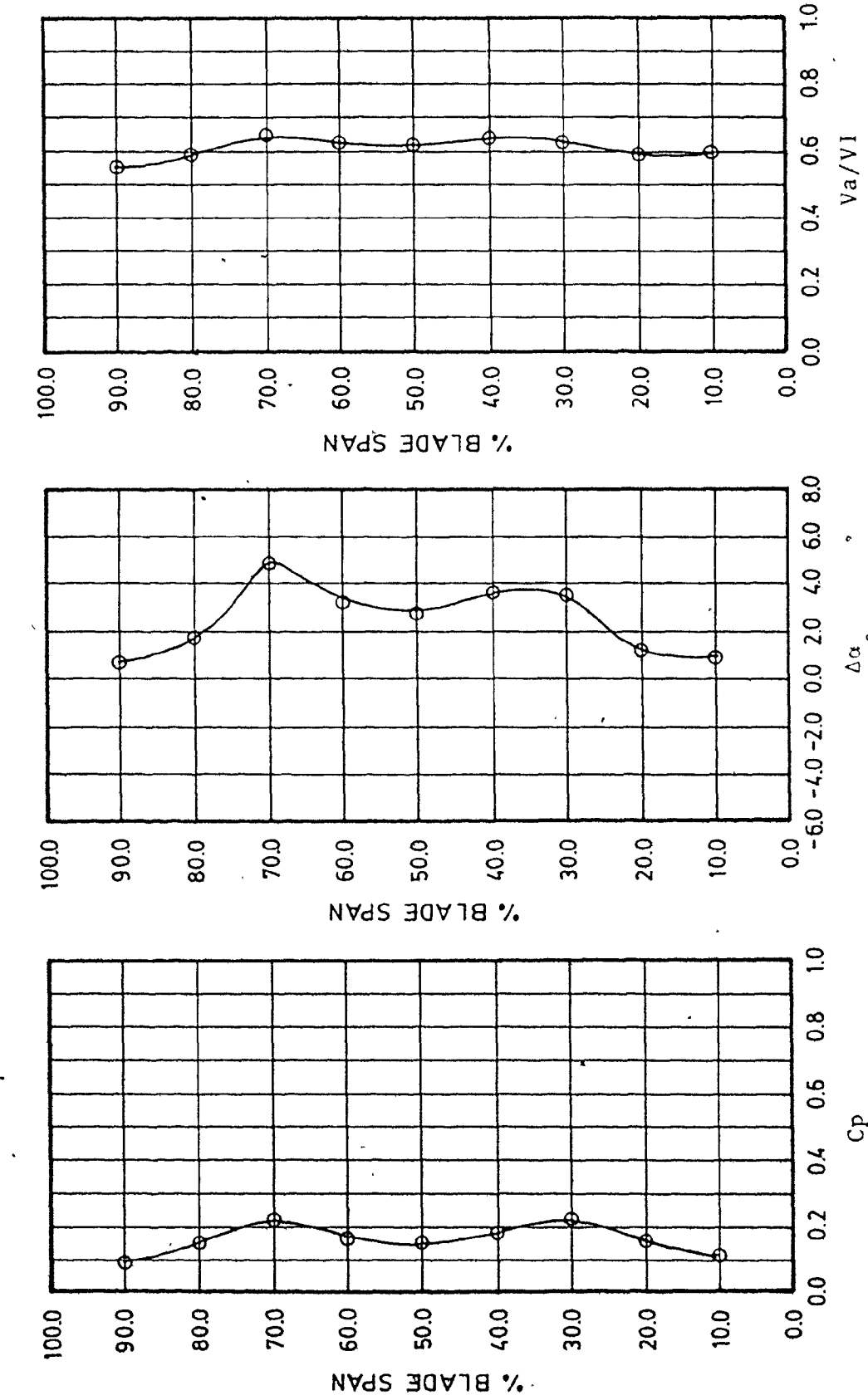

Figure 8.16 Spanwise Distribution of Pitchwise Averaged Flow Parameters for Inlet Condition e) (Maximum Suction at Both Endwalls Corresponding to -26.65 mm (-10.1 inches) of water).

tests on the same profile. A review of the literature showed that the underturning increased with increasing flow deflections. In the present tests, the areas of high underturning are shown to have higher axial velocities.

8.5 Cascade Losses and Comparison with Correlations

In order to compare the cascade secondary losses with the existing reported losses and correlations, it was necessary to compute the overall total loss coefficient and the secondary loss coefficient. The overall blade loss coefficient mass averaged in the pitch and span directions is defined as follows {5}:

$$Y_T = \frac{\Delta P_T}{P_{02m} - P_{2m}} \tag{8.6}$$

where

$$\Delta P_T = \frac{\sum_{0}^{H} \sum_{0}^{S} (V\cos\alpha\cos\theta)\Delta P_0}{\sum_{0}^{H} \sum_{0}^{S} (V\cos\alpha\cos\theta)}$$

ΔP_0 = local total pressure loss = $P_{01} - P_{02}$

P_{02m} = mass averaged exit total pressure = $P_{01} - \Delta P_T$

P_{2m} = mass averaged exit static pressure = $P_1 - \Delta P_S$

and

$$\Delta P_s = \frac{\sum_{0}^{H}\sum_{0}^{S} (V\cos\alpha\cos\theta)\Delta P}{\sum_{0}^{H}\sum_{0}^{S} (V\cos\alpha\cos\theta)}$$

ΔP = local static pressure loss = $P_1 - P_2$.

The plots of the spanwise distribution of the pitchwise averaged losses showed that it was impossible to distinguish the profile loss from the total loss. In order to measure the profile losses, it would be necessary to make detailed measurements of the boundary layer growth and the velocity distributions along the blade surfaces. Since the test rig's construction did not facilitate these measurements, it was necessary to estimate the profile losses from existing correlations. As pointed out in Chapter 2, a survey conducted by Denton [6] showed that none of the existing profile loss correlations could accurately predict the losses. For the purpose of this study, however, it was decided to make an estimate of the profile losses by using some of the correlations more commonly used in design. Therefore, the secondary loss coefficient can be obtained by subtracting this estimated profile loss from the measured overall total loss, i.e.

$$Y_s = Y_T - Y_P \qquad (8.7)$$

The loss coefficients, calculated from existing correlations, are summarized and compared with those

measured at the cascade exit measuring station A (for inlet conditions a) through e)) in Table 8.1.

In general, the measured total and secondary losses in Table 8.1 are much lower than those predicted by the correlations. The annular rig total loss coefficients presented by Elshammaa {17} are twice as high as the present measured values for the two-dimensional test rig.

The flow (under inlet condition a)) was traversed in the plane of exit measuring station B (located at a streamwise distance of 1.5C from the cascade exit) and the measured losses increased by approximately 47%. This trend has been reported in the literature and has been attributed to the effects of flow mixing. Came {5} conducted preliminary tests to establish the influence of the exit measuring station on the measured losses. His experiments covered a range of 0.5C to 2.0C. He reported that the profile and secondary losses showed a rising trend up to 1.2C and then become constant. All of his subsequent tests were performed at a downstream streamwise distance of 1.35C. Langston {26} measured the losses at various streamwise distances from the cascade exit plane and found that the total pressure loss showed an increase of almost 28% over a streamwise distance between 0.2C and 0.75C.

Figure 8.17 shows the variation in the secondary loss parameter (corrected for the effects of aspect ratio and aerodynamic loading as suggested by Dunham {7}) with

Table 8.1

A Comparison of the Calculated and Measured Cascade Losses

Calculated Loss Coefficients from Existing Correlations

Profile Loss Coefficient	Secondary Loss Coefficient	Total Loss Coefficient
Y_p = 0.095 (Ainley & Mathieson {13})	Y_s = 0.344 (Ainley & Mathieson {13})	Y_T = 0.439 (Ainley & Mathieson {13})
Y_p = 0.082 (Hawthorne {30})	Y_s = 0.188 (Dunham {7})	Y_T = 0.138 (Hawthorne {30})
Y_p = 0.044 (Baljé {3})	Y_s = 0.475 (Dunham & Came {21})	Y_T = 0.229 (Soderberg {18})
Y_p = 0.05 (Denton {6})	Y_s = 0.081 (Horlock {18})	

Measured Loss Coefficients for Inlet Conditions a) through e)

Inlet Condition	a)	b)	c)	d)	e)
Y_T	0.105	0.113	0.119	0.114	0.097
Y_s (based on Ainley & Mathieson's Y_p)	0.010	0.018	0.024	0.019	0.002
Y_s (based on Hawthorne's Y_p)	0.023	0.031	0.037	0.032	0.015
Y_s (based on Baljé's Y_p)	0.061	0.069	0.075	0.070	0.053
Y_s (based on Denton's Y_p)	0.055	0.063	0.069	0.064	0.047

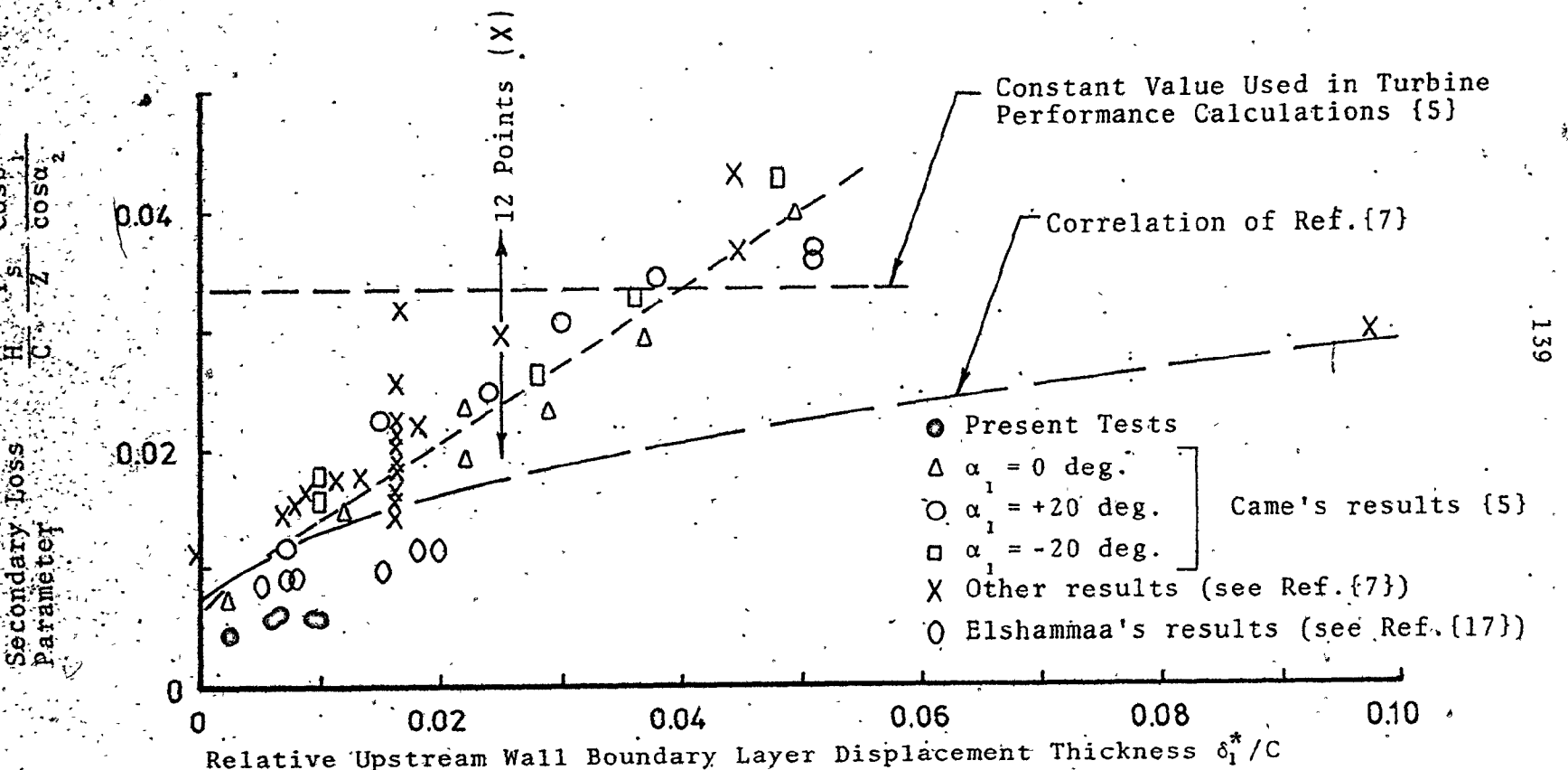

Figure 8.17 Variation of Gross Secondary Loss with the Inlet Displacement Thickness.

the relative upstream boundary layer displacement thickness (δ_1^*/C). In the secondary loss parameter, the blade loading parameter is defined as follows:

$$Z = \left(\frac{C_L}{S/C}\right)^2 \frac{\cos^2\alpha_2}{\cos^3\alpha_m} \qquad (8.8)$$

where

C_L = lift coefficient = $2\frac{S}{C}(\tan\alpha_1 - \tan\alpha_2)\cos\alpha_m$

α_m = mean gas angle = $\tan^{-1}\frac{1}{2}(\tan\alpha_1 + \tan\alpha_2)$.

The correlations of Dunham {7} and Came {5} and the constant value used in turbine performance calculations {5} are presented in Figure 8.17. It can be seen that the results of other investigations have considerable scatter because in many of the cases {5} Y_s had to be calculated and δ_1^*/C was based on a 1/7 power law inlet boundary layer profile. Came {5} pointed out that the values of δ_1^*/C in turbines are usually within the lower half of the range shown on the abscissa and in this same part of the graph, the cascade loss is much less than the indicated loss level in a turbine at similar values of δ_1^*/C.

In the present tests, the secondary loss coefficient was based on Baljé's {3} Y_p correlation which gave the highest estimate of the secondary loss coefficient and hence the highest secondary loss parameter. Also, the dimensionless displacement thickness (δ_1^*/C) was based upon an average of the

two values at the inlet endwalls. The annular results of Elshammaa [17] (Figure 8.17) show a trend similar to the present results. In general, it can be said that the measured secondary losses are much lower than those predicted by existing correlations.

CHAPTER 9

CONCLUSIONS AND RECOMMENDATIONS FOR FURTHER STUDIES

A large scale two-dimensional cascade test rig was constructed to investigate the secondary flow phenomenon occurring in turbine blade passages with high turning. Extensive tests at a Reynolds number = 3.68×10^5 (based on the blade chord) were conducted which included the measurement of the flow parameters at the bellmouth throat, within the blade test passage and at the cascade inlet and exit measuring stations. The analysis of the test results obtained at these various locations has led to the following general conclusions:

a) The bellmouth intake did an excellent job in accelerating the inlet flow to a velocity that had a uniform profile at the throat. Reasonable periodicity was established by tailoring the appropriate inlet flow conditions with facilities provided in the rig design.

b) It was possible to effectively control the inlet endwall boundary layer displacement thicknesses within a portion of the range of interest to the turbine designer.

c) Although the Reynolds number was within the range reported in the literature, the measured turbulence intensities were considerably lower than those encountered

in the actual engine or in previous cascade data.

d) The pressure distributions on the cascade endwalls, within the test passage, showed a gradient almost parallel to the pitchwise direction and a low pressure region shifted slightly from the blade suction surface. These phenomena were respectively attributed to the cross-channel migration of the endwall boundary layers and their subsequent roll up on the suction surface to form the 'Passage Vortices'. Reasonable agreement was found between the measured and theoretical pressure distributions on the blade pressure surface. Differences were noticed on the blade suction surface due to the roll up of the endwall boundary layers.

e) An examination of the total pressure loss contours at the exit measuring station showed that high loss cores (with enclosed loss peaks) existed on either side of the blade mid-span. Two low loss zones were recognized near the cascade endwalls. The removal of a portion of the endwall boundary layers had the effect of reducing and even eliminating the high loss cores and peaks. The static pressure contours generally supported the expected locations of the vortex cores.

f) The plots of the spanwise variations revealed zones of high overturning near the cascade endwalls and high underturning in a zone near the blade mid-span. These extremes were reduced with reductions in the endwall boundary

layer displacement thicknesses.

g) The cascade profile losses were not readily measurable and, therefore, had to be estimated with existing correlations.

h) The measured total pressure loss at exit measuring station B was 47% higher than that measured at exit measuring station A, due to the effects of flow mixing.

i) The secondary flow effects do not vividly show up in the measured total pressure loss coefficients but rather are more important with respect to the exit flow angles, as exhibited in the plots of the spanwise variations. Turner {27}and Woods {28} also showed this trend in their test results.

j) The three-dimensional results of Elshammaa {17} (for the same blade profile) showed that the measured total and secondary loss coefficients are higher than the values measured in the present tests. The loss cores in the present two-dimensional rig are not as close to the blade mid-span as those in Elshammaa's annular rig. The annular rig, due to the varying pitch/chord ratio, had spanwise pressure gradients which moved the low energy fluid along the span, causing the loss cores to be shifted further into the passage.

k) A comparison of the measured overall total pressure and secondary loss coefficients with those calculated from existing correlations showed that the correlations overestimate the losses.

Suggestions for Future Studies

a) The effect of flow incidence on the measured losses could be studied by varying the position of the inlet channel sidewalls.

b) The turbulence intensity at the inlet measuring station could be increased to a more representative value by installing screens at the throat of the bellmouth intake.

c) A direct measurement of the profile losses could be taken at mid-span, if the test rig blade span were increased to some suitable amount. This would prevent the vortex cores (due to the roll up of the endwall boundary layers) from merging within the passages.

d) The effect of larger endwall boundary layer displacement thicknesses on the secondary loss parameter could be investigated by tripping the boundary layer or by testing with injection instead of suction.

e) It would be possible to study the effect of the blade aspect ratio (H/C) on the position and strength of the secondary vortices by using a movable endwall to change the span length. The effects of a variable pitch/chord ratio (S/C) could also be studied.

f) Taking extensive flow measurements within the blade passage would give a complete picture of the total loss distribution.

g) A blade passage surface flow visualization could be conducted to identify possible separation zones associated with the secondary flow phenomenon.

BIBLIOGRAPHY

1. Malhotra, R.K., "The Two-Dimensional Development and Analysis of Blade Profiles Having Large Turning Angles", M. Eng. Thesis, Mech. Eng. Dept., McMaster University, March 1971.

2. Stannard, J. H., "The Aerodynamic Design and Testing of High Turning Angle Turbine Blades", Ph.D. Thesis, Mech. Eng. Dept., McMaster University, April 1975.

3. Baljé, O. E. and Binsley, R.L., "Axial Turbine Performance Evaluation", Jour. of Eng. Power, Trans. ASME, October 1968, pp. 341-348.

4. Ainley, D.G. and Mathieson, G.C.R., "An Examination of the Flow and Pressure Losses in Blade Rows of Axial-Flow Turbines", N.G.T.E., Report R.86, 1951.

5. Came, P. M., "Secondary Loss Measurements in a Cascade of Turbine Blades", I.Mech. Eng. Conference Publication, 3, 1973, p. 75.

6. Denton, J. D., "A Survey and Comparison of Methods for Predicting the Profile Loss of Turbine Blades", I. Mech. Eng., Conference Publication, 3, 1973, p.204.

7. Dunham, J., "A Review of Cascade Data on Secondary Losses in Turbines", J. of Mech. Eng. Sci., Vol. 12, No. 1, 1970, p. 48.

8. Lakshminarayana, B. and Horlock, J. H., "Review: Secondary Flows and Losses in Cascades and Axial Flow Turbomachines", Int. J. Mech. Sci., 5, 1963, p. 287.

9. Louis, J. F., "Secondary Flow and Losses in a Compressor Cascade", British ARC, R & M 3136, 1958.

10. Rohlik, H. E., Kofskey, M. G., Allen, H. W., and Herzig, H.Z., "Secondary Flows and Boundary Layer Accummulations in Turbine Nozzles", NACA Report 1168, 1954.

11. Horlock, J. H., and Lakshminarayana, B., "Secondary Flow: Theory, Experiments and Applications in Turbomachinery Aerodynamics", Annual Review of Fluid Mechanics, Vol. 5, 1973, p. 247.

12. Smith, H. B., "Secondary Flow in Axial Flow Turbomachinery", Trans. ASME, 77, October 1955, p. 1065.

13. Ainley, D.G., and Mathieson, G.C.R., "A Method of Performance Estimation for Axial Flow Turbines", Aeronatical Research Council, R & M 2974, 1957.

14. Baljé, O.E., "Axial Cascade Technology and Application to Flow Path Designs. Part I --Axial Cascade Technology", J. of Eng. for Power, Aug. 1967, p. 1.

15. Olson, R.M., "Essentials of Engineering Fluid Mechanics", Harper and Row, New York, 1981.

16. Herzig, H.Z. and Hansen, A.G., "Visualization Studies of Secondary Flows with Applications to Turbomachines", Trans. ASME, 77, 1955, p. 249.

17. Elshammaa, S. A., "The Effect of the Inlet Boundary Layer On The Secondary Flow in an Annular Cascade", Ph. D. Thesis. Mech.Eng. Dept., McMaster University, Oct. 1978.

18. Horlock, J. H., "Axial Flow Turbines, Fluid Mechanics and Thermodynamics", Robert E. Krieger Publishing Company, New York. 1973.

19. Cohen, H., Rogers, G.F.C., and Saravanamuttoo, H.I.H., "Gas Turbine Theory", Longman, 1979.

20. Horlock, J.H., Shaw, R., Pollard,D., and Lewkowicz, A., "Reynolds Number Effects in Cascades and Axial Flow Compressors", J. of Eng.for Power, July 1964, p. 236.

21. Dunham, J., and Came, P. M., "Improvements to the Ainley-Mathieson Method of Turbine Performance Prediction", Trans. ASME, Jour. of Eng. for Power, July 1970, p. 252.

22. Moustapha, S.H., "Secondary Flow In An Annular Cascade of High Turning Angle Turbine Blades", Ph.D. Thesis, Mech. Eng. Dept., McMaster University, March 1978.

23. Smith, R.H. and Wang, C., "Contracting Cones Giving Uniform Throat Speeds", J. of Aero. Sci., Oct. 1944, p. 356.

24. Harris, T.C.M., "The Aerodynamic Performance Of A High Turning Angle Turbine Blade Profile", M. Eng. Thesis, Mech. Eng. Dept.,McMaster University, Aug. 1977.

25. Holman, J. P., "Experimental Methods for Engineers", McGraw-Hill Book Company, New York, 1978.

26. Langston, L. S., Nice, M. L., and Hooper, R. M., "Three-Dimensional Flow Within a Turbine Cascade Passage", Jour. of Eng. for Power, January 1977, p. 21.

27. Turner, J. R., "An Investigation of the End-Wall Boundary Layer of a Turbine-Nozzle Cascade", Trans. ASME 79, p. 1801, 1957.

28. Woods, J. R., "An Investigation of Secondary-Flow Phenomena and Associated Losses in a High Deflection Turbine Cascade", Ph.D. Thesis, Naval Postgraduate School, Monterey, California, September 1972.

29. Sjolander, S.A., "The Endwall Boundary Layer in an Annular Cascade of Turbine Nozzle Guide Vanes", Technical Report ME 1A75-4, Carleton University, Ottawa, December 1975.

30. Hawthorne, W. R., "Thermodynamics of Cooled Turbines", Part 1 - "The Turbine State", Trans. ASME, 78, 1956, p. 1781.

APPENDIX 1

ERROR ANALYSIS

Typical error estimates, in the most frequently reported calculated flow parameters, were obtained from the following equation:

$$W_R = \left\{ \left\{ \frac{\partial R \; W_1}{\partial x_1} \right\}^2 + \left\{ \frac{\partial R \; W_2}{\partial x_2} \right\}^2 + \cdots + \left\{ \frac{\partial R \; W_n}{\partial x_n} \right\}^2 \right\}^{\frac{1}{2}} \qquad (A1.1)$$

where

R is the computed parameter or result.

W_R is the uncertainty in the computed result.

x_n is the n^{th} variable.

W_n is the uncertainty in the n^{th} variable.

The reported velocity profiles were determined from a particular form of the Bernouilli Equation described as follows:

$$V = \sqrt{\frac{(574K)E_1 T}{100 P_{atm} + KE_2}} \qquad (A1.2)$$

where

V is the computed velocity (m/s).

K is a numerical value composed of two terms: one from the transducer calibration curve and the other being the specific weight of water.

E_1 is the transducer output voltage corresponding to the dynamic pressure.

T is the measured static temperature (K).

P_{atm} is the atmospheric pressure (mbar).

E_2 is the transducer output voltage corresponding to the static pressure.

Applying equation A1.1 to A1.2 produces an estimate of the error in the calculated velocity according to:

$$\frac{WV}{V} = \left\{ \frac{1}{4}\left\{\frac{W_{E_1}}{E_1}\right\}^2 + \frac{1}{4}\left\{\frac{W_T}{T}\right\}^2 + \frac{1}{4}\left\{\frac{100\ W_{P_{atm}}}{100\ P_{atm} + KE_2}\right\}^2 + \cdots \right.$$

$$\left. \cdots + \frac{1}{4}\left\{\frac{KW_{E_2}}{100\ P_{atm} + KE_2}\right\}^2 + \frac{1}{4}\left\{\frac{100\ P_{atm}\ W_K}{(100\ P_{atm} + KE_2)K}\right\}^2 \right\}^{\frac{1}{2}} \quad \text{(A1.3)}$$

The typical percentage error for the velocity (from A1.3) was less than $\pm$ 1%.

In terms of transducer output voltages, the total pressure loss coefficient Cp_0 and the static pressure coefficient Cp_s were expressed as follows:

$$Cp_0 = \frac{E_{01} - E_0}{E_{dyn}} \quad \text{(A1.4)}$$

$$Cp_s = \frac{E_1 - E}{E_{dyn}} \quad \text{(A1.5)}$$

where

E_{01} is the transducer output voltage corresponding to the mean total pressure across the test passage at mid-span at the inlet measuring station.

E_0 is the output voltage corresponding to the total pressure at a point in the plane of

exit measuring station A.

E_{dyn} is the output voltage corresponding to the mean dynamic pressure across the test passage at mid-span at the inlet measuring station.

E_1 is the output voltage corresponding to the static pressure in the plane of the inlet measuring station A.

Applying equation A1.1 to A1.4 produces an estimate of the error in Cp_0 according to:

$$WCp_0 = \left\{ \left\{ \frac{W_{E_{01}}}{E_{dyn}} \right\}^2 + \left\{ \frac{W_{E_0}}{E_{dyn}} \right\}^2 + \frac{(-E_{01} + E_0)^2 (W_{E_{dyn}})^2}{(E_{dyn})^4} \right\}^{\frac{1}{2}} \quad \text{(A1.6)}$$

and similarly, apply A1.1 to A1.5 yields:

$$WCp_s = \left\{ \left\{ \frac{W_{E_1}}{E_{dyn}} \right\}^2 + \left\{ \frac{W_E}{E_{dyn}} \right\}^2 + \frac{(-E_1 + E)^2 (W_{E_{dyn}})^2}{(E_{dyn})^4} \right\}^{\frac{1}{2}} \quad \text{(A1.7)}$$

Typical error estimates for Cp_0 and Cp_s (from equations A1.6 and A1.7) were found to be $\pm$ 9% and $\pm$ 4% respectively.

APPENDIX 2

SUPPLEMENT FOR INSTRUMENTATION

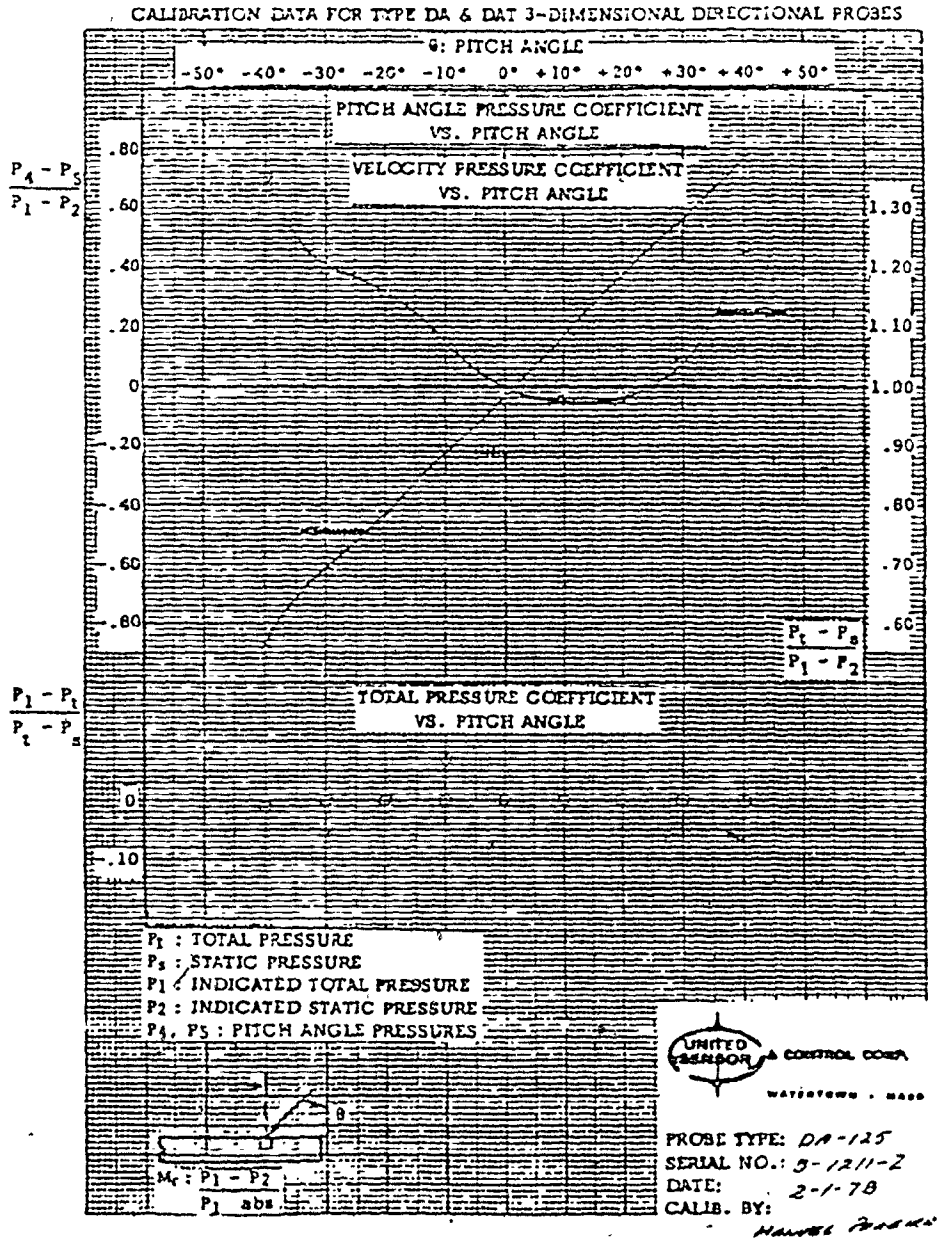

Figure A2.1 Manufacturer's Calibration Data for the Three-Dimensional Probe.

Specifications for the

Setra Model 237 Low Range Pressure Transducer

Operating Principle	Variable capacitance type sensor
Range	$\pm$ 0.5 psid ($\pm$ 3.447 378 kPa) bi-directional differential
Maximum Overload	100 psi, positive direction, 2.5 psi in negative direction
Excitation	24 volts D.C.,25 ma, nominal
Full Range Output	0 to $\pm$ 2.5 volts nominal
Zero Output	$\leq \pm$ 100 mv at 77°F
Non-Linearity	$\leq \pm$ 0.25% of full range output, (best straight line method)
Hysteresis	$\leq \pm$ 0.1% of full range output, (infinite resolution)
Ambient Operating Temperature Limits	0°F to 175°F
Compensated Temperature Range	30°F to 150°F
Thermal Zero Shift	$\leq \pm$ 0.015% full range/°F, 30°F to 150°F
Thermal Coefficient of Sensitivity	$\leq \pm$ 0.01% full range/°F, 30°F to 150°F
Acceleration Response	< 0.0002 psi/g typical

Volume Increase Due to F.R. Pressure	1×10^{-5} cubic inches
Natural Frequency	5000 H_z nominal
Output Noise	< 5 mv r.m.s.

APPENDIX 3

SPECIFICATIONS FOR THE BELLMOUTH INLET DUCT

The inlet bellmouth duct was designed from a series of profiles defined by Smith et al. {23} . The profiles for the inlet duct surfaces were derived from the non-dimensionalized co-ordinates for Z and R (found in Table 1 of Reference {23}). The throat dimensions, shown in Figure 3.2, were determined from the geometry of the inlet channel. The overall length of the duct was limited to 60.2 cm due to floor space limitations. The co-ordinate system chosen to specify the profiles is defined as follows:

z is parallel to the flow direction.
x is parallel to the throat height (blade span).
y is parallel to the throat width.

The origin was located at the throat mid-height and mid-width position. The profile co-ordinates for the z - x plane and the z - y plane are shown in Table A3.1. These co-ordinates for the z - x and z - y planes were derived from columns e and f (Table 1 of Ref. {23}) respectively.

Table A3.1

Profile Co-ordinates for the
Bellmouth Inlet Duct

z - x plane		x - y plane	
z(cm)	x(cm)	z(cm)	y(cm)
0	9.42	0	9.95
2.61	9.42	2.61	9.95
5.23	9.42	5.23	9.95
7.85	9.47	7.85	10.00
10.47	9.52	10.47	10.10
13.08	9.66	13.09	10.18
15.70	9.97	15.71	10.50
18.32	10.36	18.34	10.95
20.94	10.62	20.59	11.23
23.56	11.64	23.57	12.28
26.17	12.50	26.19	13.22
28.79	13.50	28.81	14.29
31.41	14.58	31.43	15.56
34.03	15.86	33.97	16.97
36.64	17.39	36.68	18.54
39.26	18.95	39.30	20.30
41.88	20.67	41.91	22.16
44.50	22.50	44.53	24.12
47.12	24.47	47.15	26.32
49.73	26.54	49.78	28.63
52.35	28.79	52.40	31.17
54.97	31.14	55.02	33.85
57.59	33.66	57.64	36.70
60.20	36.28	60.20	39.49